TECHNISCHE UNIVERSITÄT MÜNCHEN
Max-Planck-Institut für Physik
Werner-Heisenberg-Institut

Improving the Light Channel of the CRESST-II-Dark Matter Detectors

Michael Kiefer

Vollständiger Abdruck der von der Fakultät für Physik der Technischen Universität München zur Erlangung des akademischen Grades eines

Doktors der Naturwissenschaften

genehmigten Dissertation.

Vorsitzender:		Univ.-Prof. Dr. Alejandro Ibarra
Prüfer der Dissertation:	1.	Hon.-Prof. Allen C. Caldwell, Ph.D.
	2.	Univ.-Prof. Dr. Lothar Oberauer

Die Dissertation wurde am 22.02.2012 bei der Technischen Universität München eingereicht und durch die Fakultät für Physik am 07.03.2012 angenommen.

Überblick

Seit Beginn des zwanzigsten Jahrhunderts gibt es Indizien, die auf die Existenz von Dunkler Materie hindeuten. Kapitel 1 stellt einige dieser Hinweise sowie Annahmen über die Beschaffenheit der Dunklen Materie vor. Ein Überblick über mögliche Nachweismethoden bildet den Abschluss dieses Kapitels.

Das CRESST-Experiment zielt darauf ab, Teilchen der Dunklen Materie durch Streuung an den Atomkernen eines szintillierenden Kristalls bei tiefen Temperaturen nachzuweisen. Gemessen werden sowohl die dadurch angeregten Phononen als auch das Szintillationslicht. Der Aufbau des Experiments sowie Techniken zur Datenaufbereitung und -analyse werden in Kapitel 2 beschrieben. Dies betrifft insbesondere zwei für den weiteren Inhalt dieser Arbeit wichtigen Aspekte, die Untergrundunterdrückung mit Hilfe des Szintillationslichts und die Energiekalibration der Detektoren.

Um auch bei geringen Energieeinträgen eine Untergrundunterdrückung zu gewährleisten, ist eine hohe Lichtausbeute notwendig. Die in Kapitel 3 vorgestellten Komposit-Detektoren werden mit einem Verfahren produziert, das im Vergleich zum herkömmlichen schonender für die Szintillatorkristalle ist. Dabei wird der Sensor separat produzidert und auf den Szintillatorkristall aufgeklebt. Nach der Vorstellung dieses Produktionsverfahrens erfolgt ein Vergleich der Energieauflösung der Komposit- und der herkömmlichen Detektoren. Die Komposit-Detektoren stellen einen Verbund zweier unterschiedlicher Materialien dar. Durch Simulationen mit der Methode der finiten Elemente ist es möglich, einen Eindruck von den beim Abkühlen auftretenden mechanischen Spannungsverhältnissen zu bekommen.

Kapitel 4 beschreibt verschiedene Wege zur Bestimmung der Leistungsfähigkeit des Lichtkanals einzelner Detektoren. Die bisher praktizierte Methode wird dabei zwei neu entwickelten gegenüber gestellt. Anhand dieser Verfahren können die Lichtausbeuten der Komposit-Detektoren mit denen der herkömmlichen verglichen werden. Die Untersuchung der Daten eines weiteren, modifizierten Moduls gibt Aufschluss über die Ausbreitung des Lichts im Inneren eines Detektors.

Die Qualität der Detektorkristalle in Hinblick auf den Lichtkanal ist auch innerhalb eines einzelnen Kristalls nicht zwangsläufig unabhängig vom Ort des Energieeintrags. Durch die Analyse des Lichtsignals das durch den Zerfall eines Spurenisotops und dessen Tochterprodukts im Kristall verursacht wird, kann man einen Einblick über das Ausmaß dieser Qualitätsunterschiede gewinnen. Die Ergebnisse dieser Untersuchung in Kapitel 5 bilden den Abschluss dieser Arbeit.

Abstract

Since the beginning of the twentieth century, there is evidence for the existence of Dark Matter. Chapter 1 presents some of these observations as well as the current assumptions about the nature of Dark Matter. The chapter concludes by showing some possible methods of detecting Dark Matter.

The CRESST experiment aims at the detection of Dark Matter particles via scattering processes on the atomic nuclei of a scintillating crystal detector at low temperatures. The particle interactions in the crystal are measured via their excitation of phonons and scintillation light. The setup of the experiment, as well as techniques of data preparation and analysis are the subjects of Chapter 2. This includes the introduction of two concepts which are important for the further contents of this work, namely the background discrimination with the help of scintillation light and the energy calibration of the detectors.

In order to provide a background discrimination, even for low energies, a highly efficient light production is necessary. The composite detectors presented in Chapter 3 are produced in a way that is more protective to the scintillating crystals than the conventional method: For a composite detector, the sensor is produced apart from the scintillator crystal and then glued to it. After describing the production method, the chapter continues with a comparison of the energy resolution of composite and conventional detectors. A composite detector is a compound of two different materials with different mechanical properties. Using the finite element method, it is possible to gain an impression of how the thermo-mechanical stresses affect the materials during the detector cool-down.

Chapter 4 describes several ways of determining the performance of the light channel of individual detectors. Together with the method which is currently used, the chapter presents two newly developed methods. With these methods, it is possible to compare the light channel parameters of the composite and the conventional detectors. The data of another modified module make it possible to obtain information on the propagation of light within a detector module.

The quality of the detector crystals with respect to the light channel is not necessarily constant, even within a single crystal. By analyzing the light signal caused by the decay of a certain trace isotope and its daughter product, one can get an impression on the magnitude of these variations. The results of this investigation in Chapter 5 conclude this thesis.

Contents

1. Dark Matter

Since the 1930s, more and more evidence has been found that our Universe does not solely consist of stars, planets and nebulæ.

Some of the observations will be shown in the first part of this chapter. The second part will present the role of Dark Matter in the standard model of cosmology, and additional evidence for its existence. As such evidence was found in more and more fields of physics using different methods, the number of theories about the nature of Dark Matter grew as well. The third part will introduce a few of them, focusing especially on the Weakly Interacting Massive Particle (WIMP), the particle the CRESST[1]-collaboration is searching for. The chapter will continue showing different methods of detection of Dark Matter and conclude with considerations on the feasibility of an experiment which takes the approach of measuring the direct interaction of Dark Matter with a detector.

1.1. Evidence for the Existence of Dark Matter

Historically, the first evidence for Dark Matter was found in 1933 by Fritz Zwicky. Performing Doppler measurements on spectral lines of galaxies in the Coma Cluster, he concluded on the velocities of the individual galaxies. Using the virial theorem, he could then calculate the mass of the cluster components. Comparing this to the mass obtained by estimating the number and mass of the stars in the cluster, he found the two masses to differ by a factor of 400. As a solution, he postulated an invisible form of matter which contributes the missing mass of the cluster [Zwi33].

1.1.1. Rotational Curves of Galaxies

Newtonian mechanics can describe the motion of stars in a spiral galaxy in a fairly good approximation. In this description, the velocity v of a star

[1] Cryogenic Rare Event Search with Superconducting Thermometers

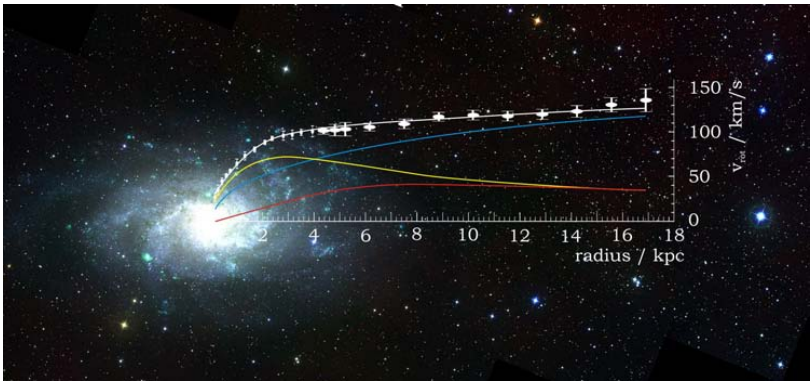

Figure 1.1.: The observed rotational curve of the galaxy M33 (points) and its theoretical counterpart, calculated according to the luminous matter distribution in the bulge alone (yellow), and with gas (red). Adding a Dark Matter halo contribution (blue) results in a curve (white) fitting well to the observation[Lan08].

orbiting the center of a spiral galaxy at a distance r is

$$v(r) = \sqrt{\frac{GM(r)}{r}}. \tag{1.1}$$

$M(r)$ is the total mass inside the orbit of the star. Masses outside the orbit do not contribute to the overall gravitational force. Assuming a mass distribution following the distribution of luminous matter in the galaxy, one can compare the velocities calculated by this model to those observed by Doppler measurements, e.g. in the galaxy cluster M33 (see Figure 1.1). This clearly suggests that either Newtonian mechanics or the assumption leading to the matter distribution is not valid.

Staying confident to Newton, one must assume that a spiral galaxy consists of more matter than only the visible parts. This matter is distributed in the form of a spherical halo, by far larger than the galaxy itself [CS99].

1.1.2. Mass Distribution in Galaxy Clusters

The mass distribution of galaxy clusters can also be determined by their gravitational lensing effect: According to Albert Einstein's theory of general relativity, the presence of mass distorts space and thus also distorts the path along which a beam of light propagates. This was first observed in

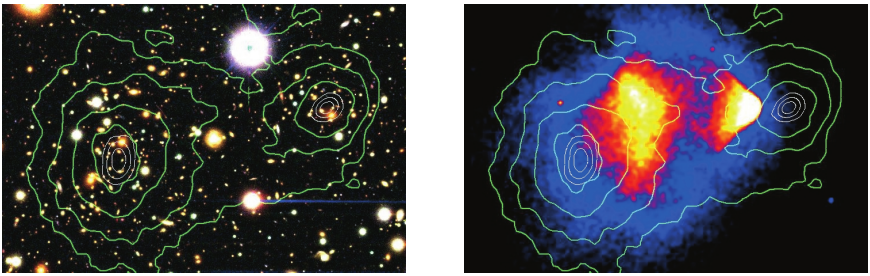

(a) Visible (b) X-Ray

Figure 1.2.: These images of the Bullet cluster were taken in the visible (left) and in the X-ray spectrum (right). The visible image shows the stars, the X-ray image shows the gas of the clusters. The green lines superimposed to the pictures indicate the mass distribution according to an analysis of the gravitational lensing effect [Clo+06].

1919, during a solar eclipse, contributing significantly to Einstein's popularity even among laypersons [Seg97].

A massive object, as for example a galaxy cluster in the line of sight between Earth and distant objects, can deflect the light coming from the objects in the background. In the case of strong gravitational lensing, the effect concerns single objects and can lead to ring-shaped distortions. For Dark Matter search, the weak gravitational lensing effect is more important. Here, the lensing effect concerns a background of galaxies. With no gravitational lensing, the shapes and orientations of these galaxies follow a certain statistical distribution. If there is a lensing object in the line of sight, the statistical distribution deviates from the observation without lensing.

A strong evidence for Dark Matter was discovered in 2006, in the so-called Bullet cluster: a collision of two galaxy clusters separated the components of the clusters, namely stars and gas clouds. This can be seen when comparing images taken in the visible spectrum to those taken by the Chandra X-Ray satellite (see Figure 1.2). This separation happens because the stars of the cluster hardly interact with each other in contrast to the gas clouds which experience a friction.

Thus, the stars leave the center of the system faster than the gas clouds do. In typical galaxy clusters, the gas contributes to the total mass much more than the stars. Therefore, the gravitational lensing effect should be much higher in the region where the gas resides than in the outer parts

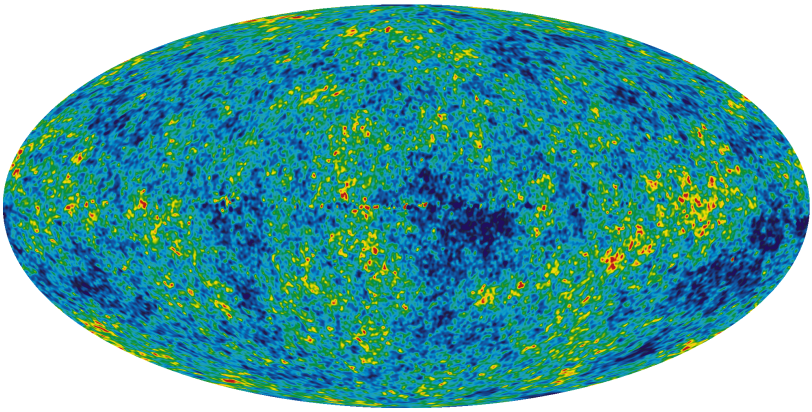

Figure 1.3.: Temperature fluctuations in the Cosmic Microwave Background radiation, recorded by WMAP, the Wilkinson Microwave Anisotropy Probe [NAS07]. The fluctuations are shown in color code ranging from 200 µK below (violet) to 200 µK above (red) average.

containing the stars. When calculating the mass distribution according to the gravitational lensing, the opposite was found to be true [Clo+06]. The major part of the matter endured the collision without any effects of friction. This observation is a strong evidence that a significant part of the galaxy clusters consists of Dark Matter which is not affected by frictional processes during the collision.

1.1.3. Cosmic Microwave Background

Besides evidence on galactic and cluster scales, there are also measurements on cosmic scale that indicate the existence of Dark Matter: The Cosmic Microwave Background (CMB) is electromagnetic radiation that has been emitted when the cosmic plasma became transparent to electromagnetic radiation 400,000 years after the Big Bang. Before that, the electromagnetic radiation was coupled to the cosmic plasma. This fact makes the background radiation a snapshot of the cosmic plasma at the time of decoupling. Due to red shift, the cosmic background radiation has shifted to the microwave band.

The WMAP collaboration has performed a precise measurement of the cosmic microwave background radiation (see Figure 1.3). From this measurement, they concluded on the angular variations of the temperature and

therefore the density of the early Universe. This allowed to extract information on the amount of Dark Matter in the overall composition of the Universe (see Section 1.2.2).

1.2. The Role of Dark Matter in the Universe

1.2.1. The Standard Model of Cosmology

The discovery of Dark matter would not only solve the missing mass problem in galaxy and cluster dynamics. Providing it exists, Dark Matter plays a significant role in cosmic evolution too.

The Friedman equation connects the expansion of the Universe to its curvature and density:

$$\underbrace{H^2(t)}_{\text{Expansion}} + \underbrace{\frac{c^2\kappa}{a^2(t)}}_{\text{Curvature}} = \underbrace{\frac{8\pi}{3}G\rho}_{\text{Matter}} + \underbrace{\frac{c^2\Lambda}{3}}_{\text{Vacuum energy}}. \tag{1.2}$$

The scale factor $a(t)$ describes the increase of the distance L between two points. As space expands, these points drift apart. If two points have a distance L_0 at present time $t = t_0$, their distance increases as

$$L(t) = a(t) L_0. \tag{1.3}$$

One cannot measure the scale factor itself, but only its normalized temporal development, represented by the Hubble parameter:

$$H(t) = \frac{\dot{a}(t)}{a(t)} \tag{1.4}$$

Similar to the distance L_0, one can define the Hubble constant H_0 as today's value of the Hubble parameter:

$$H_0 = H(t = t_0) \tag{1.5}$$

The cosmological constant Λ describes a vacuum energy (Dark Energy) which increases the speed at which the Universe expands.

The curvature κ is a property of space itself. It can have values of -1, 0 or 1. In a flat space with $\kappa = 0$, two parallel lines will stay parallel at infinity. If space is positively curved (open), such parallel lines will intersect like the meridians on a globe, which are parallel in the equatorial region

but intersect at the poles. A space with negative curvature would feature parallel lines which drift apart.

Assuming a cosmological constant of $\Lambda = 0$ and a flat space ($\kappa = 0$), one can define a critical density ρ_c fulfilling the Friedman equation at present time:

$$\rho_c = \frac{3{H_0}^2}{8\pi G} \tag{1.6}$$

Dividing by ${H_0}^2$, one can rewrite the Friedman equation (1.2) as

$$1 = \underbrace{\frac{\rho_M}{\rho_c}}_{\text{Matter}} - \underbrace{\frac{c^2\kappa}{a^2(t)\,{H_0}^2}}_{\text{Curvature}} + \underbrace{\frac{c^2\Lambda}{3{H_0}^2}}_{\text{Vacuum energy}} \tag{1.7}$$

One defines the ratio between matter density ρ_M and critical density ρ_c as matter density parameter

$$\Omega_M = \frac{\rho_M}{\rho_c} \tag{1.8}$$

Then the remaining terms can be defined as density parameters as well, adding up to the density Ω of the entire Universe:

$$\Omega = \Omega_M - \Omega_\kappa + \Omega_\Lambda. \tag{1.9}$$

This equation shows the connection between the different components of the Universe and its future development in form of the Hubble parameter.

1.2.2. Composition of the Universe

By analyzing [Kom+11] the Cosmic Microwave Background from the data of WMAP, it was possible to deduce values for the Hubble parameter $H_0 = 70.4^{+1.3}_{-1.4}\,\mathrm{km\,s^{-1}\,Mpc^{-1}}$ as well as for the different components of the density parameter listed above. The component Ω_M related to the Matter is even specified further in terms of Non-Baryonic Dark Matter Ω_c and Baryons Ω_b as follows:

- $-0.0133 < \Omega_\kappa < 0.0084$: The Universe is flat.
- $\Omega_\Lambda = 0.728^{+0.015}_{-0.016}$: The major component in the Universe is Dark Energy.
- $\Omega_c = 0.227 \pm 0.014$: Most of the matter in the Universe is non-baryonic Dark Matter.

- $\Omega_b = 0.0456 \pm 0.0016$: Less than 5 % of the Universe consists of baryonic matter.

For galaxies, the contribution of luminous matter to the total density is in the range of $\Omega_{\text{lum}} \approx 0.01$ [BG06]. This means that among the baryonic component, the luminous part is only about one fourth. Among the candidates for the dark baryonic part are Massive Compact Halo Objects (MACHOs) and galactic filaments. MACHOs could be brown dwarfs, neutron stars and black holes [Nar93]. As described in [FPL11], the galactic filaments contain most of the baryons in the Universe.

1.3. Candidates for Non-Baryonic Dark Matter

The considerations concerning a Dark Matter candidate have to include certain prerequisites in order to comply with the current observations:

- By definition, Dark Matter cannot not interact with light, so it has to be *electrically neutral*.
- Since all evidence relies on gravitational interaction, Dark Matter must *have a mass*.
- No unexplained interaction involving the strong nuclear force has been observed, so the particles have to be *color neutral* as well.
- Dark Matter must be *stable on cosmological time scale*, since its current impact on celestial mechanics can be observed as well as its influence on the early Universe.
- Simulations of structure formation in the early Universe indicate that at that time, the Dark matter particles had to be non-relativistic (so called *Cold Dark Matter*). The opposite, *Hot Dark Matter* could not have created small structures like galactic halos first, before accumulating to larger structures like galaxy clusters and super clusters.
- The properties of the candidate have to be compliant with current models and observations of the Big Bang Nucleosynthesis and stellar evolution.
- In order for the theory to be falsifiable in a direct detection experiment (see Section 1.4), there has to be a rare but measurable interaction of Dark Matter with normal matter. This is possible if Dark Matter participates in the weak nuclear interaction.

1.3.1. Standard Model Particles

The only particle described by the Standard Model of particle physics, which partially features the properties needed for Dark matter is the *neutrino*. However, as neutrinos are relativistic, they cannot be responsible for structure formation according to the current state of knowledge. Furthermore, upper limits for neutrino abundance and mass today indicate that neutrinos can only contribute with %1.3 to the overall density of the Universe, so they cannot be the only candidate [NG10]. Since no Standard Model particles can fully explain Dark Matter, current searches focus on particles beyond the Standard Model.

1.3.2. WIMPs

The candidate on which the CRESST-II Dark Matter search and other experiments focus, the Weakly Interacting Massive Particle (WIMP), is a hypothetical generic type of particle. This candidate is supposed to fulfill the prerequisites described above.

In the theory of Supersymmetry (SUSY), several such particles exist. The basis of this theory is the concept that each standard model particle has a supersymmetric partner. The difference between normal and supersymmetric particles is the spin; the superpartners of bosons are fermions and vice versa. The conservation of a quantum number called *R*-parity prevents the decay of the lightest SUSY particle into Standard Model particles as well. This makes the Lightest Supersymmetric Particle (LSP) a stable particle and thus a candidate for Dark Matter. In the Minimal Supersymmetric Standard Model (MSSM), there are two electrically neutral LSP candidates [BG06]:

The Gravitino: The superpartner of the graviton. As it interacts only gravitationally, chances of its discovery are extremely feeble. This renders a theory of Dark Matter involving gravitinos as hardly falsifiable and thus of low scientific value.

The Neutralino: A superposition of the superpartners of W, Z, γ, and Higgs boson.

1.3.3. Axions

SUSY is one theory among others, which extend the Standard Model and include candidates which could serve as Dark Matter candidates.

One of these candidates is the Axion, which was originally postulated in order to explain why CP violations only exist in weak but not in strong interactions. It turns out that axions would be a Cold Dark Matter candidate as well [NG10]. If the mass of the axion was in a range between 10^{-6} and 10^{-3} eV, it could contribute significantly to Dark Matter. Several experiments try to detect axions, as they are supposed to be convertible to photons inside a strong magnetic field [BG06].

Since the CRESST experiment aims for the detection of Dark Matter in the form of WIMPs, the following considerations are focused only on WIMP Dark Matter.

1.4. Overview on the Different Methods for the Detection of WIMPs

There are several methods which one could use to gather information on WIMPs:

Collider experiments try to produce color-charged SUSY particles in high energy collisions, for example at the Large Hadron Collider (LHC). If R-Parity is conserved, these particles can only decay to the color-neutral LSP if they dispose their color charge. This results in events with high-jet multiplicity. The escaping LSP could be noticed as a missing transverse energy [Ber+10].

The indirect method aims at the possibility that already existing particles of Dark Matter could either decay or annihilate each other. The resulting secondary particles, preferably γ-rays could be detected using for example air Čerenkov telescopes [Ber+10].

Direct detection experiments on the other hand are based on the assumption that the WIMP density in the galactic Dark Matter halo is sufficiently high, allowing to detect WIMP-nucleon scattering events in low-background experiments. The scatterings are supposed to cause measurable nuclear recoils in the detector.

The WIMP energy spectrum is not supposed to show any characteristic features as e.g. lines. The energy and the rate of the signal are expected to be low. For example in [Sch10], the energy transfer of a WIMP-nucleaon scattering is estimated to be of $\mathcal{O}(10\,\mathrm{keV})$ and the rate of $0.1\,\mathrm{kg}^{-1}\,\mathrm{d}^{-1}$ respective to the detector mass and the measurement time.

In order to still have a possibility to identify a WIMP spectrum, one needs to distinguish the WIMP part of a signal from possible backgrounds. Two methods for rejecting background are

Signal discrimination: WIMPs are expected to scatter off atomic nuclei. The background has a significantly high component of electrically charged particles. These interact mainly with the electrons in the detector material. A method of discrimination between electron and nuclear recoil signals could reduce the background.

Signal multiplicity: As they are not electrically charged, neutrons do not scatter off the electrons, but also off the nuclei. This means that giving a similar signal, a neutron background could not be separated from the WIMP signal that easily, especially in the range of low energies. On the other hand, the probability of a WIMP scattering twice or even more often in the same detector is extremely low, whereas neutrons can scatter multiple times.

Once the background is removed, one could try to circumstantiate the hypothesis of having found a WIMP signal by further criteria as e.g.:

Multi-target approach: The scattering cross section depends on the mass of the nucleus involved. Since the form of this dependence is known, the comparison of signal rates obtained with two or more different nuclei provides a way of identifying a WIMP signal.

Temporal modulation: Since the WIMP velocity relative to the detector influences the signal rate, there is a possibility to identify WIMPs by this variation. In an Earth-bound detector, the velocity of the detector relative to the WIMP halo changes periodically twice: Each day, as Earth rotates around itself and each year as Earth revolves around the sun, while the solar system is moving through the WIMP halo. These velocities periodically add up constructively or destructively. Determining the amplitude, phase and periodicity of the signal and comparing this to the model gives a possibility to identify a WIMP signal. However, for this method to work one needs relatively high signal rates in order to produce a statistically reliable result.

Directional information: If a detector could determine the direction of incoming particles, the same periodicity should be visible in a signature of the direction as well.

1.5. Direct detection of WIMPs

1.5.1. Event rate

In order to produce valuable results, an experiment needs to be constructed such, that the rate of WIMP events is statistically significant. The WIMP detection rate R' rate depends on the flux Φ_χ through the target, the number of target nuclei $n_\mathcal{N}$ and the cross section σ for WIMPs scattering off nuclei:

$$R' = \Phi_\chi \sigma n_\mathcal{N}. \tag{1.10}$$

In order to compare different experiments, one can normalize the rate by the detector mass m_D which is a product of the number $n_\mathcal{N}$ and mass $m_\mathcal{N}$ of the target nuclei

$$R = \frac{R'}{m_D} = \frac{\Phi_\chi \sigma}{m_\mathcal{N}}. \tag{1.11}$$

1.5.2. Differential recoil spectrum

This rate is only a rough value. In reality, not all WIMPs have the same velocity, but the velocity follows a certain distribution $f(v)$. Furthermore, the cross section might be depending of the velocity and the transferred energy.

In order to obtain a more realistic picture, it is necessary to estimate the recoil spectrum. For this, one must calculate the differential event rate $\frac{\mathrm{d}R}{\mathrm{d}E_R}$:

$$\frac{\mathrm{d}R}{\mathrm{d}E_R} = \frac{\mathrm{d}}{\mathrm{d}E_R}\frac{\Phi_\chi \sigma}{m_\mathcal{N}} \tag{1.12}$$

$$= \frac{1}{m_\mathcal{N}} \Phi_\chi \frac{\mathrm{d}\sigma}{\mathrm{d}E_R} \tag{1.13}$$

$$= \frac{n_\chi}{m_\mathcal{N}} \int_{v_{\min}}^{\infty} \mathrm{d}^3 v f(v)\, v \frac{\mathrm{d}\sigma(\vec{v_\chi}, E_R)}{\mathrm{d}E_R} \tag{1.14}$$

This includes the flux of WIMPs Φ_χ depending on their velocity v and number density n_χ as:

$$\Phi_\chi = n_\chi v. \tag{1.15}$$

The velocity $v_{\min}$ is the minimal value above which the energy E_R can be transferred in an elastic scattering process:

$$v_{\min} = \sqrt{\frac{E_R m_\mathcal{N}}{2\mu_{\chi\mathcal{N}}{}^2}}, \tag{1.16}$$

where the value $\mu_{\chi\mathcal{N}}$ denotes the reduced mass of WIMP and nucleus

$$\mu_{\chi\mathcal{N}} = \frac{m_\chi m_\mathcal{N}}{m_\chi + m_\mathcal{N}}. \tag{1.17}$$

Scattering cross section

The cross section σ in general has two contributions, one spin-independent with the index SI and the other spin-dependent with the index SD:

$$\sigma = \sigma_{\mathrm{SI}} + \sigma_{\mathrm{SD}}. \tag{1.18}$$

The target nuclei used in CRESST have a net spin of zero, except for some rare isotopes [Son10]. Thus, the spin-dependent part is negligible. The differential spin-independent cross section is specified, for example in [Ber+10]:

$$\frac{\mathrm{d}\sigma_{\mathrm{SI}}}{\mathrm{d}E_R} = \frac{m_\mathcal{N}\sigma F^2\left(E_R\right)}{2\mu_{\chi\mathcal{N}}{}^2 v^2}. \tag{1.19}$$

The nuclear form factor $F\left(E_R\right)$ contains information about the nucleon density in the target nuclei. With this cross section, equation (1.14) states

$$\frac{\mathrm{d}R}{\mathrm{d}E_R} = \frac{n_\chi}{2\mu_{\chi\mathcal{N}}{}^2}\sigma F^2\left(E_R\right)\int_{v_{\min}}^{\infty}\mathrm{d}^3v\frac{f(v)}{v}. \tag{1.20}$$

There are experiments with various target materials and therefore various target *nuclei* with different σ. In order to compare them, a normalized cross section for coherent elastic WIMP-*nucleon* scattering $\sigma_{\chi N}$ is used [Bot+97]:

$$\sigma_{\chi N} = \left(\frac{1+\frac{m_\chi}{m_\mathcal{N}}}{1+\frac{m_\chi}{m_p}}\right)^2\frac{\sigma}{A^2}, \tag{1.21}$$

with the atomic mass number of the target as A and the proton mass m_p.

The current limit for the cross section $\sigma_{\chi N}$ is in the range of $10^{-3}\,\mathrm{pb}$ for WIMPs with $m_\chi = 10\,\frac{\mathrm{GeV}}{c^2}$ [Apr+11]. If the target nuclei have a similar mass than the WIMPs, this means a WIMP-nucleus cross section of

$$\sigma \approx \mathcal{O}\left(10^{-9}\,\mathrm{pb}\right) \tag{1.22}$$

Velocity distribution

The next step is the velocity distribution, which is of Maxwell-Boltzmann type in the simplest realistic case. Such a model, called an isothermal sphere, describes particles which are gravitationally bound and in thermal equilibrium. With a cutoff at the escape velocity, according to [DFS98], the velocity distribution is

$$f(\vec{v}) = \mathfrak{N}\left(\frac{3}{2\pi w^2}\right)^{\frac{3}{2}} \exp\left(-\frac{3v^2}{2w^2}\right) |. \tag{1.23}$$

Here, w specifies the root means square of the WIMP velocities in the galactic rest frame:

$$w = \sqrt{\frac{3}{2}} v_\infty \tag{1.24}$$

with the asymptotic value v_∞ for the rotational velocity. In our galaxy, over large ranges, the rotational velocity is similar to that of our solar system $v_\odot = 220\,\mathrm{km\,s^{-1}}$. Therefore,

$$w = 270\,\mathrm{km\,s^{-1}} \tag{1.25}$$

The normalization factor $\mathfrak{N}$ is explicitly written as

$$\mathfrak{N} = \left(\mathrm{erf}(z) - \frac{2}{\sqrt{\pi}} z \exp\left(-z^2\right)\right)^{-1} \tag{1.26}$$

with

$$z^2 = \frac{3}{2}\frac{v_{\mathrm{esc}}^2}{w^2}. \tag{1.27}$$

The term v_{esc} stands for the galactic escape velocity. Its current [Smi+07] values is

$$v_{\mathrm{esc}} = 544\,\mathrm{km\,s^{-1}}. \tag{1.28}$$

Form factor

The last term which is missing in equation (1.20) is the form factor F. It describes the spatial distribution of matter in an atomic nucleus. Particles with sufficiently high energies can "see" the scattering nucleus as an object with a substructure instead of point-like. Mathematically this is represented as a Fourier transform of the matter density of the nucleus.

The most common form factor model in Dark Matter search was developed by Richard Helm [Hel56], modeling the nuclear density $\rho(r)$ as a convolution of two density functions [Eng91]:

$$\rho\left(\vec{r}\right) = \int \mathrm{d}^3 r' \rho_0\left(\vec{r}'\right) \rho_1\left(\vec{r} - \vec{r}'\right) \tag{1.29}$$

The first term represents a sphere of constant density:

$$\rho_0\left(\vec{r}\right) = \begin{cases} \text{const.} & \left|r^2 < R_0^2\right., \\ 0 & \left|r^2 > R_0^2\right.. \end{cases} \tag{1.30}$$

The radius of the sphere is the text-book nuclear radius with a subtraction due to skin effects.

An exponential decay called the skin function describes the edge of the sphere:

$$\rho_1\left(\vec{r}\right) = \exp\left(-\frac{1}{2}\frac{r^2}{s^2}\right). \tag{1.31}$$

The dimension $s \simeq 1\,\mathrm{fm}$ denotes the skin thickness:

$$R_0{}^2 = R^2 - 5s^2. \tag{1.32}$$

The Fourier transform of the density $\rho\left(\vec{r}\right)$ yields

$$F\left(\vec{q}\right) = \int \rho\left(\vec{r}\right) \mathrm{e}^{\mathrm{i}\vec{q}\vec{r}} \mathrm{d}^3 r = 3\frac{j_1\left(qR_0\right)}{qR_0} \exp\left(-\frac{1}{2}(qs)^2\right). \tag{1.33}$$

with the momentum $q = \sqrt{2m_{\mathcal{N}} E_R}$ transferred in the scattering process. The function $j_1\left(qR_0\right)$ is the first spherical Bessel Function.

Spectrum

With all information provided, it is possible to compute and plot the expected differential event rate (see Figure 1.4). The plot shows spectra for three different WIMP masses from 10 GeV to 100 GeV. Each individual spectrum is the sum of the spectra of the chemical components of $CaWO_4$, the default target material in CRESST. The contribution of the different elements to the sum is weighted according to their stoichiometric quantities in the compound.

Overall, one can see that the differential spectrum is dominated by energies below 100 keV and that for cross-sections of $\mathcal{O}\left(10^{-6}\,\mathrm{pb}\right)$, the rates are very low as well. The differential cross section drops exponentially with the recoil energy. In addition to this drop, the spectra for 100 GeV and 1000 GeV show a dip in the range of 50 keV to 60 keV. This dip is an effect of the nuclear form factor of tungsten.

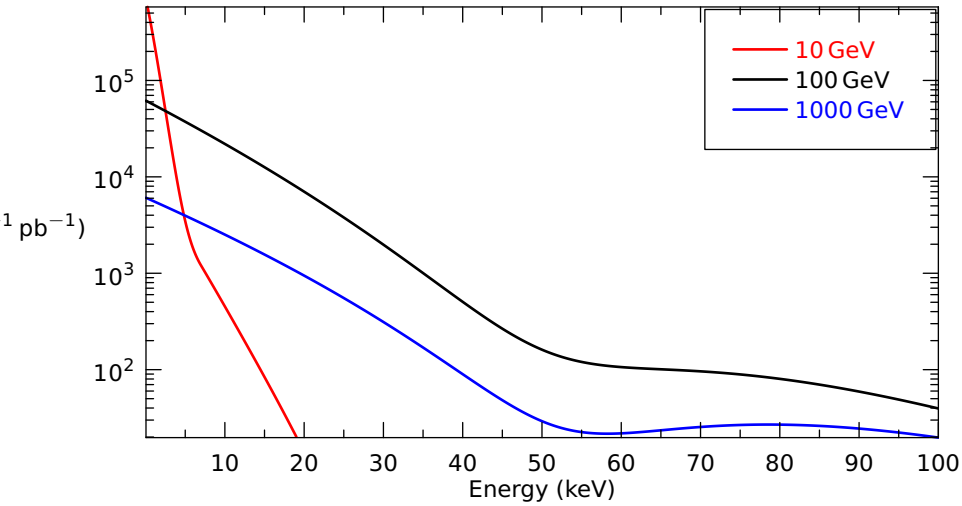

Figure 1.4.: The differential event rate of WIMPs with energies of 10 GeV, 100 GeV and 1000 GeV scattering off different nuclei, using the model of equation (1.20), with a Helm form factor. The dips around 50 keV are an effect of the nuclear form factor of tungsten.

The consequence of such a spectrum is that for finding a WIMP-signal, one needs a detector which is sensitive to low energy signals. The low signal rate is also an issue: There is a background of natural and artificial radioactivity whose rate exceeds the signal by many orders of magnitude. Thus, a detector has to be designed such, that it can filter the signal from the background.

1.6. Summary

Since the early 20th century, observations show that the Universe does not solely consist of visible matter. Today, observations ranging from dynamics on galactic scale to the anisotropy of the cosmic microwave background indicate that Dark Matter exists.

Extensions to the Standard Model of particle physics postulate particles which are suitable candidates for explaining the evidence for Dark Matter. These so-called WIMPs are particles which interact with baryonic matter only at extremely low cross sections.

A Dark Matter experiment is thus confronted with low signal rates, low energies and a featureless energy spectrum. This requires detectors of high sensitivity and good methods of identifying a weak signal in a strong background.

2. The CRESST-II Experiment

The CRESST (Cryogenic Rare Event Search with Superconducting Thermometers) collaboration maintains a WIMP Dark Matter search experiment in the Laboratori Nazionali del Gran Sasso (LNGS). This underground laboratory is located within the mountain of the same name in central Italy.

The experiment name CRESST-II comes from the fact that the experiment itself is already in its second phase. This phase includes the active background discrimination technique explained below. For reasons of simplicity, the name CRESST stands for the CRESST-II experiment in the following text.

Data taking sessions in CRESST are called *runs*. The data used in this thesis are from Run 31 and Run 32 which took place from April 2008 until February 2009 and from April 2009 until March 2011, respectively.

The first section of this chapter will introduce the different sources of noise and background that the experiment has to deal with. The detector modules and the physics behind them are the topic of Section 2.2. A description of the data acquisition system follows in Section 2.3. The last section will introduce the issues which have been addressed in this work.

2.1. Noise and Background

In principle, there are two sources of bad signal: there is a background of unwanted particles triggering a signal in the detector. In addition, there are electrical disturbances and mechanical vibrations. Exposing the detectors to these sources of false signal results in a trigger rate much higher than the rate of expected signal events. In this way, it would be impossible to discover a Dark Matter signal. One major problem in a Dark Matter experiment is therefore the reduction of noise and background signal.

2.1.1. Infrastructure and Noise Reduction

As shown in Chapter 1, Dark Matter experiments need to be extremely sensitive to energy and signal rate. The CRESST experiment achieves this sensitivity by using cryogenic detectors and transition-edge sensors (see

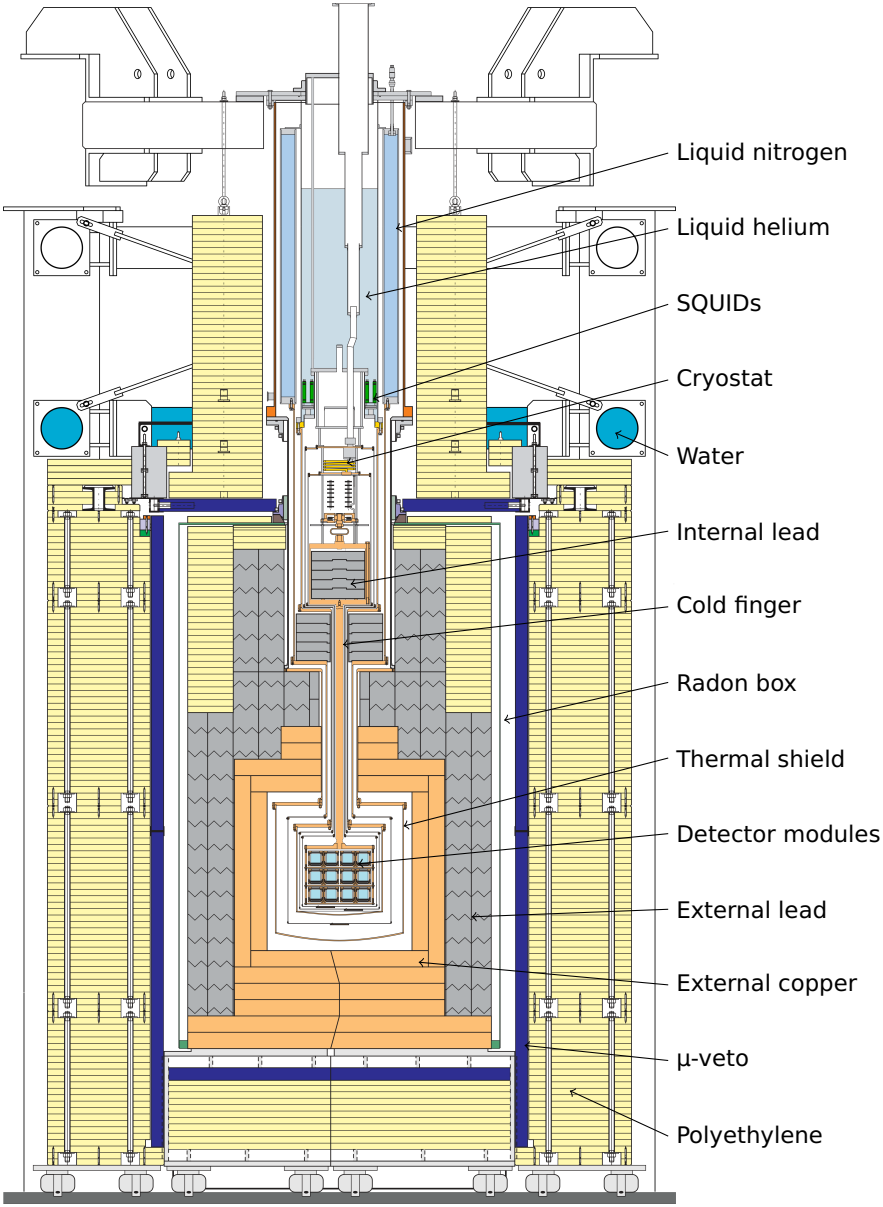

Figure 2.1.: Drawing of the CRESST experimental setup.

Section 2.2.4). A ^{3}He-^{4}He dilution refrigerator provides the necessary cooling power and is capable of cooling the modularly designed detector down to $\approx 6\,\mathrm{mK}$. The cryostat including its supply of cryogenic liquids dominates the upper part of Figure 2.1. The detector holder is in the center. It is capable of housing up to 33 detector modules. Various shields cover the detector from radioactivity and thermal radiation.

The pumps of the cryostat and the activities outside the experimental site cause vibrations. These vibrations are a source of mechanical noise for the experiment. In order to decouple the detector modules from this noise, they have no rigid contact to the outside world. Pneumatic dampers carry the weight of the cryostat and the detector modules. In order to avoid excessive coupling to the pumps, a heavy tube suspended by a double-gimbal structure and damped by two metallic bellows connects the cryostat to the pumping system.

The electrical signals of the detector modules pass strong amplifiers (so-called SQUIDs, see Section 2.3.1) before entering the readout electronics. This amplification does not only apply to the real detector signal but also to every electrical noise that the wires could pick up, e.g. from the power lines or from HF emitting devices. In order to keep the readout electronics from picking up noise from the outside world, the detectors and the SQUID system are located inside a Faraday cage.

2.1.2. Background Reduction

The detector modules are exposed to various sources of radioactivity. A passive shielding can reduce the radiation which comes from outside the experiment. An additional active discrimination technique removes the background originating from inside the shielding and from the detectors themselves.

Cosmic Rays

Earth is exposed to a radiation of high energy particles which are called cosmic rays. Absorptions of these particles in the upper atmosphere produce high energetic muons. This secondary radiation can penetrate the atmosphere down to ground level and even reaches into Earth's crust. When interacting with the material of the experiment, muons are capable of inducing neutron radiation, to which the detector is sensitive.

The bombardment with background particles makes a low-background experiment on the surface impossible. Instead, the CRESST experiment resides in the underground laboratory LNGS. The LNGS is a part of INFN, the

Italian national institute for nuclear physics. The facility itself, currently one of the largest underground laboratories operated world-wide, is located in a side cavern of a highway tunnel leading through the Abruzzese mountains. The rock surrounding the cavern extends at least 1400 m in every direction. This natural shielding reduces the muon flux to $\mathcal{O}\left(1\,\mathrm{h}^{-1}\,\mathrm{m}^{-2}\right)$, which is six orders of magnitude less than the level above ground [Arp92].

This natural shielding is necessary but not sufficient to make a low-background experiment possible. The remaining muons could trigger the detectors by themselves or generate secondary particles in the detector or the surrounding material. A dedicated muon detector around the actual experiment identifies them and thus provides a veto signal in order to reject time periods in which a muon has passed the detector.

The CRESST muon veto consists of 20 plastic scintillator panels, covering completely the sides of the detector, the bottom and, except for the cryostat pass-through, the top as well. The scintillation light of each panel is detected by an individual photomultiplier.

External Contamination

γ-Radiation The rock that surrounds the cavern is the main γ-background source in the laboratory. The rock contains various elements of the natural ^{238}U- and^{232}Th-decay chains and the radioactive ^{40}K isotope. In total, the γ-flux at the Gran Sasso laboratory is in the order of $10^7\,\mathrm{h}^{-1}\,\mathrm{m}^{-2}$ [Arp92].

An effective shielding against γ-rays is lead. Its heavy atoms provide high stopping power against γ-radiation. On the other hand, lead is not a clean material in terms of radio-purity. Especially its isotope ^{210}Pb can be a severe problem. This lead isotope is a part of the ^{238}U chain. With $T_{1/2} = 22.3\,\mathrm{yr}$ it is the most long-lived unstable lead isotope and it produces α-, β- and γ-radiation along its further decay.

Smelting the lead from its ore removes the parent nuclei of ^{210}Pb. Thus after smelting, the intrinsic radioactivity reduces as the content of ^{210}Pb decays. In ancient lead, for example from ingots found in the wreck of a Roman cargo vessel, the amount of ^{210}Pb has reduced by a factor of 10^{-27}. Such lead is suited even better for shielding than newly produced lead, but only small amounts exist. Therefore, the lead parts inside the cryostat consist of this ancient lead. This innermost shield protects the detectors from radiation emanating from the cryo equipment above.

Within the outer lead shield layer, there are 10 t of copper which shield the detectors against the residual γ-radiation from the lead. The issue of natural radioactivity does not occur with copper, as the decay times of its radioactive isotopes are so short that intrinsic radioactivity is not relevant

on the time scale of a CRESST run. Highly pure copper is commercially available, since it is an important feedstock in electrics industry.

The occurrence of radioactive ^{210}Pb is not solely limited to the shielding. One of its ancestors in the radioactive decay chain is ^{222}Rn. This noble gas emanates permanently from the walls of the cavern and if it adheres to a surface before decaying, the successor isotopes can be implanted into the surface and thereby contaminate it. In CRESST, the sensitive part of the experiment is therefore encased in a box flushed with pure nitrogen gas as means to displace the radon.

When producing, transporting and setting up the detectors, they are in danger of being contaminated by radioactive trace materials from dust, human sweat and radon from the air. In order to minimize these contaminations, the detector assembly takes place in a clean room. Transport and installation into the experimental setup happen under clean room conditions as well.

Neutrons A very dangerous kind of background are neutrons, as their signal is difficult to discriminate from a WIMP signal. In the Gran Sasso laboratory, there are four main sources for neutrons: Radioactive decays in the cavern walls can induce (α,n) reactions on light elements. Some isotopes can also be subject to spontaneous fission. High energetic neutrons can occur when nuclei are irradiated with muons. In addition, secondary neutrons can be released in spallation reactions of fast neutrons.

Light nuclei, as for example hydrogen, are the scattering partners to which neutrons can transfer their energy most efficiently. The CRESST experiment is equipped with a polyethylene (PE) neutron shield, a material that is rich in hydrogen. The shield has a total mass of 10 t and is up to 45 cm thick. Similar to the γ-shield, this neutron shield is mostly made out of bricks. Small PE pellets and water-filled volumes cover the areas which are more delicate and where PE bricks do not fit in.

2.1.3. Active Background Discrimination

With the shields and the Faraday cage closed, the trigger rate drops typically well below $0.1\,\mathrm{s}^{-1}$ per detector module. While this is a rate the DAQ system can cope with, the signal is still dominated by background. This background comes from remaining radioactive impurities in the detector holding structure or the detectors themselves.

The final step is to discriminate the background from the possible WIMP signal. As shown in Figure 2.2, the detector materials used in CRESST are

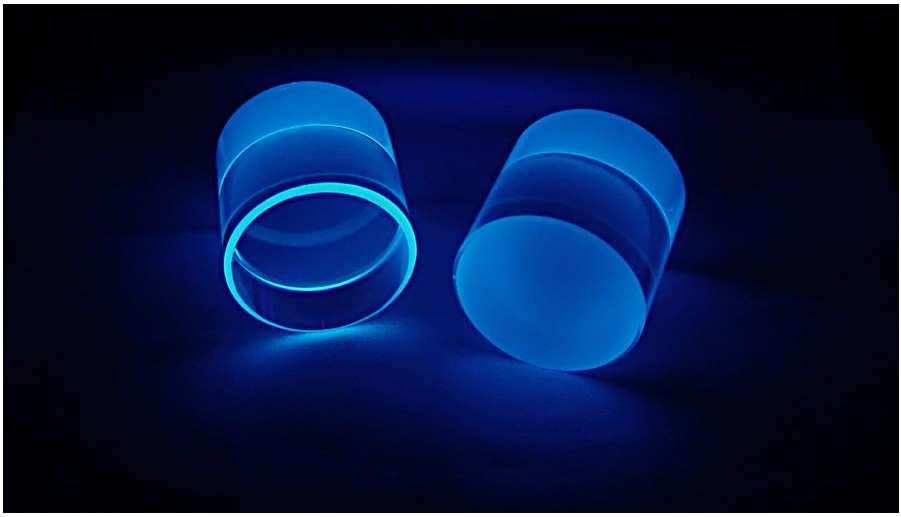

Figure 2.2.: A $CaWO_4$ detector crystal scintillating in UV light. The wavelength spectrum of the emitted light has its maximum at $\approx$ 420 nm [Zde+05].

scintillator crystals. The light yield, a measure for the proportion at which the scintillator transfers energy into light depends on the nature of the impinging particles.

This difference in light production is described as a quenching factor QF. The quenching factor is a characteristic quantity for each particle of type X. It is defined as the amount of scintillation light L_X produced by this particle compared to the amount of scintillation light L_γ produced by a γ-ray of the same energy:

$$QF_X\left(E_{\text{dep}}\right) = \frac{L_X\left(E_{\text{dep}}\right)}{L_\gamma\left(E_{\text{dep}}\right)} \tag{2.1}$$

The quenching factor is not necessarily constant for all given energy depositions E_{dep}. However, in standard CRESST data analyses the quenching factors are assumed to be constant. Table 2.1 contains an example of the values used in the recent CRESST Dark Matter analysis. An explanation of the physics behind the quenching factors can be found e.g. in [Huf10].

The criterion for the active background discrimination is the light yield. As indicated in Figure 1.4, the expected WIMP event rate has its highest

type	$1/QF$
electron	1
α-particle	4.5
oxygen	9.6
calcium	15.7
tungsten	25.6

Table 2.1.: The quenching factors used in the CRESST data analyses. Data are taken from [Ang+11].

values at low energies. Therefore, a high discrimination power is especially important in the region of low energies. For CRESST analyses it is crucial to precisely measure the light yields at low energies as this is the most interesting range for Dark Matter search.

2.2. Detector Modules

The CRESST detector modules have to be sensitive to energies in the keV range. Due to the remaining background, they need to individually identify each detected particle.

Each standard detector module in CRESST consists of two individual detectors. The phonon detector measures the energy of the particle, while the additional information of the light detector indicates the nature of the particle. Figure 2.3 shows the two detectors that constitute one module. The CRESST experiment has room for up to 33 detector modules. Recently, in March 2011, CRESST finished Run 32. In this run, there were 18 detector modules installed.

2.2.1. Module Holder

The outer case of the detector modules, called the detector holder, is made out of high-purity copper. It consists of two separate parts for the light and the phonon detector crystals. In Figure 2.3, the module is opened. The light detector is the disk-shaped object on the left side. The phonon detector is the cylindrical object on the right. Six pairs of clamps keep the phonon detector in place, whereas the light detector is held by three singular clamps. The material for these clamps is spring bronze. This renders them more elastic than pure copper.

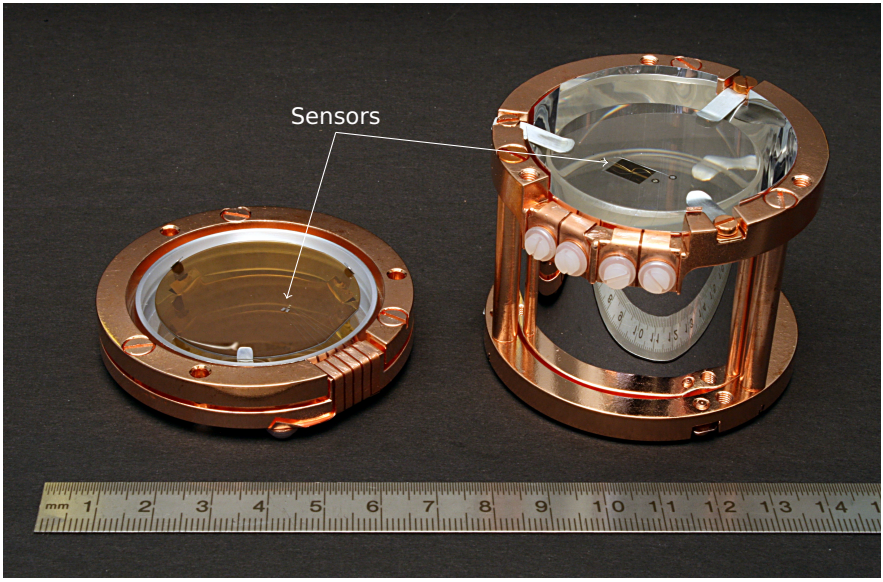

Figure 2.3.: A standard CRESST detector module before closing. The light detector is the disk-like object on the left side. The phonon detector with the big scintillator crystal is on the right side. On the surface of the crystals, one can see the sensor film structure. A reflecting foil keeps the scintillation light inside the module.

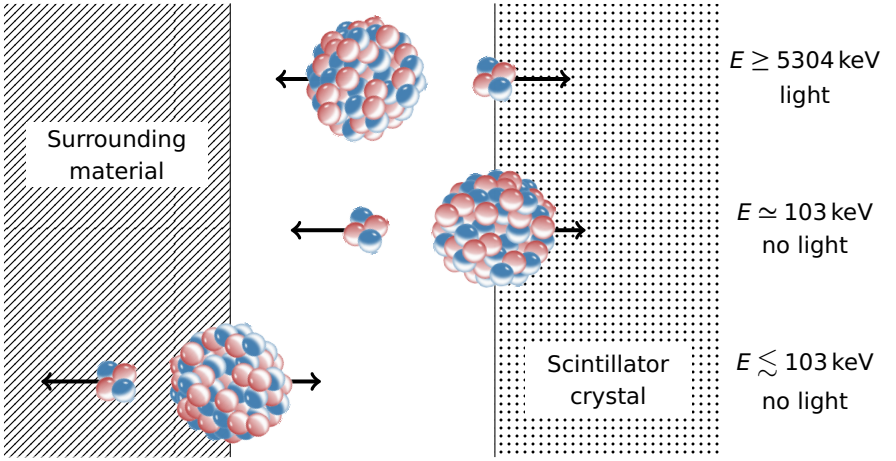

Figure 2.4.: Background events due to surface contaminations with ^{210}Po. In the first case, the event can be clearly identified as an α-particle. Without a scintillating housing, the second and third cases do not give scintillation light. There is also no characteristic energy; everything from 0 up to 103 keV is possible.

It is important for the discrimination capability of the detectors to gather the scintillation light as efficient as possible. For this purpose, a multi-layer polymeric foil covers the inside of the holder. It reflects the scintillation light and thus increases the light collection efficiency of the detector module.

The foil also serves another purpose, namely the discrimination of events due to surface contaminations with α-emitters. These contaminations could mimic WIMP events in the following way:

During the production and mounting in the cryostat, the detectors are exposed to air. As already mentioned, this air contains a fraction of ^{222}Rn, which decays to the relatively long-lived ^{210}Po. This polonium isotope is an α-emitter:

$$^{210}\mathrm{Po} \rightarrow {}^{206}\mathrm{Pb} + \alpha \qquad Q = 5407.46\,\mathrm{keV} \tag{2.2}$$

The energy is distributed between the α-particle and the ^{206}Pb-nucleus. The α-particle leaves the center of mass with an energy of 5304.38 keV [CEF99] and the nucleus recoils with the remaining energy.

The lead nucleus leaves the center of mass in the opposite direction as the α-particle (see Figure 2.4). If the α-particle hits the crystal, the high energy deposited in the crystal and the scintillation light lead to a clear identification. In the more unfavorable case, the nucleus flies towards the detector crystal while the α-particle heads outwards. A lead nucleus impinging on the crystal gives a similar signal as a tungsten recoil inside, since the mass of the nuclei are in the same order of magnitude. Additionally, the parent nucleus can be implanted in the foil. In this case, the lead nucleus loses a part of its kinetic energy while leaving the foil material.

As it was shown in Figure 1.4, tungsten recoils between 0 and $\approx$ 100 keV are a possible WIMP signal in CRESST. Thus, the impinging lead nuclei are dangerous, as they can easily be mistaken for WIMPs.

The confusion of α-induced Pb recoils with WIMP scattering can be completely avoided with a scintillating reflective foil. The α-particle from the ^{210}Po decay enters the foil and the scintillation light from the foil permits an event discrimination.

2.2.2. Phonon Detectors

Choice of Materials

As one can see in the schematic view of Figure 2.5, the largest part of a CRESST detector module is the phonon detector. Its main part is the scintillating target crystal already shown in Figure 2.2. A standard target crystal is cylindrical and has a height of 40 mm and measures 40 mm in diameter.

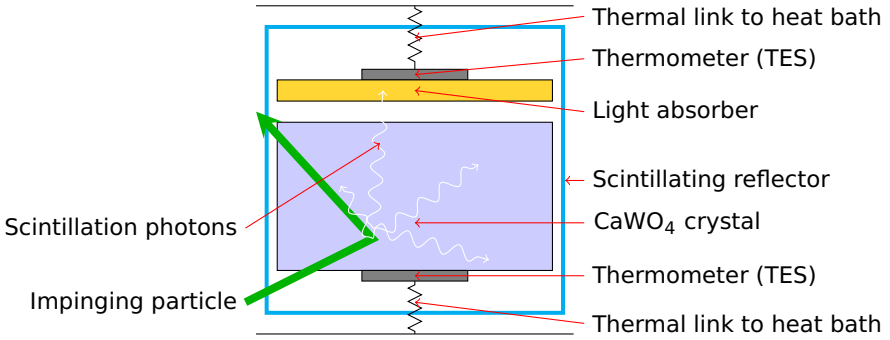

Figure 2.5.: Schematic view of a CRESST detector module.

The standard material for these crystals is $CaWO_4$, which has an emission spectrum peaked at $\approx 420\,\text{nm}$ [Zde+05], in the blue region of visible light. Since Run 31, CRESST is testing $ZnWO_4$ as an alternative material as well. $ZnWO_4$ has two advantages over $CaWO_4$: it emits more light at the same deposited energy in the crystal and its overall intrinsic radioactivity is low compared to $CaWO_4$. The light emitted by $ZnWO_4$ is greenish, in the range of $\approx 510\,\text{nm}$ [OTF80].

Having a different crystal structure and different components, $ZnWO_4$-crystals have a higher density. Their weight is about 400 g while standard $CaWO_4$ crystals have 300 g.

Principle of Operation

The following description is a simplified explanation of the CRESST detectors working as cryogenic calorimeters. In the case of phonon detectors, they consist of a cylindrical target crystal which has a sensor attached. Neglecting the scintillation, the energy deposited in the target crystal is converted to heat. The resulting change of temperature is the signal which is measured with a highly sensitive thermometer.

In this very basic explanation, the energy deposition ΔE results in a temperature rise ΔT depending on the heat capacity C:

$$\Delta T = \frac{\Delta E}{C} \tag{2.3}$$

For sufficiently small heat capacities and extremely sensitive thermometers, this temperature rise becomes measurable, even if the energy deposition is

in the order of 10 keV. In the case of inorganic insulators as $CaWO_4$, the heat capacity of the material follows Debye's T^3 law. For temperatures around 10 mK, this means that the heat capacity drops by 13 orders of magnitude compared to room temperature. Hence, the resulting rise of temperature is in the range of µK. Transition edge sensors (TES, see Section 2.2.4) can measure such low temperature variations. In Figure 2.3 the TES can be seen as a metallic structure of $6 \times 8\,\mathrm{mm}^2$ on top of the target crystal.

As this description of the signal formation is very basic, a more detailed consideration will follow in Section 2.2.5.

2.2.3. Light Detectors

The light detectors in CRESST follow the same principle of operation as the phonon detectors. The scintillation light is absobed by a crystal which converts the energy into phonons. The phonon energy is then measured by a TES.

The target crystal of a light detector is either a pure silicon wafer or a silicon-coated sapphire wafer. The diameter of the wafer is 40 mm and its thickness ≈ 0.4 mm. The TES has a size of $0.3 \times 0.45\,\mathrm{mm}^2$.

2.2.4. Transition-Edge Sensor

As mentioned before, the temperature changes that a scattering particle provokes, are in the µK range. A transition-edge sensor (TES) has an extreme temperature sensitivity, even though only over a small range. The principle of operation is illustrated in Figure 2.6. The sensor is kept at a temperature in the phase transition between normal conductivity and superconductivity. In this range, the response of the sensor's resistance to temperature changes is extremely high, allowing to detect even tiny changes.

An active feedback circuit performs the actual stabilization at the temperature called the operating point of the sensor. In CRESST, each sensor can be stabilized at its individually optimal operating point. At the operating point, the resistive response to sufficiently small variations of temperature is linear. For the superconducting tungsten thin-film structures in CRESST, the operating point is in the range of 10 mKdash30 mK.

The phonon detector TES sketched in Figure 2.7 consists of the following parts:

Tungsten film This is the actual sensitive part of the detector. The film has a thickness of 2 kÅ and an area of $6 \times 8\,\mathrm{mm}^2$. When the film absorbs

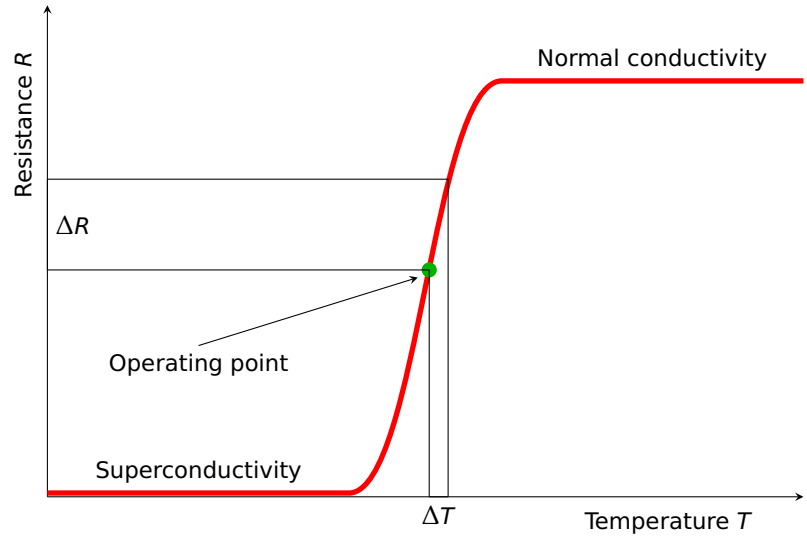

Figure 2.6.: Temperature measurement with the help of the change of resistance in the phase transition between normal and superconductivity. A slight change in temperature results in a remarkable change in resistance due to the high gradient of the resistance around the operating point.

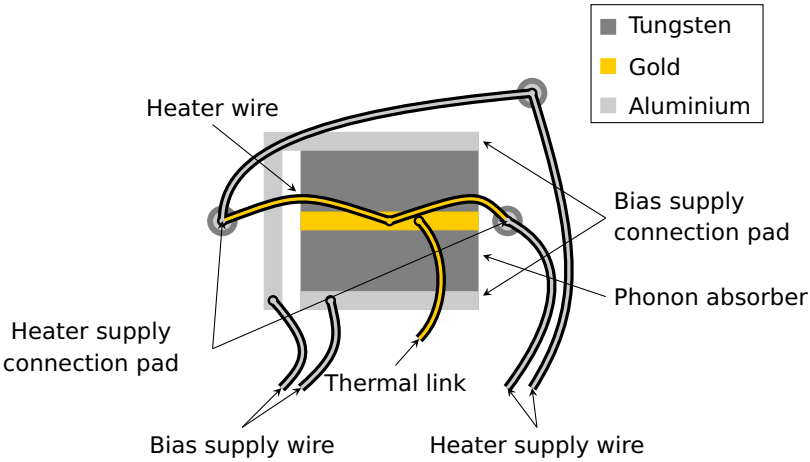

Figure 2.7.: Schematic view of the phonon detector TES.

phonons, their energy is transferred to the electron system in the film. This rise of the temperature results in an increase of the resistance.

Contact pads The electrical connection to the bias current supply is realized as a wire bond. The pads are the contact area for the bond wires on the sensor side.

Heater structure The temperature of the sensor is stabilized actively: an electrical heater keeps the temperature slightly above the base temperature of the cryostat. The heater is a gold wire stitch bond. Gold stays normal conducting and thus always dissipates heat when a current runs through. As all normal conductors, gold also has a thermal conductivity in contrast to a superconducting material. Therefore, a gold strip distributes the heat over the sensor film.

Thermal link The thermal excitation relaxes to a heat bath via a bond wire that is made of gold.

The actual fabrication of a phonon detector TES consists of the following steps: First a tungsten film is evaporated onto the crystal. The shape of the sensor is etched in a photolithographic process. Then, the aluminum contact pads are evaporated on top of the tungsten film. In the last step, the gold strip is sputtered onto the tungsten. The phonon detector TES which are produced in this configurations can reach energy resolutions below 1 keV.

The TES for the light detectors operate by the same principle. However, their shape is different to better suit the properties of the light detector.

2.2.5. Pulse Shape Formation

Equation (2.3) explains the signal development in a CRESST detector in an extremely simplified way. A more precise, quantitative description [Prö+95] (see Figure 2.8) works under the following assumptions:

An energy deposition in the crystal excites optical phonons of high frequencies. Within nanoseconds, these phonons decay to acoustical phonons with frequencies in the order of half the Debye frequency [Mar80]. These acoustical phonons decay further due to crystal lattice anharmonicities. The frequency of the population declines further but stays in the 100 GHz range for the time scale of the detector response.

In contrast to phonons near the thermal equilibrium, these phonons still have a high frequency. This is why they are called non-thermal phonons. They spread ballistically through the target crystal and couple to the electron system of the thermometer film. Inside the thermometer film, the electrons

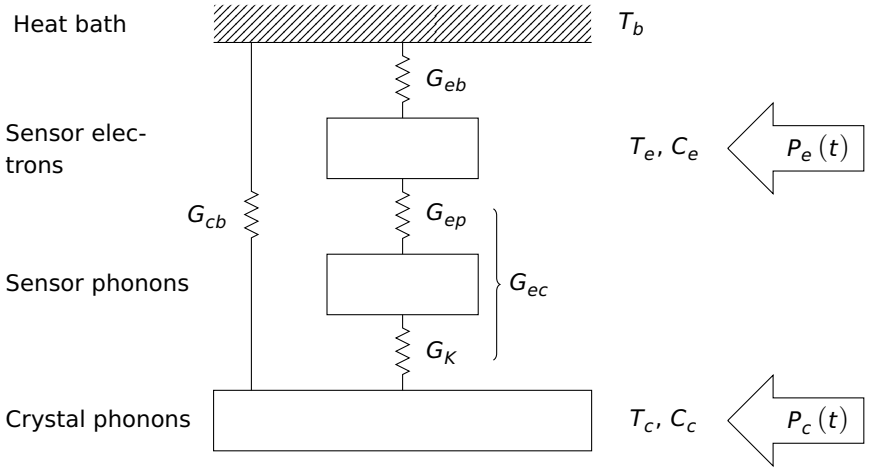

Figure 2.8.: Thermal model of the detector. T_b, T_e and T_c represent the temperatures of the heat bath, the electron system in the thermometer and the thermal phonon system in the crystal. The heat capacities of these systems are C_e and C_c. The thermal conductivities between the different parts are denoted by the various G values. $P_c(t)$ and $P_e(t)$ represent the energy transfer from the non-thermal phonons.

excite thermal phonons. At the end of the process, the energy of these phonons relaxes to the heat bath. This relaxation can take place along two paths: either directly via the thermal link on the thermometer or by coupling back to thermal phonons in the target crystal and then via the metal clamps that keep the crystal in position.

The thermalization of high-frequency-phonons feeds the power P_0 into the system. A fraction ϕ thermalizes in the thermometer and the rest $(1-\phi)$ thermalizes at the surfaces of the target crystal, probably due to surface impurities. These power inputs are P_c for the crystal, and P_e for the thermometer. They start immediately after the particle interaction which is represented by the step function $\Theta(t)$. Their amplitude decays exponentially with the time constant τ_n, as the number of non-thermal phonons reduces.

$$P_e(t) = \Theta(t) \qquad \phi \quad P_0 e^{-t/\tau_n} \tag{2.4}$$

$$P_c(t) = \Theta(t)(1-\phi) P_0 e^{-t/\tau_n} \tag{2.5}$$

For the input power P_0 one can assume that the impinging particle deposits the energy ΔE during the time τ_n. This is the time constant with which non-thermal phonons from the crystal thermalize in the system

$$P_0 = \frac{\Delta E}{\tau_n}. \tag{2.6}$$

As the overall thermalization is a concurrent process between thermalizations on the surfaces of the target crystal and in the electron system of the thermometer, the overall time constant is one over the reciprocal sum of the individual time constants:

$$\tau_n = \left(\frac{1}{\tau_c} + \frac{1}{\tau_e} \right)^{-1} \tag{2.7}$$

The thermalization in the electron system is described as follows:

$$\tau_e = \frac{2V_c}{\bar{\eta} A \langle v_\perp \alpha \rangle} \tag{2.8}$$

It depends on the probability of transmission between the crystal and the sensor α, and the phonon group velocity $v_\perp$ normal to the surface. The phonons are averaged over incidence angles and phonon modes. The probability for an absorption in the electron system is $\bar{\eta}$. The fact that the decay time depends on the target crystal volume V_c is important for pulse-shape analyses:

$$\tau_e \propto \frac{V_c}{A} \tag{2.9}$$

The time constants τ_e and τ_c determine the fractions ϕ and $(1-\phi)$ according to which the phonons thermalize:

$$\phi\tau_e = (1-\phi)\,\tau_c \tag{2.10}$$

$$\Rightarrow \qquad \phi = \frac{\tau_c}{\tau_e + \tau_c} \tag{2.11}$$

The energy flows between the systems cause variations of their temperatures. These variations can be expressed as two differential equations for the temperatures T_e of the electrons in the thermometer and T_c of the phonons in the target crystal. The changes of temperature are a result of energy depositions in the respective systems and subsequent energy transfers via the various couplings, either between the systems or to the heat bath:

$$C_e\frac{\mathrm{d}T_e}{\mathrm{d}t} + (T_e - T_c)\,G_{ec} + (T_e - T_b)\,G_{eb} = P_e\,(t) \tag{2.12}$$

$$C_c\frac{\mathrm{d}T_c}{\mathrm{d}t} + (T_c - T_e)\,G_{ec} + (T_c - T_b)\,G_{ab} = P_c\,(t) \tag{2.13}$$

The thermometer and the target crystal have heat capacities denoted as C_e and C_c. The thermal coupling between the target crystal and the heat bath is G_{ab}. G_{eb} is the coupling between the thermometer and the heat bath. The couplings between the heat bath phonons, the thermometer phonons G_K and the thermometer electrons G_{ep} can be added up reciprocally to G_{ec}.

Initially, the whole system is in thermal equilibrium with the heat bath:

$$T_c\,(t=0) \equiv T_e\,(t=0) \equiv T_b \tag{2.14}$$

The thermometer signal is the change of temperature in the thermometer:

$$\Delta T_e\,(t) \equiv T_e\,(t) - T_b \tag{2.15}$$

The solution to the two differential equations (2.12) and (2.13) has a form of

$$\Delta T_e\,(t) = \Theta\,(t)\left(A_n\left(\mathrm{e}^{-t/\tau_n} - \mathrm{e}^{-t/\tau_{in}}\right) + A_t\left(\mathrm{e}^{-t/\tau_t} - \mathrm{e}^{-t/\tau_n}\right)\right). \tag{2.16}$$

This solution is the superposition of two exponential pulses: the first one is caused by the thermalization of high frequency phonons in the thermometer, the second by thermal phonons from the target crystal coupling back to the thermometer. The amplitudes of these pulses are denoted by A_n and A_t.

In this notation, the intrinsic thermal relaxation time constant of the thermometer is called τ_{in}, the life time of the non-thermal phonons is τ_n, and the thermal relaxation time of the whole system is τ_t. The explicit values of

these time constants and amplitudes in terms of the thermal couplings and heat capacities can be found in [Prö+95].

The non-thermal component of this pulse can behave in two different ways, depending on the ratio between τ_{in} and τ_n:

Calorimetric mode If $\tau_n \ll \tau_{in}$, this means that phonons thermalize faster in the thermometer than they can relax to the heat bath. Thus, the thermometer integrates the input power. Then, the amplitude of the non-thermal component A_n corresponds to the energy deposition in the detector. This mode of operation is called calorimetric mode. In the calorimetric mode, the decay of the non-thermal phonons determines the rise time of both signal components. The decay times are determined by τ_{in} for the non-thermal and by τ_t for the thermal component.

Bolometric mode If $\tau_n \gg \tau_{in}$, the thermometer can dispose the energy faster than it is incoming. The result is that the amplitude of the non-thermal component does not correspond to the integrated energy but to the power flowing through the thermometer. This mode of operation is called bolometric mode. In the bolometric mode, τ_n determines the decay time of the non-thermal and the rise time of the thermal component.

CRESST phonon detectors work in bolometric mode while the light detectors are optimized to work as calorimeters. This is due to the fact that the energies in the light channel are extremely small, as only a small fraction of the deposited energy is converted to scintillation light.

2.3. Data Acquisition System

The DAQ system of CRESST registers the changes of resistance occurring due to energy deposition in the crystals. In order to do this, the sensors need a bias current for the resistance measurement. At the same time, a voltage-controlled heater current stabilizes the detectors in their individual operating points. The signal processing chain amplifies the signal coming from the detectors and triggers the digitizers which read out the signal. Figure 2.9 is an overview of the DAQ system. The following sections will treat the individual components.

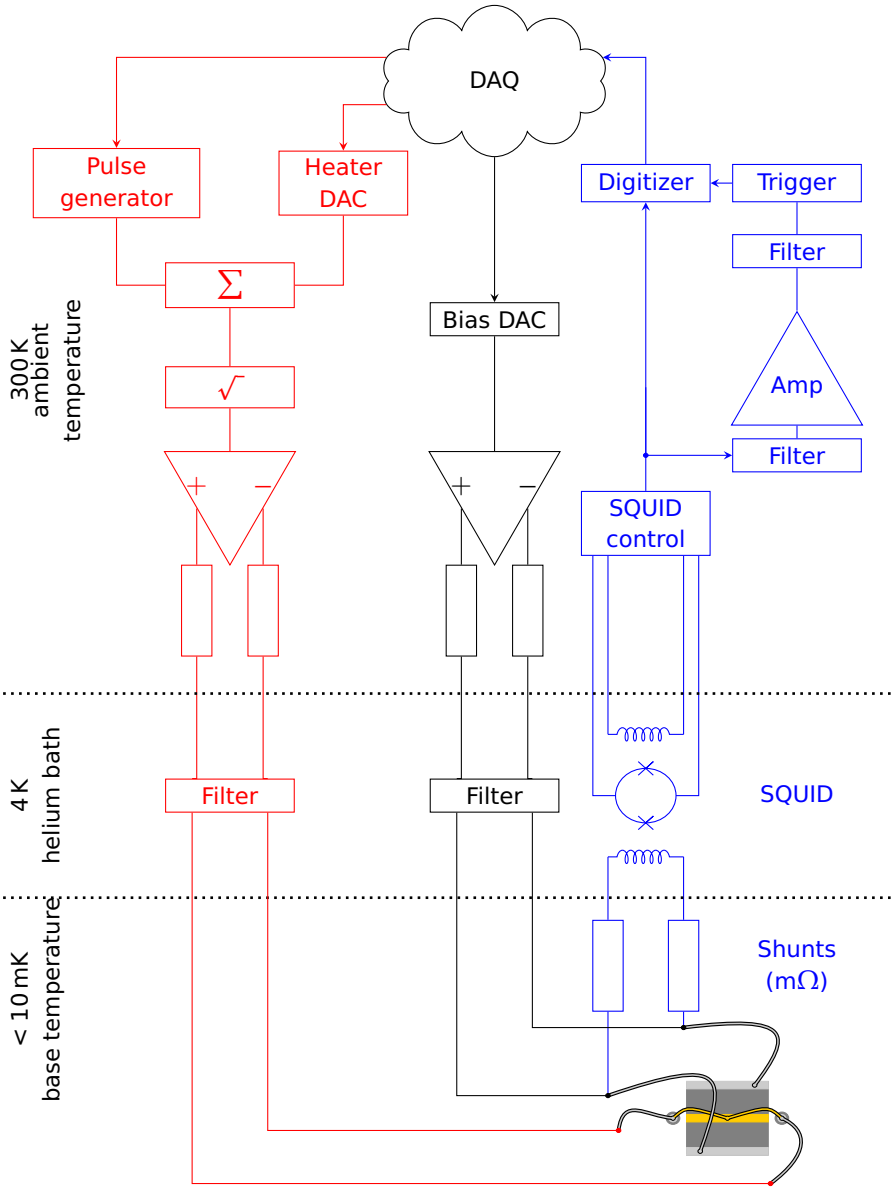

Figure 2.9.: Simplified schematics of the CRESST DAQ system. The readout circuit containing the SQUID amplification and the trigger electronics is shown in blue, the detector bias in black and the heater supply and test pulse generation system in red.

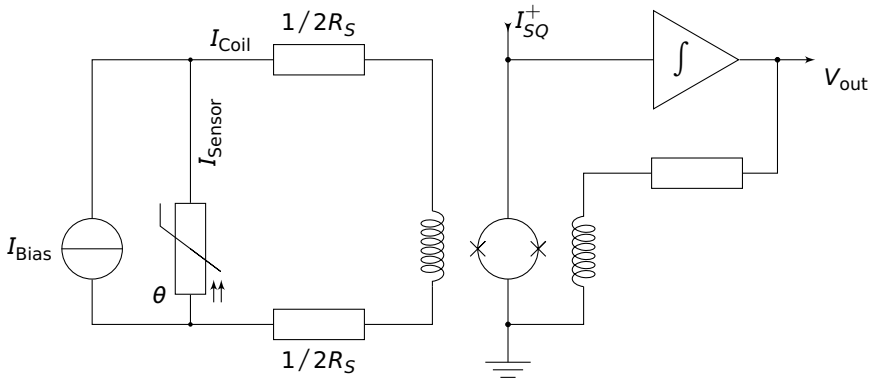

Figure 2.10.: SQUID-based resistance measurement. The change of the voltage V_{out} reflects the change of the resistance of the sensor film.

2.3.1. SQUIDs

A conventional method for measuring a resistance signal is to provide the detector with a bias current and then to digitize the voltage drop occurring over the detector. This simple method is not suitable for small signals as the ones from a TES. A SQUID (Superconducting Quantum Interference Device) provides a much better method for measuring small variations of the current.

A technical realization of a resistance measurement with a SQUID works as shown in Figure 2.10: In parallel to the resistance (the sensor film), there is a superconducting coil (input coil) and two shunt resistors whose values are $1/2R_S$ each. The bias current I_{Bias} splits up between the sensor branch and the coil branch. The ratio depends on the resistances in the branches. The input coil generates the variable magnetic field which passes through the SQUID.

A FLL (Flux-Locked-Loop) keeps the magnetic flux inside the SQUID coil at a constant level. In order to do this, there is a second coil called feedback coil which is connected to the output of the FLL electronics. Since this feedback has to compensate for the change of flux, it depends on the signal fed into the SQUID. Therefore, the output of the FLL carries information on the change of resistance in the thermometer film.

As already indicated by its name, the magnetic flux inside the SQUID is quantized. This and the properties of the FLL bear two possible sources of bad signals:

SQUID resets: The amplitude of the FLL output is limited to $\pm 10\,\mathrm{V}$. If the output transgresses this value, the FLL resets. The dynamical range of the FLL must be big enough to follow a detector pulse completely in order to avoid this.

Flux quantum losses: The change in the magnetic field can be too fast for the FLL to cope with. In this case, the FLL locks onto the following quantum state. This results in a harsh change in the output voltage of the FLL. A detector signal contaminated with such a flux quantum loss is not well-defined.

To recapitulate, the variation of the temperature in the sensor results in a variable voltage at the output of the SQUID FLL. In the overview picture (Figure 2.9), the circuit providing the bias supply is drawn in black and the circuit reading out the signal in blue.

2.3.2. Data Taking Chain

The signal which leaves the FLL is continuously digitized and the readings are written to a buffer. The digitizer resolution is 16 bits and the time base in Run 32 is $40\,\mu\mathrm{s}$. In parallel to the digitizer, a triggering module surveys whether the signal exceeds a pre-defined level. When the trigger is activated, the digitizer buffer is written to the hard disk.

In the data of Run 32, such a record consists of 8192 samples. A fraction of 2048 of these samples are the ones, which have been buffered in the time before the trigger was activated. This part of the pulse is called the pre-trigger region. A full module record contains the records of the phonon detector and its light detector(s)[1], independent on which of the individual detectors has triggered.

After the record has been written, it makes no sense to immediately arm the trigger again. It is necessary to wait for the pre-trigger buffer to fill again.

2.3.3. Heater Chain

In Figure 2.9 red color denotes the circuits that are responsible for the thermal stabilization of a detector. The heater chain is controlled by the DAQ system and its output is fed into the sensor heater. The heater signal is a

[1] In Run 32, there is one special module which has two light detectors.

superposition of two different signals: A quasi-constant heater current stabilizes the sensors at their operating points and a pulse-shaped signal is used to probe the response of the sensor.

The DAQ outputs both in the form of voltages: the artificial pulses and the nearly constant heater signal. The sum of these voltages is sent through an analog square-rooter and controls a current source which is connected to the sensor heater.

Without the square-rooter, the heater power would be proportional to the square of the sum of the input signals, since the power is proportional to the square of the current. Consequently, the response to the heater pulses would change with the power which is currently necessary to stabilize the sensor temperature. The square-rooter linearizes the relation between control voltage and heater power.

Probing the response of the sensors with artificially injected heater pulses serves two purposes:

Control pulses for temperature control The temperature changes resulting from a particle interaction are in the range of µK. The sensor must have a temperature which is stable at this precision. For this aim, the heater sends high-energy pulses in fixed time intervals of 3 s to 6 s. These so-called control pulses are energetic enough to drive the sensor into normal conductivity. The height of the response thus corresponds to the distance between the current operating point and the top of the transition curve. A PID[2] software control loop adjusts the heater current according to this value.

Test pulses as an energy gauge Every 30 seconds, the DAQ launches a pulse of a pre-defined sequence. The amplitude of these pulses varies, but usually they are all smaller than the control pulse. As the relation between the injected pulses is known, the different input amplitudes serve as a gauge for the response of the sensor. In combination with the response of the detector to a γ-source of known energy, this gauge allows to do an energy calibration of the detector. In Run 32, the calibration reaches from 5 keV to 2000 keV.

The DAQ system assigns a special flag to the injected heater pulses and records them together with the value controlling the Pulse generator. The injected energy and the response amplitude are later used for the energy calibration.

[2]PID stands for Proportional Integral Differential, meaning that the control loop reacts on the present, the historical and the extrapolated future value of the signal.

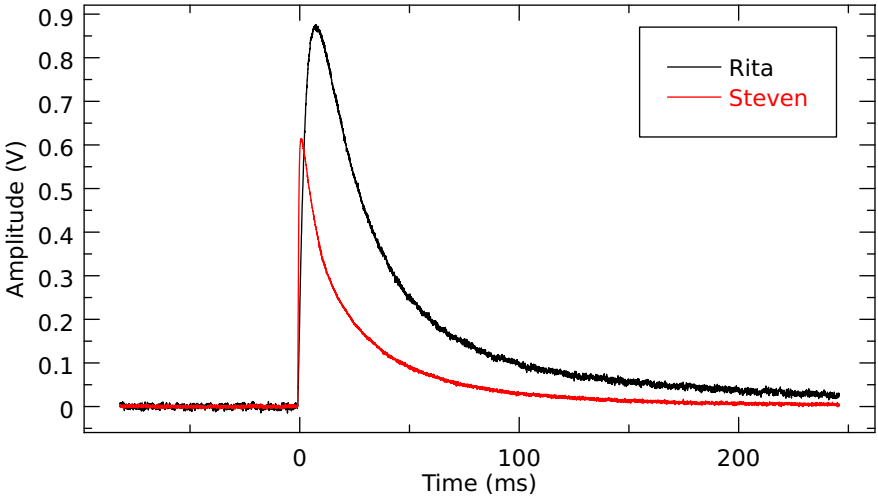

Figure 2.11.: A pulse recorded with the detector module *Rita*/*Steven* (D51/D52) in Run 32. *Rita* is the phonon detector and *Steven* the corresponding light detector of the module.

2.4. Data Treatment

The records (see Figure 2.11) which are written to disk by the DAQ system can be analyzed using a software developed in-house. Before the actual analysis starts, the software determines several fundamental parameters of each pulse.

Since a detector module contains a phonon and a light detector, the full signal of a module consists of two pulses. Furthermore, it is possible that more detectors than the one of a module see a pulses. This is the case for the test pulses and for coincident particle signals. The ensemble pulses which happen within a certain time interval are called *events*.

Elementary parameters, as for example the timing of the measurement, have to be registered already by the DAQ systems. Some simple parameters can be calculated with fixed algorithms that do not need any further assumptions. Such parameters are for example rise and decay times, pulse height etc. calculated from the pulse after a moving average filtering.

In contrast, there are several algorithms for determining the pulse height. The final step, the conversion of pulse height values to deposited energies uses the test pulses and data of a calibration source.

2.4.1. Determination of Main Parameters

Each pulse has some characteristic properties which for example describe the shape of the pulse and the timing. Some of these parameters can already be determined by the DAQ system, for example:

Time since start This is the difference between the time when the data file has been created and the time at which the trigger occurs. If several files are analyzed simultaneously, the value refers to the start of the first file.

Amplitude of test pulse This parameter is only meaningful for test pulses. It represents the voltage which was used to generate the artificial heater pulse. Since the voltage is related to the energy of the pulse, this value is necessary in order to calibrate the detector.

Onset delay in event This is the time difference between the first pulse trigger in an event and subsequent triggers of different detectors in the same event.

The first step of a data analysis is to calculate the so-called "main parameters" from the sample data of the record. The sub-program which performs this task is called CMP. The most important main parameters for this work are:

Base line This is the average level of the SQUID output without a pulse. Its value in a record is determined by averaging samples in the pre-trigger region. For displaying a pulse or for calculating its height, the base line level is subtracted from the readings so that each pulse is shown with a base line of 0.

RMS in base line This is the root-mean-square of the samples in the region which was used for the baseline calculation. Besides being necessary for the determination of the pulse onset, this parameter gives a coarse hint on the signal quality of the record.

Pulse height The pulse height is determined with a 50-sample average moving over the whole record. The maximum value minus the 50-sample baseline average determines the Pulse height parameter.

Peak position This is the sample number at which the maximum for the pulse height determination occurred.

Onset channel The pulse onset is the first sample which exceeds 10 % of the pulse height value. The parameter itself is the sample number of the pulse onset.

Rise time The rise time is the time difference between the onset of the pulse and the time at which the pulse has reached 50 % of its maximal height.

Decay time The time calculated by subtracting the onset time from the time at which the pulse has decayed to 1/e of its height. This value does not directly correspond to any of the decay times mentioned in Section 2.2.5 since the pulse height does not correspond to the amplitudes mentioned there.

2.4.2. Algorithms for Amplitude Determination

The algorithm for finding the pulse height by using a moving average over the whole record is very simple and fast. On the downside, it has a number of drawbacks and often its results are not reliable.

For example, noise can easily cause the algorithm to produce bad results: since the algorithm searches for maxima, it is biased towards finding the maximum in places where the noise and the signal add up constructively.

The second, more severe weakness of this algorithm is related to the non-linearity of the transition curve. In the analysis, one assumes a correlation between the pulse height and the energy. This is true if all pulses have the same shape. But the shape of a pulse is determined by the transition curve of the thermometer. The pulses have the same shape only as long as the deposited energy does not excite the sensor above the region where the relation between temperature and resistance is linear. Especially for higher energies this is not necessarily the case and pulse heights are systematically too small.

In all these cases, one needs to use a more sophisticated algorithm to determine the response of the detector. In the CRESST data analysis, there are two methods for this task. Both make use of the shape of a pulse in order to conclude on its height. In order to prevent confusion, the term *pulse height* is only used for the basic moving-average algorithm while in the case of the algorithms mentioned below, the term *amplitude* is used.

Standard Event Fit

The standard event fit works by scaling and shifting a template pulse so that it fits best to the recorded data (see Figure 2.12). In order to build such a so-called *standard event*, one needs to calculate the average over several hundred pulses from a narrow energy range. The set of these pulses has to be cleaned from undesired records containing for example SQUID resets or periodic noise. In addition, the pulses which form the template need to stem

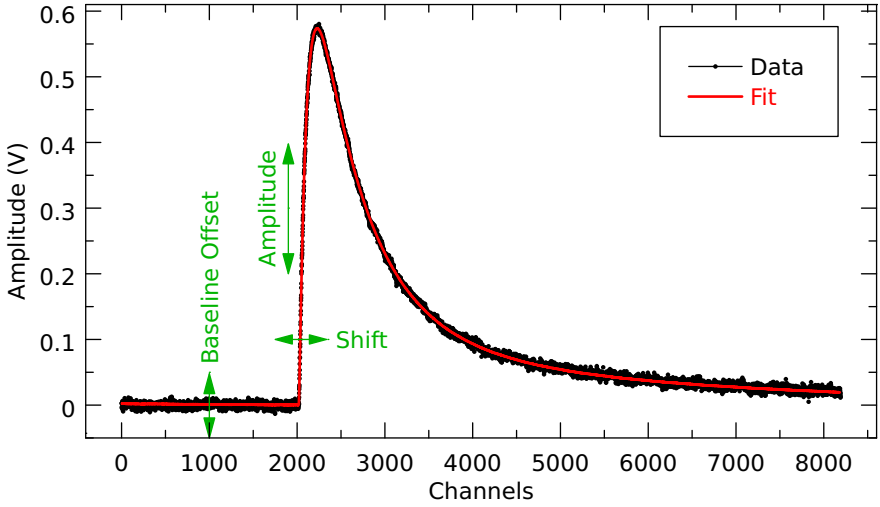

Figure 2.12.: Principle of operation for the standard event fit. The standard event (red) is fitted to the data (black). The green arrows represent the free parameters of the fit.

from the linear regime of the sensor. Averaging over these cleaned samples yields the standard event. A standard event obtained in this way has the archetypal shape of all pulses in the linear regime.

There are three free parameters for fitting the standard event to the pulses: the onset of the pulse can vary in time, the baseline can have an offset and the whole standard event can be scaled in order to reproduce the size of the pulse. This scaling is the most important parameter as it determines the amplitude of the pulse.

For comparison, the RMS value of the deviation between the fitted standard event and the original pulse is calculated. This RMS value is minimized for each parameter in order to find the best fit.

Truncated Standard Event Fit

If the excitation of the sensor is sufficiently high, the top of the pulses becomes flat. This saturation occurs because the sensor becomes normal conducting and its response to temperature changes in the normal conducting regime is very low. In this case, the deposited energy and the pulse height of the response are not correlated any more.

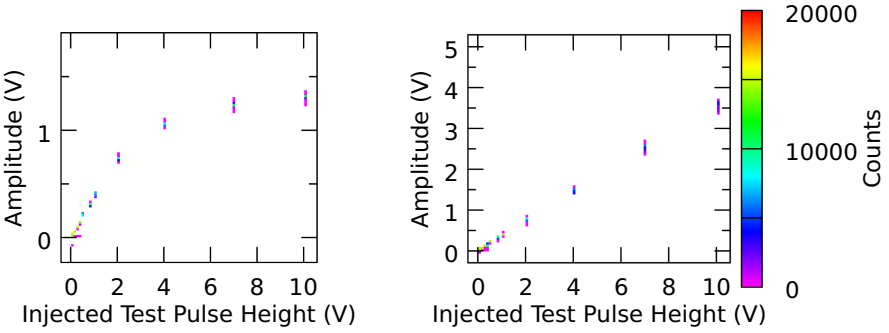

(a) Normal fit (b) Truncated fit

Figure 2.13.: The amplitudes of injected test pulses and the corresponding amplitudes of a standard event fit of the detector responses. In picture (a), the fit considers all data points of a pulse. Consequently, the response becomes non-linear if the pulses are too high in energy. With a truncated fit as in (b), the response can be linearized.

This effect is illustrated in Figure 2.13(a). Here, the test pulses of the detector *Steven* are plotted. The abscissa represents the energy of the injected pulses and the ordinate shows the response in terms of pulse amplitude. As soon as the voltage determining the height of the injected test pulse exceeds 2 V, the response behavior changes drastically. Above 4 V, the amplitude hardly increases any more. A normal standard event fit generates false results, since it relies on the correlation of pulse shape and pulse amplitude.

The solution for this problem is to truncate the data for the fit, for example as shown in Figure 2.14. Truncation means that samples above a certain height are ignored in the RMS summation which serves as an indicator for the fit quality. If only the samples from the linear range are taken into account, the energy-dependent deviance of the pulse amplitude does not influence the fit any more. This method works as long as the pulse samples below the truncation level are sufficient for concluding on the injected energy.

This truncated fit can produce amplitudes which are linearized up to a value which is much larger than the maximal pulse height. For example with *Steven*, after the truncated fit, the amplitudes of the test pulses have a linear response over the whole range of injected test pulse energies (see Figure 2.13(b)).

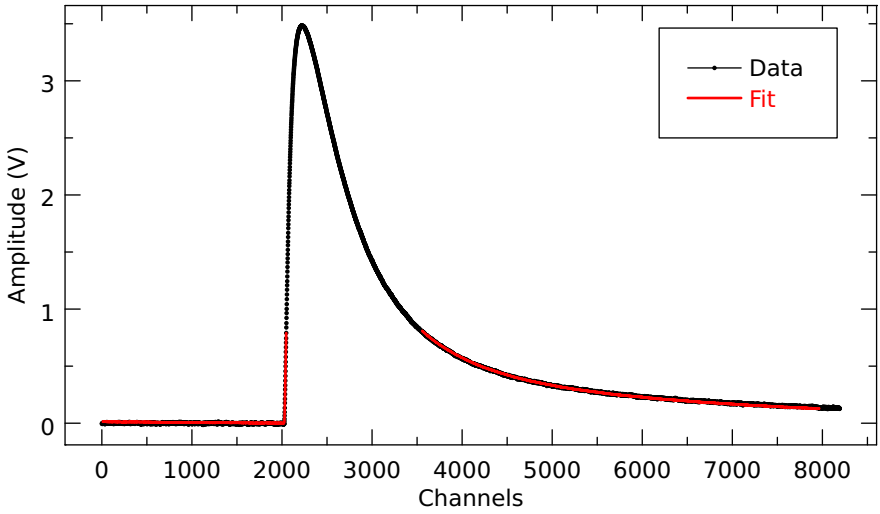

Figure 2.14.: Truncation of pulses in a standard event fit. Of the entire pulse (black), only the linear regime (red) reaching up to 0.7 V is considered for the fit (red).

Exponential Fit

Alternatively, one can fit the model described in equation (2.16) to the data. High-energy pulses have to be truncated for this method as well. This fit algorithm is much slower and less stable than the standard event fit. Usually, it is not suitable for fitting large numbers of pulses. The exponential fit is applied for the precise determination of pulse parameters such as the rise time or the decay times.

2.4.3. Energy Calibration

The pulse amplitudes which have been reconstructed by the standard event fit are responses to the energy depositions in the phonon and light detectors. After fitting, it is possible to calculate the *relative* difference between energies which excited the detectors, e.g. whether one energy deposition was twice as strong as the deposition before.

However, in order to set an *absolute* energy scale, one needs the response of the detector to at least one known energy. Then, one knew that the depositions were 100 keV and 50 keV respectively. Additionally, it is possible to

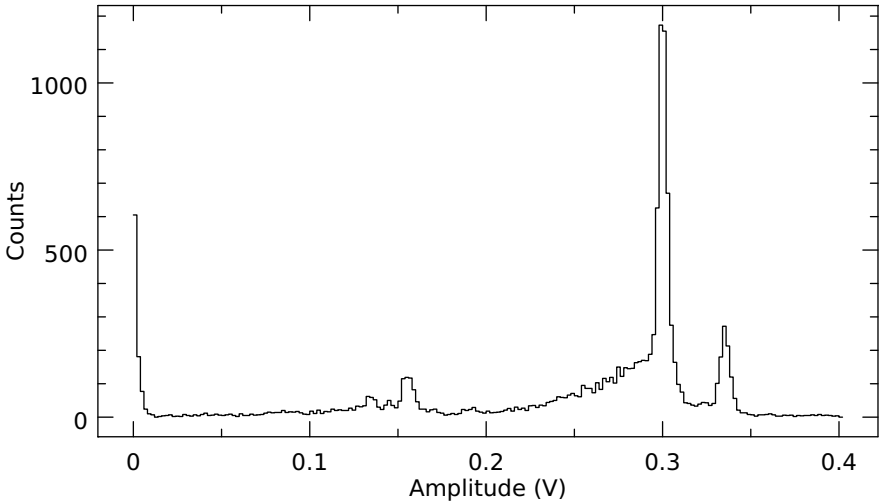

Figure 2.15.: The calibration peak of ^{57}Co in the detector *Rita*. The biggest line corresponds to 122 keV, the line right to it to 136 keV. The lines which have an amplitude of ≈ 0.15 V are escape lines of tungsten.

refine the energy scale by gauging the response of the detector over a range of energies and over time.

Calibration

The calibration is done by exposing the detectors to a known radioactive source. For the Dark Matter search in CRESST, this is usually a ^{57}Co γ-source. The main emission lines of this isotope are at 122 keV and at 136 keV. As a γ-photon in this energy range is capable of penetrating copper of a few mm thickness, it is possible to place the calibration source outside of the cryostat and to remove it when the calibration is finished. This method allows for a relatively intense calibration source, so the time necessary for the calibration can be kept short.

For phonon detectors, the two peaks are distinct, while most light detectors cannot resolve the difference in the amount of scintillation light between the 122 keV and 136 keV-lines. In the calibration that precedes a Dark Matter analysis, the phonon detector amplitude which corresponds to the 122 keV peak is interpreted as the response to an energy deposition of 122 keV in the target crystal.

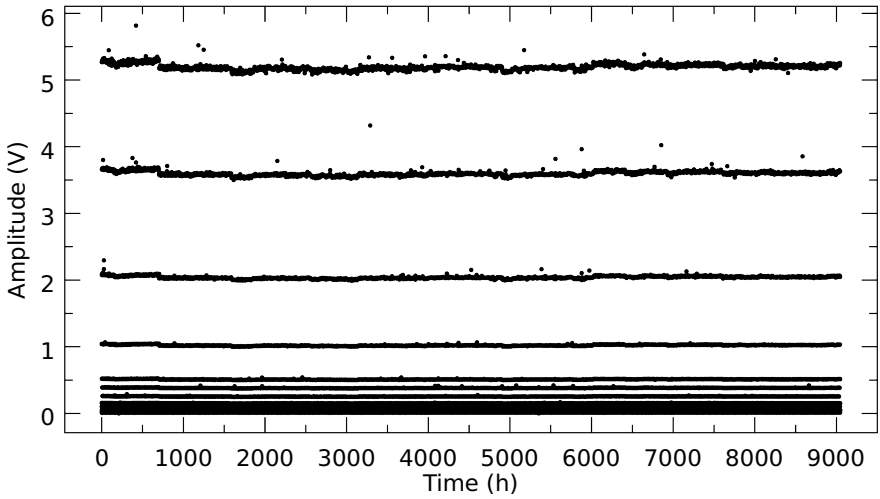

Figure 2.16.: The temporal evolution of the test pulse responses in *Rita*. Each vertical line represents pulses of one injected amplitude.

The fact that a part of the energy leaves the crystal in the form of scintillation light is neglected. In consequence, this means that other particles, e.g. α-particles, produce phonon energy readings that are slightly off scale.

As already mentioned in Section 2.1.3, the situation is more delicate concerning the light detector. The calibration peak corresponds to the scintillation light which has been generated by 122 keV γ-photons absorbed in the target. For α-particles of the same energy, the response would be lowered by the quenching factor.

In order to emphasize the particle-dependent behavior, the energy calibration of the light detector is denoted as $\mathrm{keV_{ee}}$, where the index stands for "electron equivalent". This name indicates that the energy scale is only correct under the assumption that the scintillation light was generated by electron recoils. For particle interactions which have quenching factors $\neq 1$, the energy reading of the light detector does not correspond to the deposited energy.

Gauging

Strictly speaking, the energy calibration obtained with the ^{57}Co source is only valid at 122 keVand during the time when the detector was exposed

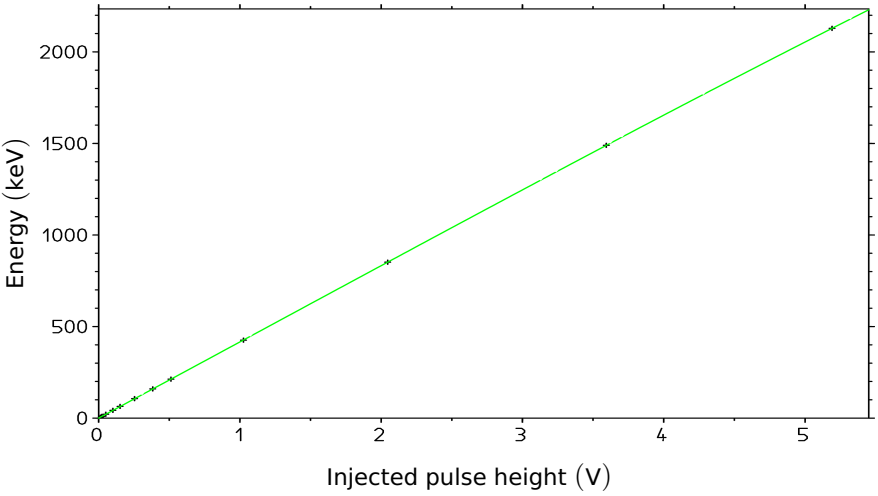

Figure 2.17.: Test pulse amplitudes versus the energy of the calibration. The green line represents the polynomial fit used to evaluate intermediate pulse heights.

to the calibration source. The test pulses provide the gauge for extending the calibration to a wider range of energies. Since they are sent over the whole duration of the measurement, they can also reveal an eventual time-dependent change of the detector response.

As already indicated in Figure 2.13, some of the test pulses saturate the detectors, so they need to be fitted using the truncated standard event. Since test pulses have different shapes than particle pulses, a dedicated test pulse standard event is required.

The temporal evolution of the test pulses of the detector Rita during Run 32 is shown in Figure 2.16. For the gauging, the time-dependence of the test pulse response amplitudes is modeled using splines. This is necessary in order to have a gauge in the time between two test pulses of the same injected amplitude.

The values of the splines at a given time are the response of the detector to depositions of discrete energies at that time. Values between these discrete energies can be interpolated with a polynomial of low order, nearly linear (see Figure 2.17). Since the energies are only known in terms of injected heater pulse height, one needs a relation between the injected pulse height and energy deposition by a particle.

The assumption is that in both cases, a heater and a particle pulse, the response of the detector is similar since in both cases the sensor of the detector reacts to thermal phonons. In the case of a particle interaction, the thermal phonons come from the thermalization processes described in [Prö+95], in the case of the test pulses they are created by the electrical current flowing through the heater wire.

Thus, if one of the test pulses had the same response amplitude as the pulses of the 122 keV γ-absorption one would know the relation between the injected heater pulse heights and the resulting energy depositions. Usually, there is no heater pulse which exactly produces a response of the same amplitude as the 122 keV peak.

Fortunately, in such a low energy range on can consider the detector response to be linear and therefore, one can linearly approximate the test pulse response using two test pulses which have a lower and a higher response than the 122 keV γ-line.

2.5. Summary

The CRESST experiment aims to detect Dark Matter by the scattering off atomic nuclei. In order to overcome the high rate of background radiation, the detectors are heavily shielded. An active background discrimination technique provides the possibility to discriminate between individual particle types.

This active discrimination technique relies on the fact that the detectors have two measurement channels: Energy and scintillation light. The scintillation light is the criterion for discrimination. It is therefore important for the sensitivity of the experiment to precisely measure the light yield of the events.

For the analysis, the detectors can be calibrated over a certain energy range with the help of a γ-source. This procedure provides a calibration which is normalized to the response to γ-events. An additional calibration, for example with α-particles will result in a slightly different energy scale and might yield additional knowledge of the detectors.

3. Composite Detectors

This chapter describes the newly-developed detector modules which have been first used in Run 31 of the CRESST experiment. The motivation for developing alternative modules will be discussed in Section 3.1.

Subsequently, Section 3.2 will describe the manufacturing of composite detectors with different types of glue.

The modified detectors produce pulse shapes which are different from those which conventional detectors produce. The difference is explained in Section 3.3, while Section 3.4 describes the impact of these changes to the recorded spectra.

The composite detectors consist of at least two different materials, a glue and one or two different types of crystals. Since the glue and the crystals have different thermo-mechanical properties, the cool-down creates stresses in the detector. Section 3.5 presents simulations of the stress which occurs in different detector geometries.

3.1. Motivation

3.1.1. Influence of the High Temperature Process on the Scintillation Efficiency

During the production of the detectors, the aluminum and tungsten layers for the sensors are evaporated onto the crystal substrate. The tungsten process temperature has an influence on the shape of the transition curve of the film. A process temperature of 450 °C has turned out to produce good thermometers.

In order to create pure films, the pressure in the evaporation system is kept at 10^{-8} mbar. This low pressure, together with the heat, changes the chemical composition of the crystal, namely by outgassing of oxygen from the $CaWO_4$ compound. A crystal with a reduced oxygen content is a less efficient scintillator [Nino5].

In order to preemptively compensate for this effect, one can anneal the crystal in an oxygen atmosphere. This oxygen enrichment can drastically

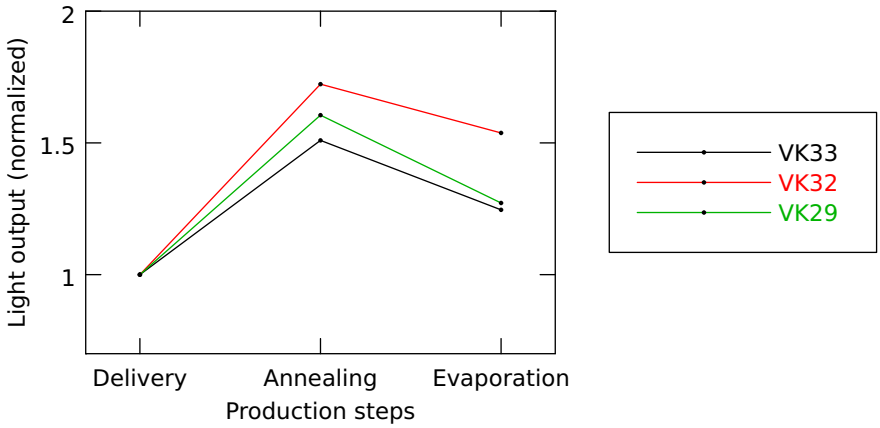

Figure 3.1.: The evolution of light output of three different crystals after different steps of the detector production. The values [Pet06] of each crystal are normalized to its respective light output at delivery time.

increase the scintillation efficiency. After the tungsten deposition, the scintillation efficiency drops again, but not as low as if the crystal had not been annealed before. Annealing the crystal after the deposition is not an option, because the hot oxygen atmosphere would compromise the quality of the sensor film.

Figure 3.1 shows this behavior using the three crystals *VK-29*, *VK-32* and *VK-33* as examples. After delivery, each crystal was irradiated with a ^{137}Cs source and the amount of scintillation light was measured with a photomultiplier. After annealing and after sensor deposition, the light output was measured again. The initial value serves as the reference for normalizing the second and third values.

In the cases of all three crystals, the annealing treatment raised the scintillation efficiency high above the initial value. For crystals which have been bought at a later time, the rise is not as high (compare Table 4.1). This happens due to the fact that crystals which have been bought more recently are already annealed by the manufacturer.

The evaporation process for producing the sensor film caused the scintillation efficiency to drop again. The high temperatures are inevitable for the evaporation of the sensor films. Nonetheless, since they reduce the scintillation efficiency, the goal is to minimize their influence on the scintillators.

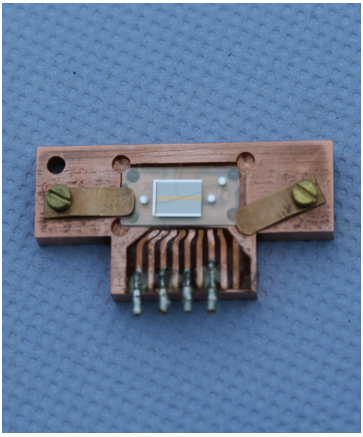

(a) A thermometer carrier mounted in a test sample hoder

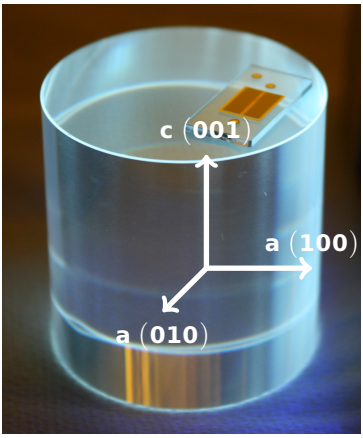

(b) The complete composite detector with the symmetry axes of $CaWO_4$

Figure 3.2.: The composite detector design: The sensor is produced separately on a small crystal. This *thermometer carrier* is glued to the *target crystal*. The crystal does not suffer the high-temperature treatment, keeping its good scintillation capabilities. In Run 32, the axes of the crystals were oriented according to picture (b)

A promising way is to produce the thermometer on a separate small crystal as in Figure 3.2(a), henceforth called the *thermometer carrier* crystal and to glue this carrier to the big *target crystal*. In this way, the corruptive effects of the high temperature treatment affect only the small carrier crystal. Figure 3.2(b) shows an example of such a composite detector.

3.1.2. Alternative Scintillator Materials

The default target material for CRESST is currently $CaWO_4$. For future runs, other materials might be interesting as well. However, their properties make it difficult to use them in conventional detectors. A composite detector on the other hand might still allow for such materials:

$ZnWO_4$: This material is easier to purchase than $CaWO_4$, since production and demand for it are higher. According to [Bavo9] it also produces more scintillation light at a given energy deposition. On the downside, the $ZnWO_4$ crystals are more brittle, they crack easily under mechanical stress. This includes thermomechanical deformations which happen during the thermometer deposition. In addition, the transparency of $ZnWO_4$ heavily decreases after a thermometer deposition.

Iodides: These materials are supposed to scintillate better than $CaWO_4$ as well. Some iodide crystals are very delicate to handle. The materials can be hygroscopic and an exposition to the atmosphere of more than a few hours turns the surface of these crystals hazy.

3.2. Manufacturing

The thermometer carriers have a size of $20 \times 10 \times 1\,\mathrm{mm}^3$. They consist of the same material as the target crystals, $CaWO_4$ or $ZnWO_4$. In order to reduce thermal deformation stress, the $CaWO_4$ thermometer carriers are cut such, that their crystal axes match those of the target crystal. Since $CaWO_4$ is a crystal of Scheelite structure, the crystal axes in the (010) and (100) direction are equivalent [YB71]. The target crystals are fabricated such, that the (001)-plane corresponds to the axial faces of the cylinder. A rotation of the carrier crystal along the axis of the cylinder therefore has no effect on the thermal deformation stress.

In the previous run, there were four composite detectors. Their targets were the $CaWO_4$ crystals *Hanna*, *Maja*, and *Rita*, as well as the fourth crystal named *$ZnWO_4$-4*. All four were assembled using commercially available

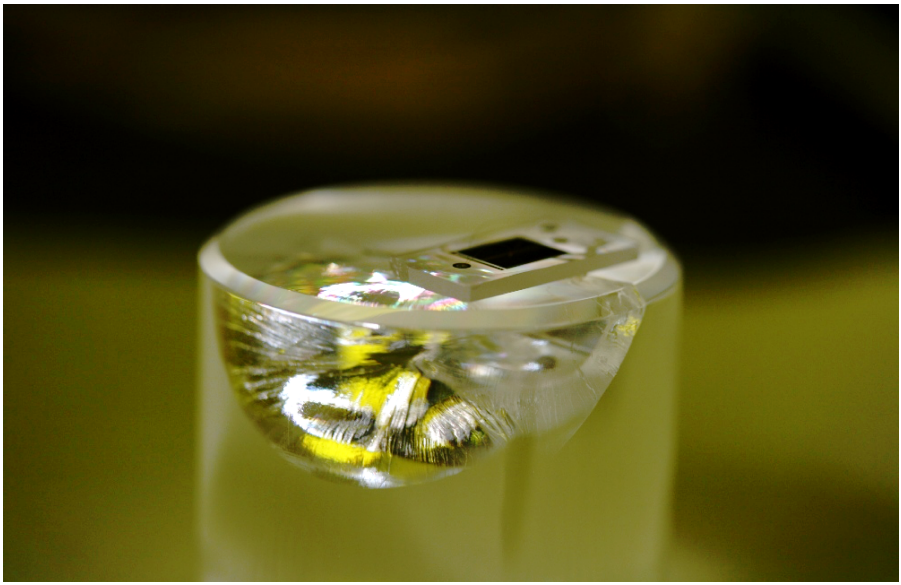

Figure 3.3.: The phonon detector *Hanna* after Run 31. The stress caused by the different thermal expansions of Araldite and $CaWO_4$ has destroyed the target crystal.

glues. The glues were Araldite®–2011 in the case of *Hanna* and EpoTek® 301–2 in the case of *Maja*, *Rita* and the $ZnWO_4$-crystal.

3.2.1. Araldite

Araldite 2011 is a scintillating epoxy resin glue. In the proof-of-principle experiment described in [Kie07], an Araldite-glued detector gave promising results. The experiment took place in a laboratory above the Earth's surface, so the detector had to be of smaller size than the Gran Sasso detectors in order to keep the background-related triggering rate low. This model detector had a cuboid shape of $20 \times 10 \times 5\,\mathrm{mm}^3$.

In contrast, in the Gran Sasso setup, the Araldite-glued detector *Hanna* never produced usable signals. After dismounting, one could see that the thermal stress of cooling the detector had caused a crack in the target crystal (Figure 3.3). It starts at the adhesive joint and extends into the bulk of the target crystal. The carrier crystal did not seem to be affected. Consequently, the setup for Run 32 did not include Araldite-glued detectors any more.

After Run 31, the module *Hanna* was disassembled in order to determine the thickness of the glue layer. The glue had a thickness of $< 20\,\mu m$ at the thinnest point and between $30\,\mu m$ and $40\,\mu m$ at the thickest point. Most of it was of a thickness around $30\,\mu m$.

3.2.2. EpoTek

EpoTek® 301–2 is a two-component epoxy resin glue, similar to Araldite®–2011. Handling EpoTek® 301–2 is more easy since the mixed glue is much more liquid in comparison to Araldite®–2011. On the one hand, the production of thin adhesive joints is much easier with EpoTek® 301–2, since it spreads better between the two crystals, behaving similar to a drop of water.

On the other hand, this means that the shape of the adhesive area can change after the glue has been deployed on the surface. Before hardening, the glue re-arranges itself due to capillary forces in the thin gap between the two crystals.

In Run 32, a second $ZnWO_4$-detector glued with EpoTek® 301–2 replaced the module containing *Hanna*. Up to now, all EpoTek-glued detectors have survived the cooling cycles.

3.3. Pulse Shapes

In a composite detector, there are two possible crystals in which an energy deposition can happen. Looking at the volumes of the parts, it is evident that most of the events happen in the target. The different crystal volumes cause different pulse shapes which permits determining where the deposition took place.

Spikes If the energy deposition takes place in the thermometer carrier, the pulse shape changes drastically, compared to a pulse from the target: As one can see in Figure 3.4, the pulses rise much faster and the time constant for their decays are much shorter than normal. This is due to the fact that the time constants depend on the volume in which the energy deposition takes place (see equation (2.9)). The volume of the carrier is much smaller than the volume of the target. Therefore, the carrier pulses are much faster.

Normal Pulses In the target crystal, the phonons that have been created due to an energy deposition cannot directly couple to the electrons of the

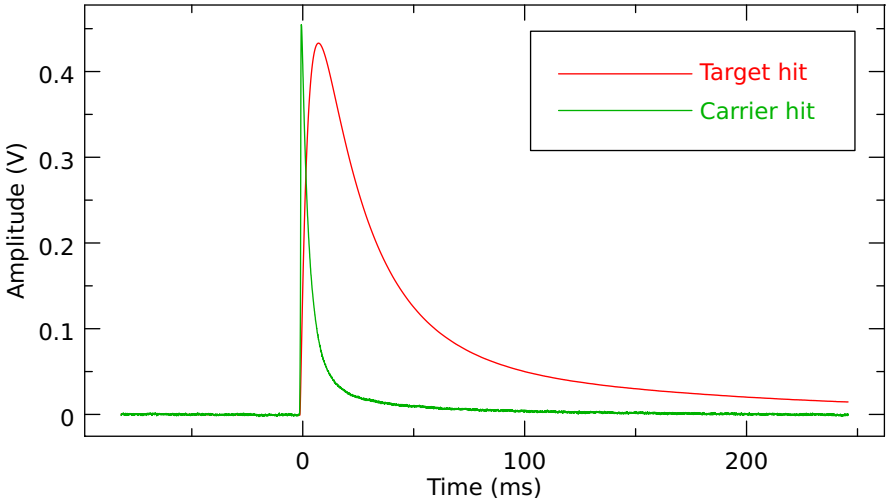

Figure 3.4.: Comparison between the signals of particle interactions in the target crystal and thermometer carrier parts of a composite detector.

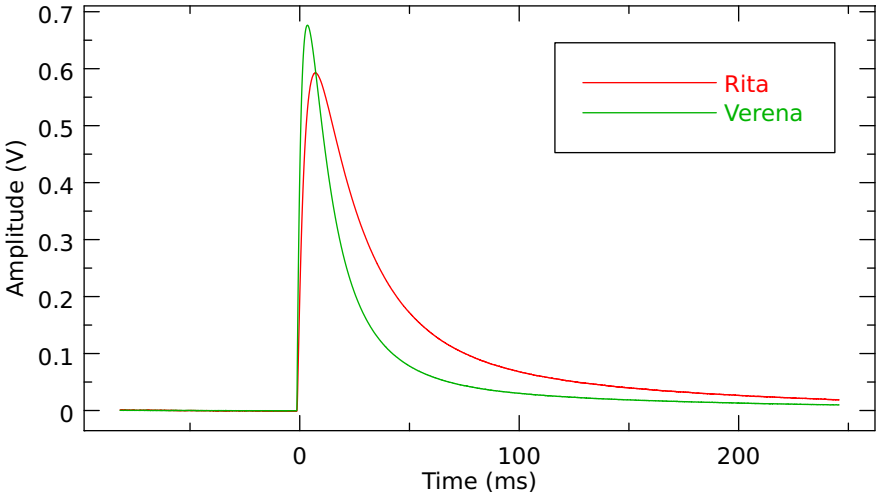

Figure 3.5.: Comparison between the signals of a conventional (*Verena*) and a composite detector (*Rita*).

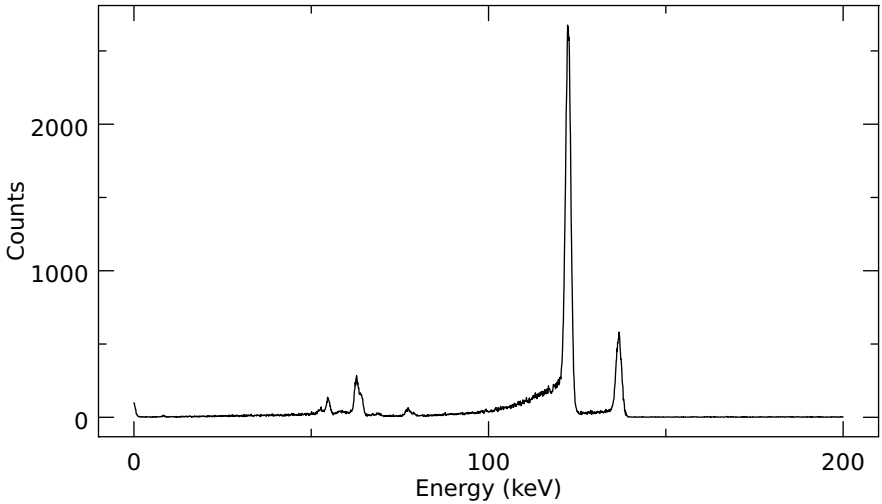

Figure 3.6.: Calibration spectrum recorded with the conventional detector *Julia*.

sensor. Instead, they first have to couple to the phonons in the glue which then couple to the phonons in the thermometer carrier crystal.

Although the intermediate steps cause a slight deformation in the pulse shapes, the resulting signal of a composite detector is not significantly different from the signal of a conventional detector: in Figure 3.5, there is a comparison between the standard events of the conventional detector *Verena* and the composite detector *Rita* from that run. The signal of *Rita* has a longer decay time than the one of *Verena* but the record length is sufficient to observe the interesting part of the pulse.

3.4. Spectral Quality

The main information which is extracted from the detector data are energy spectra. Thus, one has to compare the conventional and the composite detectors with regard to the quality of the spectra as e.g. the resolution of spectral lines. The data from the calibration of Run 31 with the ^{57}Co calibration source are a suitable reference.

The Figures 3.6 and 3.7 are calibration spectra recorded with the detectors *Julia* and *Maja*. One can see the 122 keV and 136 keV peaks from the ^{57}Co source. The escape peaks of γ-photons from the ^{57}Co are visible as well.

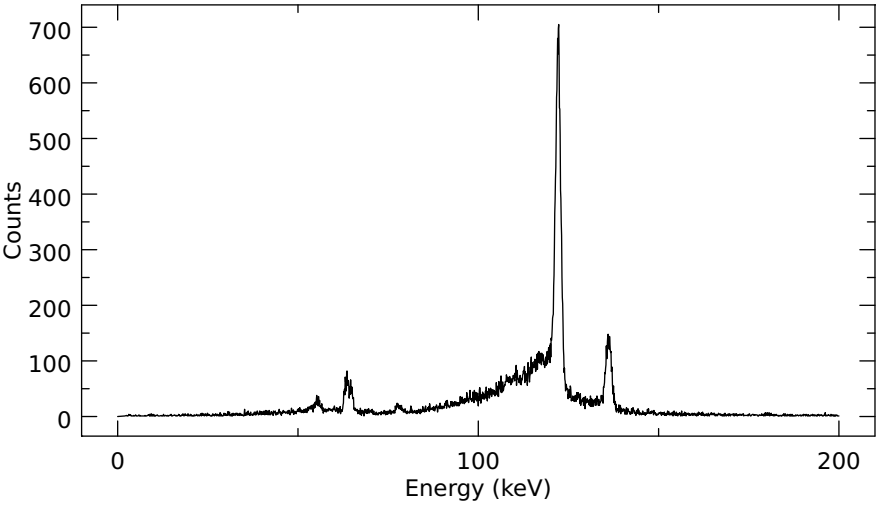

Figure 3.7.: Calibration spectrum recorded with the composite detector *Maja*.

Name	FWHM (keV)		Comment
	122 keV-Peak	Baseline	
Julia	1.92	0.99	standard
Maja	1.98	0.80	EpoTek
Rita	1.98	0.41	EpoTek
Hanna	2.62	0.44	Araldite, broken
$ZnWO_4$	1.81		EpoTek, Measurement by [Bav09]

Table 3.1.: Comparison of the FWHMs of the 122 keV calibration line. The module *Julia* has a standard phonon detector while the others have composite detectors.

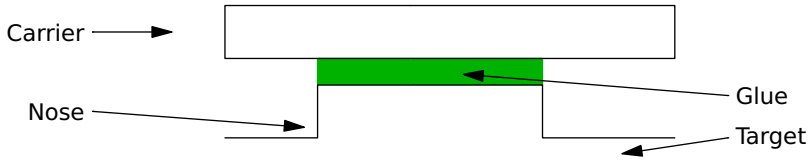

Figure 3.8.: Design for a modified target crystal. The idea is to reduce the stress and thereby fake signals created due to thermal relaxation by adding a "nose"-like structure to the target crystal. If the glue and the nose have the same dimensions, there should be less thermo-mechanical stress in the target crystal because the nose provides less material that can exercise a force in the glue.

These peaks are due to excitation of tungsten atoms where the incoming γ-ray loses a part of its energy by exciting X-ray fluorescence in the tungsten. If then the X-ray is not seen by the detector, its energy does not show up in the measurement.

When visually compared, the two spectra do not bear a remarkable difference. The spectrum recorded with *Rita* has a bit less statistics which is due to the position of the calibration source relative to the two detectors. The resolutions of the two detectors can be determined via the FWHM of the 122 keV peak. Table 3.1 shows the values for all composite detectors of Run 31 and the detector *Julia* for comparison. The resolution of the EpoTek® 301–2-glued composite detectors is in the same range as the resolution of conventional detectors. The detector which was glued with Araldite®–2011 has a worse resolution. The reason might be the cracks which disturb the propagation of phonons in the crystal.

3.5. Stress Simulations

Apart from the sensor film, a composite detector consists of at least two different materials, namely the glue and the crystals. Having different thermo-mechanical characteristics, they contract to a different extent when cooling down. Since both materials are connected, the different contraction rates cause mechanical stress. If this thermo-mechanical stress exceeds the value which a material can maximally sustain, the material cracks.

Each of these cracks is an energy deposition in the detector. Since cracks do not ionize the material, they do not excite any scintillation center. Therefore, the crack formation could fake signals of particles with a high quench-

ing factor. This means that depending on the model implications, the cracks could be falsely interpreted as WIMPs. Even more severe cracks can destroy the whole crystal as in the case of *Hanna*.

The thermo-mechanical stress depends on the material characteristics as well as on the geometry of the detector. With a good choice of these properties, it could be possible to reduce the risk of producing cracks in the crystal. Geometrical modifications as the one shown in Figure 3.8 could possibly also influence the stress. Such a nose might help to avoid areas of large thermo-mechanical stress in the target crystal.

The rest of this chapter shows simulations of the composite detector during cool-down. The simulations address the following questions:

- Is there a need for aligning the target crystal and thermometer carrier axes?
- Do flat glue spots reduce the stress?
- Is it beneficial to limit the diameter of the glue spot?
- Could an additional nose reduce the stress?

Before presenting the results of the simulation, some basic parameters of a thermo-mechanical problem will be discussed.

3.5.1. Theory of Elasticity of Materials

Stress

In solid state physics, the force F which acts on a material is usually normalized to the surface A. This yields the so-called stress σ:

$$\sigma = \frac{F}{A} \tag{3.1}$$

In a three-dimensional space, there are three possible directions for the stress: One normal to a surface and two in parallel to it. The parallel stresses are commonly called shear stress.

In order to investigate the load of a material, one considers the stress on three cut planes normal to the unit vectors $\vec{x}_i$ (see Figure 3.9). The three stresses (one normal, two shear) on each cutting plane are named σ_{ij} according to the direction of the plane normal $\vec{x}_i$ and the direction of the force $\vec{x}_j$. This results in a 3×3 stress tensor $\hat{\sigma}$. This general case can be simplified by

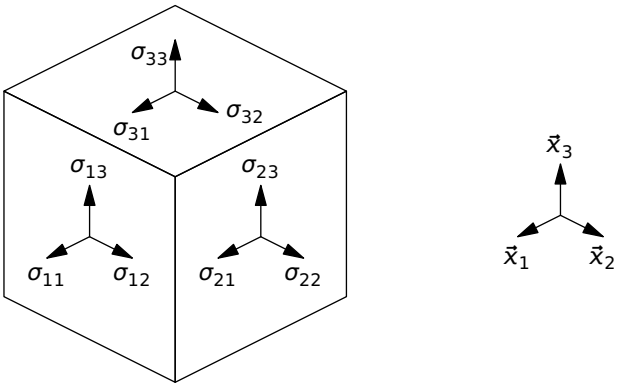

Figure 3.9.: Components of the stress tensor σ.

assuming that no angular momentum transfer occurs. Then, always two of the components are related such that

$$\sigma_{ij} = \sigma_{ji} \tag{3.2}$$

which makes the stress tensor symmetrical.

It is always possible to choose a coordinate system in which the surfaces are aligned such that no shear but only normal stress components occur. This coordinate system is called the system of the *principal axes*. The three remaining stress components are accordingly called principal stresses. The principal stresses have only one index number, usually in Roman style. They are named σ_I to σ_{III} where σ_{III} is the biggest and σ_I the smallest component [RHB08].

Deformation

When being exposed to a force, a solid can change its shape in different ways, depending on the force and the material properties:

Elastic Strains Similar to the stress, there are two types of deformation: normal strain (orthogonal) and shear strain (in parallel). Figure 3.10(a) depicts the deformation of a rod which is exposed to a force F_x that is pulling in the x-direction. Without a load, the rod has a length l_0. When applying the load, the rod elongates to a length of $l_1 = l_0 + \Delta l$.

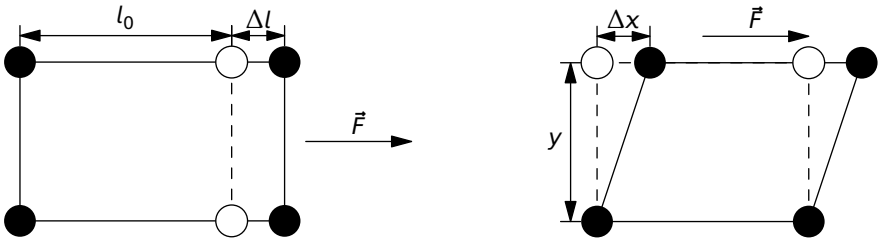

(a) Normal strain (b) Shear strain

Figure 3.10.: Normal and shear strain

The strain ε in x-direction is defined as the change in length over the original length:

$$\varepsilon = \frac{\Delta l}{l_0} \tag{3.3}$$

The concept of shear deformation is illustrated in Figure 3.10(b), where a force F_x is pulling the material in x-direction. However, in this case the material is not fixed on a surface that is perpendicular to the force but in parallel to it. The reaction of the material is called shearing. In this example, the shear γ is defined as the displacement in x-direction depending on the position in y-direction.

$$\gamma = \frac{\Delta x}{y} \tag{3.4}$$

The general case of a three dimensional deformation including both shear and strain is described by a symmetrical 3×3-tensor $\hat{\varepsilon}$:

$$\varepsilon_{ij} = \varepsilon_{ji} \tag{3.5}$$

As in the case of the stress tensor, the index i corresponds to the surface that is normal to the deformation. The index j indicates the direction of the deformation again. This so-called strain matrix contains all possible normal and shear strains occurring in a unit volume.

Poisson's Ratio When stretching an object like e.g. a rubber tape in x-direction, the material contracts along the y- and z-axes. Figure 3.11 illustrates this behavior in a simplified two-dimensional case:

A force $\vec{F}$ pulls at a quadrangular body along the x-axis and elongates it by Δl_x. At the same time, it becomes thinner by Δl_y in the y-direction.

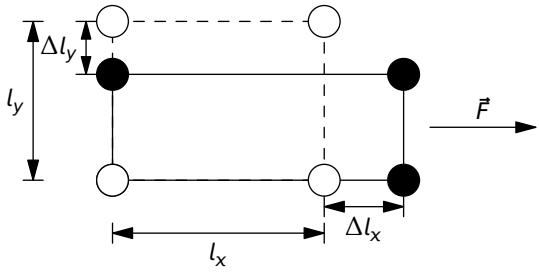

Figure 3.11.: The deformation described by Poisson's ratio.

The relation between deformations in different directions is described by Poisson's ratio ν. It is the relation of the relative changes in length:

$$\nu = \frac{\frac{\Delta l_x}{l_x}}{\frac{\Delta l_y}{l_y}} \tag{3.6}$$

The general case for three-dimensional objects requires a set of three different Poisson's ratios ν_{yz}, ν_{zx}, and ν_{xy} which relate the deformations in all three directions.

Elasticity

In the one-dimensional case of a spring with an elasticity D, the force F depends linearly on the excursion Δl. This behavior is known as Hooke's law:

$$F = D\ \Delta l \tag{3.7}$$

Generalized to three dimensions and anisotropic materials, Hooke's law, instead of relating the force and the excursion of a rod, describes the stress depending on the strain:

$$\sigma_{ij} = C_{ijkl}\varepsilon_{kl} \tag{3.8}$$

The counterpart of the spring constant D is the compliance matrix $\hat{C}$, or C_{ijkl} in component notation. It describes the specific elastic properties of the material. Due to symmetry reasons only 36 of its $3^4 = 81$ initial components are independent. Making use of this fact, the compliance matrix is usually written in the so-called Voigt notation, turning it into a 6×6 matrix. In a cartesian coordinate system with the directions x, y and z, the Voigt notation

abbreviates pairs of indices in the following way:

$$1 \equiv xx\,; \qquad 2 \equiv yy\,; \qquad 3 \equiv zz\,; \qquad 4 \equiv yz\,; \qquad 5 \equiv zx\,; \qquad 6 \equiv xy \tag{3.9}$$

With the strain and stress tensors in vectorial form, Hooke's law yields:

$$\begin{pmatrix} \sigma_1 \\ \sigma_2 \\ \sigma_3 \\ \sigma_4 \\ \sigma_5 \\ \sigma_6 \end{pmatrix} = \begin{pmatrix} C_{11} & C_{21} & C_{31} & C_{41} & C_{51} & C_{61} \\ C_{12} & C_{22} & C_{32} & C_{42} & C_{52} & C_{62} \\ C_{13} & C_{23} & C_{33} & C_{43} & C_{53} & C_{63} \\ C_{14} & C_{24} & C_{34} & C_{44} & C_{54} & C_{64} \\ C_{15} & C_{25} & C_{35} & C_{45} & C_{55} & C_{65} \\ C_{16} & C_{26} & C_{36} & C_{46} & C_{56} & C_{66} \end{pmatrix} \begin{pmatrix} \varepsilon_1 \\ \varepsilon_2 \\ \varepsilon_3 \\ \varepsilon_4 \\ \varepsilon_5 \\ \varepsilon_6 \end{pmatrix} \tag{3.10}$$

The elastic properties of $CaWO_4$ are given in the form of a such a compliance matrix [GHJ73]. However, the simulation software requires material data in the form of the so-called Young's and shear moduli E and G and the Poisson ratio ν.

Therefore, one needs to convert the values from one form into the other. The equations in [PW07] help to state the relations between the two different notations, using a third form, the stiffness matrix $\hat{S}$. This matrix describes the inverse of Hooke's law:

$$\varepsilon_{ij} = S_{ijkl}\sigma_{kl} \tag{3.11}$$

With this information, one can transfer the stiffness matrix into the compliance matrix and vice versa by using the relation

$$\hat{S} = \hat{C}^{-1} \tag{3.12}$$

Young's moduli $E(\vec{n})$ describe the connection between the normal stresses and strains along the unity vector $\vec{n}$:

$$\frac{1}{E(\vec{n})} = n_i n_j S_{ijkl} n_k n_l \tag{3.13}$$

The components parallel to a surface are handled by the *shear moduli* $G(\vec{n}, \vec{m})$

$$\frac{1}{4G(\vec{m}, \vec{n})} = m_i n_j S_{ijkl} m_k n_l \tag{3.14}$$

The connections between the stiffness matrix and Poisson's ratios are given as

$$\nu(\vec{m}, \vec{n}) = -\frac{m_i m_j S_{ijkl} n_k n_l}{n_p n_q S_{pquv} n_u n_v} \tag{3.15}$$

In the case of EpoTek® 301–2, the material characteristics are given in the E, ν form directly [Cea+06]. With these parameters, one can model the *reaction* of a material which is exposed to certain forces and displacements. The following step is a description of the *cause* for these forces and displacements.

Thermal Expansion Coefficient

The fact that rising temperatures make most objects expand, while falling temperatures make them contract, is common knowledge. Assuming a linear relation between the change of length Δl and the temperature ΔT leads to the thermal expansion coefficient α.

For an object with a length l, the change of length goes with the temperature as follows:

$$\Delta l = l\alpha\Delta T \tag{3.16}$$

The thermal expansion coefficient is thus:

$$\alpha = \frac{1}{l}\frac{\Delta l}{\Delta T} \tag{3.17}$$

The glue as an amorphous material has only a single value valid for all directions. However, $CaWO_4$ is a material with an anisotropic expansion behavior, having one expansion coefficient for the a-axes and another one for the c-axis.

When extending the description from a one-dimensional to a three-dimensional case, one has to take into account such a behavior by defining different expansion coefficients for the different spatial directions i:

$$\alpha_i = \frac{1}{l_i}\frac{\mathrm{d}l_i}{\mathrm{d}T} \tag{3.18}$$

In addition to this, α must not necessarily describe a thermal expansion *constant* but the values α_i themselves can depend on the temperature:

$$\alpha_i = \alpha_i(T). \tag{3.19}$$

The thermal expansion coefficients used for the simulation were measured by [YB71] in the case of $CaWO_4$ and by [Cea+06] for EpoTek® 301–2.

Criterion for Damage

With these characteristics of the material known, it is in principle possible to calculate the reaction of a composite detector to a cool-down. However, this does not necessarily mean that one can decide whether geometrical configurations of the detector are good or even possibly destructive. A cool-down always creates strains and related stresses in the material. As long as the displacements are within the limits of elasticity, these effects are reversible and therefore do not cause permanent damage in the form of cracks.

One way of investigating whether a material suffers permanent damage is to determine if its deformations change from elastic to becoming plastic. The transition occurs when the so-called stress criterion σ_c exceeds the characteristic yield stress R_y of the material

$$\sigma_c \geq R_y. \tag{3.20}$$

The quantities σ_y and R_y are scalars. While R_y is a material-dependent quantity which one can measure, there are different possible assumptions for σ_c. The decision which assumption to make is purely empirical. For ductile materials as metals, there are stress theories as e.g. the von-Mises-hypothesis in which the stress criterion contains all the components of the stress tensor:

$$\sigma_y = \sqrt{\frac{1}{2}\left(\left(\sigma_{11}-\sigma_{22}\right)^2 + \left(\sigma_{22}-\sigma_{33}\right)^2 + \left(\sigma_{11}-\sigma_{33}\right)^2 + 3\left(\sigma_{23}^2+\sigma_{13}^2+\sigma_{12}^2\right)\right)} \tag{3.21}$$

Such a criterion respects the fact that deformations of the material in different directions might compensate for each other. Then, the plastic deformations might prevent the material from breaking.

When pulling a wire for example, the wire at first is only deformed elastically. When the force becomes stronger and starts to deform the material beyond its limits of elasticity, the wire will become irreversibly longer and thinner. However, the wire is not completely destroyed. Only as soon as the deformations become too big or too fast for the material to cope with, the wire will rip.

$CaWO_4$ on the other hand is brittle and not ductile, at least at room temperature and below. Therefore, one can assume that sufficiently high deformations will not result in a plastic deformation of the material but will break the crystal instead. In such a case, the stress criterion is much simpler than in the case of ductile materials. The stress criterion is simply the largest primary stress [Wit10]:

$$\sigma_c = \sigma_{III} \tag{3.22}$$

Since no measurement of the temperature-dependent yield stress R_y for $CaWO_4$ exists, one cannot determine whether the crystal actually cracks under the conditions occurring in the simulations. However, one can assume that the crystal will not crack if the stress criterion is not too high. Thus, the investigation within this work aims at finding configurations which keep the greatest principal stress σ_{III} at a low level.

3.5.2. FEM Method

FEM in General

Analytically determining the maximum primary stress which occurs in a cold composite detector would pose an extremely complicated task. One would need to set up an equation or a set of equations in order to model

- the geometry of the composite detector,
- the thermo-mechanical behavior of its components, taking into account the anisotropic behavior of the $CaWO_4$ parts,
- and finally the resulting deformation and stresses when the glue and the crystals are forced to interact.

Subsequently, one would have to find the maximum of the function modeling the primary stress distribution inside the detector.

It is doubtful, whether one could resolve such a problem with purely analytical methods. Instead, this work makes use of a numerical method known as the Finite Element Method (FEM).

This method can help to solve complex problems by dividing them into a set of smaller problems. The small problems then are resolvable. Since FEM is a numerical method, the possibility to solve complex problems with the FE method comes at the cost of having only an approximative solution.

The first step is to split the object into smaller and simpler geometrical shapes, called the volume, surface and line *elements*. Common basic elements are e.g. triangles and quadrangles which form tetrahedra and prisms.

When the geometry model exists, the next step is to model the physical interactions between the *nodes*, the points that delimit the individual elements. In a mechanical problem, this could be the position of the points related to the forces acting on them and the elasticity of the material between them. In case of a diffusion problem on the other hand, one could model the concentration e.g. of a mineral dissolved in a liquid related to the diffusion between different locations in the liquid.

If the individual elements were completely isolated, the model would be of no use. Therefore, one has to set up connections that relate the individual elements. Specifying boundary connections makes it possible to model external influences as e.g. mechanical forces or temperature gradients.

If not explicitly stated otherwise, the following text concerns the thermo-mechanical problem of the composite detectors. A more detailed, general explanation of the principles behind FEM can be found e.g. in [Abb11] or in [Wit10], just to name a few.

Software

In general, the solution of a problem with the FE method consists of three major steps. Each of these steps is treated by one or more programs.

Pre-Processor The pre-processor is used in order to create a mathematical model of the problem. First, one needs to create a geometrical model of the composite detector. The discretization of the geometrical model produces the so-called *mesh* which consists of the finite elements. Subsequently, one assigns the physical properties of the different materials to corresponding regions of the mesh. In the last step, one specifies boundary conditions corresponding to the mechanical and thermal loads which act on the detector.

Solver The mesh together with the material data and the boundary conditions are the input data for the solver. The solver calculates the reaction of the element nodes to the loads. It assembles the results into two fields. The first field contains the forces occurring inside and among the elements. The second field describes the displacement of the individual nodes.

Post-Processor The post-processor uses the result of the solver in order to generate further information, as for example the field containing the primary stresses. The user-interface which displays the final result is also a component of the post-processor software.

The FEM calculations in this thesis were performed with the help of the distribution of free FEM software called SALOME-MECA. The two relevant packages of this distribution are SALOME and Code_ASTER. SALOME provides a GUI with which one can specify the geometrical properties of the detector and a set of algorithms for generating a mesh according to the geometry. Code_ASTER is used for providing the model with physical properties. It contains solvers for various types of problems and provides means for post-processing the result in order to extract the primary stresses. Finally, one can observe the result of the calculation in the GUI part of SALOME.

Model

Geometry An example for a composite detector model can be seen in Figure 3.12. It consists of the thermometer carrier (blue), the glue (red) and the target crystal (green). Only half of the thermometer carrier is displayed in order to show the position of the glue between the two crystals.

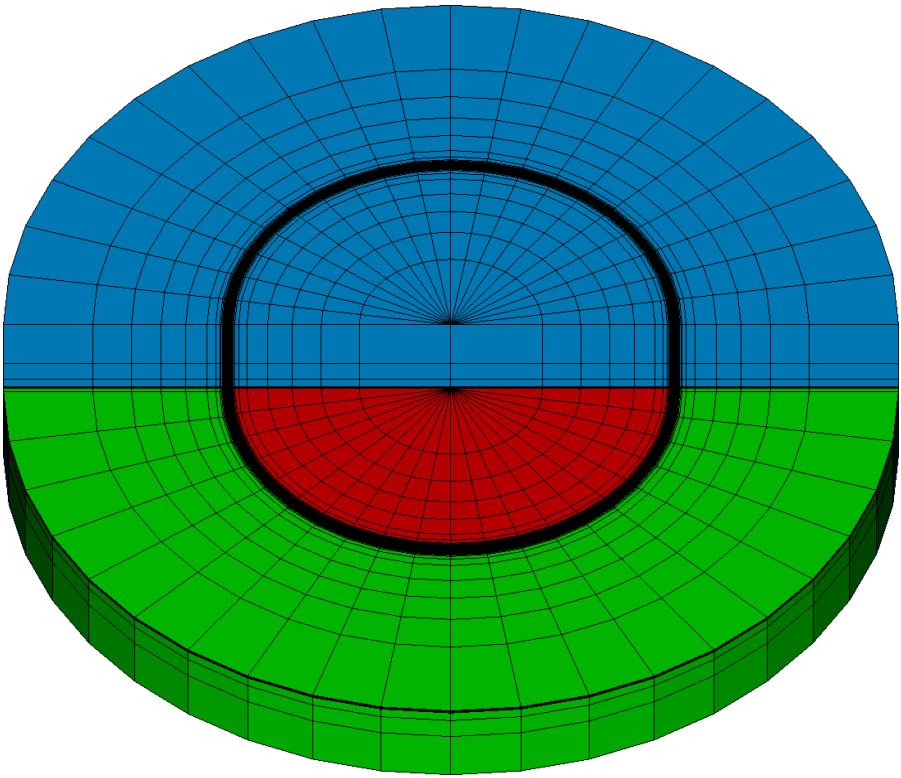

Figure 3.12.: The meshed geometrical model of a composite detector. Half of the thermometer carrier (blue) is cut out to reveal the glue (red) and the target crystal (green). The black lines represent the margins of the mesh elements.

Since the stress in the crystals drops off on relatively short distances, it is not necessary to model an entire $40 \times 40\,\mathrm{mm}^3$-cylinder for the target crystal and a corresponding $20 \times 10 \times 1\,\mathrm{mm}^3$ cuboid for the thermometer carrier. By reducing those parts to cylinders of $10 \times 1\,\mathrm{mm}^3$, one does not lose relevant information. On the other hand, limiting the geometry reduces the complexity of the problem, and thus drastically shortens the calculation time. The glue spot in the shown model has a diameter of 5 mm and a thickness of 40 µm. A model with these dimensions resembles the actual glue spots of the Run 32 composite detectors.

Meshing The black lines in Figure 3.12 indicate the boundaries of the individual mesh elements. As one can see, the size of the mesh elements is not constant over the whole geometry. Instead, the crystal meshes are refined towards the glue interfaces. The smallest mesh elements are located is the outer rim of the glue spot and its neighboring regions in the crystals. Finer meshes increase the precision of the calculation in regions of interest.

Although it is possible to manually generate a mesh by specifying the nodes and the line face and volume elements, it is much more convenient having the mesh generated automatically, especially in the case of more complex objects.

The automatic mesh generator can make use of various algorithms and corresponding hypotheses [Sal]: on the one hand, the meshing *algorithm* determines e.g. whether to split the faces of an object into triangular or quadrangular elements. The meshing *hypotheses* on the other hand can e.g. define the size distribution of the mesh elements. In combination, they provide a way to generate regions with coarser and finer meshes, depending on how important the regions are in the model.

The mesh in Figure 3.12 is a composition of three individual meshes corresponding to the parts of the composite detector. Since all three of them are cylinders, the instructions for the mesh generator had the following general structure for each of them:

- Generate two-dimensional sub-meshes for the cylinder faces first.
  - Split the circle into “pie pieces” of equal size.
  - Divide the pieces along the radial direction using concentric circles.
- Produce volume elements by extruding the polygons of the faces along the cylinder axis

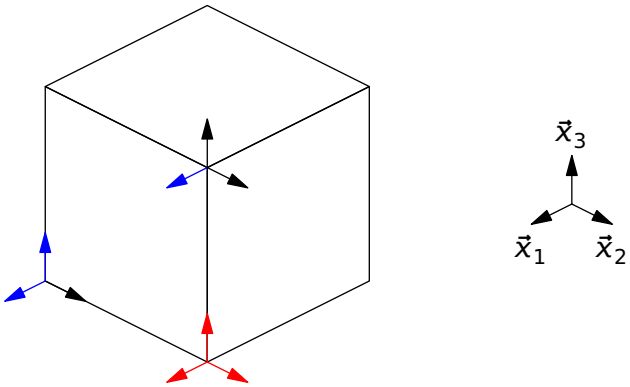

Figure 3.13.: Fixating a solid in three points is sufficient for keeping it from moving: Constraining the movements marked by the red arrows to zero stops any translation. When one additionally prevents motion in the directions marked by the blue arrows, there is no possibility for rotation any more.

The hypotheses used for the meshes in this work are chosen such that the circular faces are divided into 40 segments. The radial mesh size distribution for both the glue and the crystals decreases from the center towards the glue to a value of 5 µm as well. In case of the crystals, the mesh size then increases again from the interface to the outer rim of the cylinder. Axially, the crystals are divided into slices whose thickness decreases down to 5 µm near in the interface region. All of the glue slices have a thickness of 5 µm as well. With different smaller and bigger mesh sizes, the calculation gave consistent results. The finally selected mesh size is a balance between memory requirements and calculation time on the one hand and a detailed display on the other hand.

Apart from the shape, it is possible to select whether the mesh elements are *linear* or *quadratic*. This choice reflects the order of the polynomial which models the interaction between the boundary nodes of the mesh. A quadratic mesh allows more precise calculations at the cost of computing time. In the case of this work, the results only changed by 2 % while the calculation time increased by a factor of 10. Therefore, all the following calculations rely on linear meshes.

Boundary conditions In order to complete the formulation of the problem, one needs to specify boundary and connection conditions:

Isostatic support: If there is no specification on the movement of the entire object, the solver crashes, as the model concerns only the internal degrees of freedom. There is no information on the translation and rotation of the detector, meaning the model is under-determined.

One can arbitrarily choose a set of boundary conditions. In the easiest case, the boundary conditions simply prevent any movement of the simulated object. Figure 3.13 illustrates a way to do this, called isostatic support. This support works by restricting movements of three nodes in the geometry. Setting movements along the blue arrows to zero will keep the object from rotating. Restraining the movement along the red arrows will stop any translation.

Connection: If not explicitly stated otherwise, each sub-mesh representing a physical part of the detector is isolated. Therefore, one has to prompt the pre-processor to link the nodes on the faces of the glue spot to their adjacent neighbors on the crystal.

These conditions state the geometrical relations of the node elements. Two macroscopic properties of the system remain:

Crystal alignment $CaWO_4$ is an anisotropic material. This means that Young's modulus, the shear modulus, and Poisson's ratio have different values along the a- and c-axis. One has to state the orientation of the crystal axes along the meshed geometries. In case of the first simulation, the c-axes of both crystals are aligned along the cylinder axes. Since the glue is amorphous, its alignment is not relevant.

Temperature The initial temperature of the material is set to 300 K. The simulation calculates the state of the detector after a cool-down to 10 mK.

3.5.3. Results

Default Configuration

The simulation shown in Figure 3.14 will serve as the reference for all further discussions in this chapter. It relies on the assumptions presented in Section 3.5.2. These assumptions describe a composite detector with properties matching to those composite detectors which were part of the Run 32 setup. The color code of the picture represents the highest primary stress σ_{III} in the volume elements inside the detector. The picture itself is a cut view along the $y-z$-plane in order to inspect the inside of both the detector

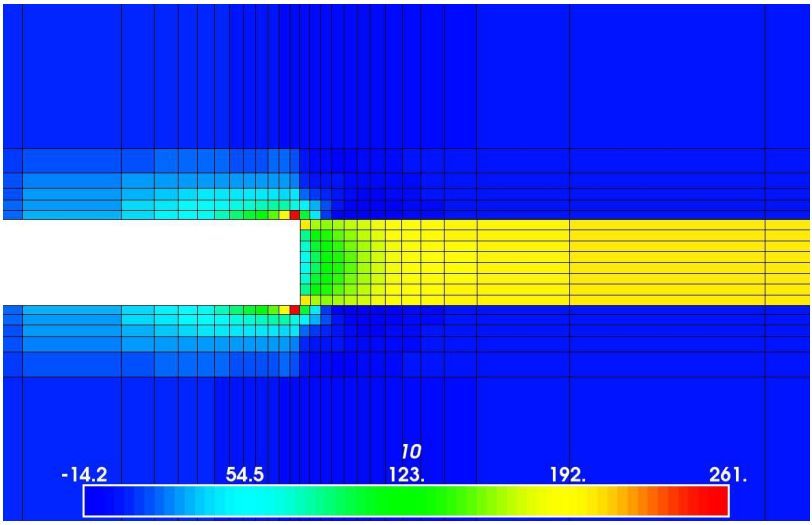

Figure 3.14.: The highest primary stress σ_{III} in the environment of the glue. The picture is a cut along the $y-z$-plane. Values are given in units of 100 MPa.

and the glue layer. If the sign of the primary stress is positive, the corresponding element suffers an expansion. If the stress is negative, the element is compressed.

The bulk material of both crystals suffers from a compression stress of $\sigma_{III} \approx 14\,\text{MPa}$ due to the cooling down. Most regions of the glue undergo an expansion stress of $\sigma_{III} \approx 200\,\text{MPa}$. The mismatching thermal expansion coefficients in combination with the different elasticities of the material are the reason why the crystal contracts while the glue suffers from an expansion stress although being cooled down.

The most interesting phenomenon happens at the crystal surfaces, near the outer rim of the glue. In contrast to the bulk material, this crystal region undergoes an expansion stress similar to the glue. With a value of $\sigma_{III} \approx 260\,\text{MPa}$ indicated by the red color of the element, this is the most intense stress in the entire model. In this region, the crystal will most probably crack, if the stress finally becomes too high for the crystal to bear.

The mesh elements in this interface region have an edge length of 5 µm. Thus, one can read from the plot that the stress drops down to $1/e$ of its original value in a distance of $\approx 30\,\mu\text{m}$ along the planes. The stress attenuation length in the axial direction is less than 10 µm.

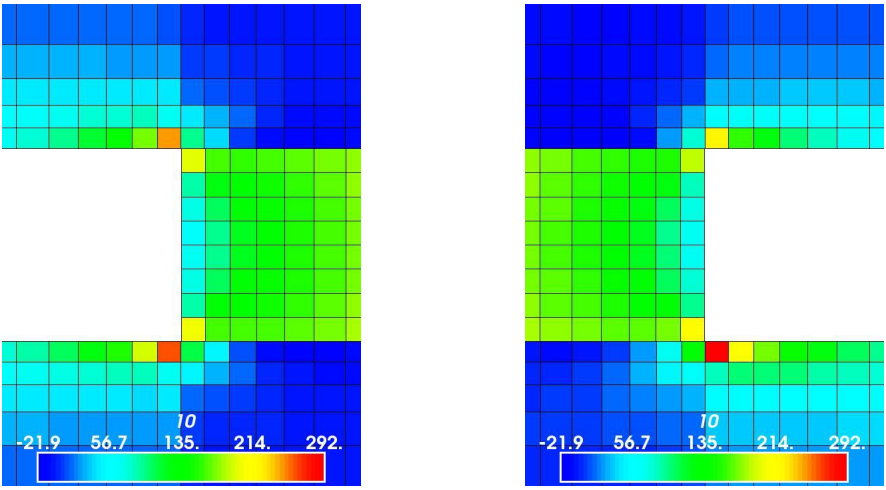

(a) View along the $(y-z)$-plane

(b) View along the $(x-z)$-plane

Figure 3.15.: The primary stress σ_{III} in a composite detector with the c-axes not aligned. In plot (a), the two a-axes coincide. Plot (b) looks at the region where the c-axis of the thermometer carrier meets the a-axis of the target crystal.

Planning to reduce the stress with the help of a nose structure as suggested in Figure 3.8, one would have to produce a glue spot which would cover the whole surface of the nose with a precision of $\mathcal{O} \approx (10\,\mu\text{m})$. As mentioned in Section 3.2.2, capillary effects between the crystal surfaces make it impossible to force the glue into assuming a certain geometry. Therefore, it is not realistic to make use of such a nose structure.

Alignment of the Crystals

One of the main concerns while assembling the composite detectors is the alignment of the crystals. $CaWO_4$ has different thermal expansion coefficients along its a- and c-axes. If the axes of the two crystals do not match, there might be stress caused by the crystals expanding differently along the same spatial direction, in addition to the stress created by the tension between the glue and the crystals.

In order to get an impression about the influence of the alignment of crystals with anisotropic characteristics on the stress in the detector, one can

	Thickness (µm)				
	20	40	60	80	100
Crystal Stress [MPa]	170	260	326	378	526
Glue Stress[MPa]	200	200	200	200	200

Table 3.2.: Influence of the thickness of the glue layer on primary stresses σ_{III} in the crystal region next to and inside the bulk material of the glue.

vary the alignment of the material properties in the simulation. If the two crystals are aligned in parallel, the primary stress value is $\sigma_{III} \approx 260\,\text{MPa}$ all along the glue interface. The same is true when rotating e.g. the thermometer carrier along the z-axis which is in parallel to the c-axes of the crystals.

The situation changes when rotating the alignment along one of the other two axes, x or y. In one of the most extreme cases, the c-axis of the thermometer carrier is in parallel with an a-axis of the target crystal. The result of this configuration is presented in Figure 3.15 which shows two sectional views along different planes of the detector geometry.

Figure 3.15(a) is a cut along the $y-z$-plane, where the a-axes of the crystals are in parallel. While in the target crystal the primary stress stays at $\sigma_{III} \approx 260\,\text{MPa}$, its value in the thermometer carrier changes by 5 % to $\sigma_{III} \approx 247\,\text{MPa}$.

In Figure 3.15(b), a cut along the $x-z$-plane, the a-axis of the target overlaps with the c-axis of the thermometer carrier. In this direction, the changes are more grave: The stress in the thermometer carrier drops to $\sigma_{III} \approx 220\,\text{MPa}$ which is a decrease of $\approx 15\,\%$. In the target, the stress increases to $\sigma_{III} \approx 290\,\text{MPa}$ which means $\approx 20\,\%$ more stress than in the case of a detector with aligned crystals. Percental changes of the same size can be observed with different mesh sizes.

However, the stress reduction occurs only along one spatial direction while the other one stays unchanged. In addition, it is not clear whether cracks in the carrier would eventually provoke additional cracks in the glue. Therefore, it is reasonable to have the crystals in a composite detector aligned.

Dimensions of the Glue Layer

Thickness Table 3.2 contains σ_{III} stress values for circular glue spots of 5 mm diameter. The thickness of the glue layer varies from 20 µm to 100 µm

	Diameter (mm)			
	0.1	2.5	5	9.9
Crystal Stress [MPa]	214	270	260	200
Glue Stress [MPa]	170	200	200	200

Table 3.3.: Influence of the diameter of the glue layer on primary stresses σ_{III} in the crystal region next to and within the bulk material of the glue.

in steps of 20 µm. One can see that the primary stress in the bulk material of the glue does not depend on the thickness of the glue layer.

On the other hand, the glue thickness has an influence on the primary stress in the crystal. The stress increases with thicker glue layers. Therefore, it is worthwhile to produce detectors with slim glue layers.

Diameter The stress σ_{III} depending on the diameter of the glue spot in Table 3.3 indicates that the diameter of the glue spot has no simple influence on the level of stress in the crystal. Both, extremely small and extremely large glue spots reduce the stress. In case of the large glue spots, the reason might be that outside the glue spot, there is simply not enough crystal material for causing large stresses.

In Figure 3.16, one can see that for a diameter of 100 µm, even the stress in the glue decreases. Therefore, detectors with very small glue spots might be an idea to reduce the stress. However, a small glue spot is less good for transmitting phonons. This could be compensated by making multiple spots. Nonetheless, as the glue is very fluid, these small spots would most probably unite due to the capillary forces between the two crystals.

3.6. Summary

Starting with Run 31, the CRESST setup included composite detectors. In contrast to a conventional detector module, a composite detector module has a modified phonon detector. Its sensor film does not sit directly on the cylindrical target crystal but instead on a small crystal called thermometer carrier. The thermometer carrier crystal is connected to the target crystal by a layer of epoxy resin glue.

The CRESST experiment could benefit of composite detectors in several ways. Firstly, composite detectors keep the bulk of the scintillator crystal from being exposed to high temperatures during the production process.

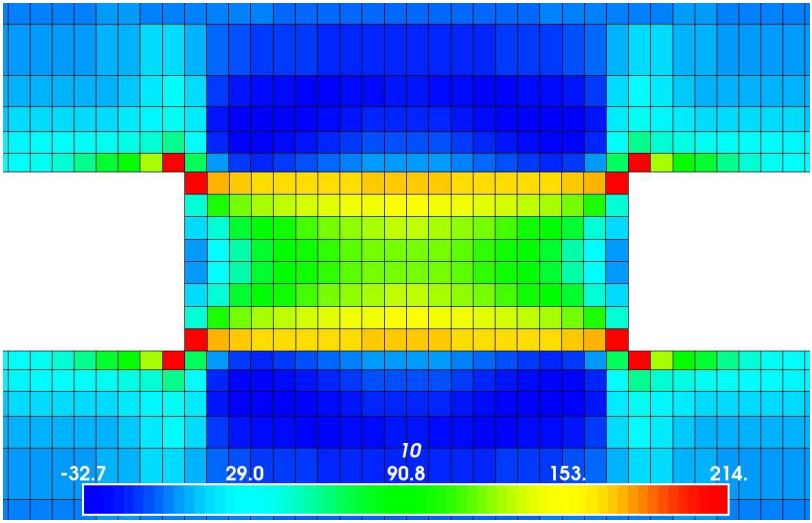

Figure 3.16.: Stress distribution in a glue spot of 100 µm diameter and 40 µm thickness. In this case, the stresses are lower than in a normal-sized glue spot. Due to the behavior of the glue, such a geometry is hardly possible.

Apart from increasing the production of scintillation light in certain $CaWO_4$ crystals, this makes it possible to use alternative scintillator materials in the first place. Secondly, composite detectors could simplify the detector production such that it might be possible to produce multiple thermometer carriers at once.

The glue layer between the target and the thermometer carrier means that phonons from particle interactions in the target have to pass through the glue before being detected. Data gathered in both Run 31 and Run 32 show that the pulses of composite detectors tend to be slightly slower than pulses of conventional detectors. Nonetheless, this does not significantly affect the energy resolution of the phonon detectors.

Each of the two components of a composite detector can experience an energy deposition. It is possible to determine in which of the components the particle interactions took place using the pulse shape of the signals. This is due to the fact that the components have different volumes and that the pulse shape depends on the absorptive volume.

When the $CaWO_4$ crystal and the glue are cooled down, they contract with different rates. Since both materials are connected, this results in thermo-mechanical stress. This stress might relax either in the form of micro-cracks which could fake particle interactions or by destroying the composite detector. Since this thermo-mechanical stress depends on the geometry of the detector, it is possible that certain geometries create more or less stress.

Measuring the thermo-mechanical stress actually occurring in the detector modules was not possible with the given resources. Instead, this work features simulations using the finite element method. These simulations give qualitative information on which geometrical parameters are favorable for designing a detector.

The simulations showed, that the highest stresses occurred at the interface region between the crystals and the glue, next to the rim of the glue spot. It emerged that it is especially important to produce thin glue layers for reducing the stress in this region. The diameter of the glue spot also plays a role in terms of the stresses. However, its influence is not as large as that of the thickness. The stress is also sensitive to the alignment of the crystals. With the c-axes of both crystals aligned in parallel, the stress along the rim region is constant all over the structure. If these axes are orthogonal to each other, there are regions with stresses that are higher and lower.

In summary, composite detectors have proven to work reliably in both Run 31 and Run 32. Their signal quality is good and they bear the potential for further optimizations of the CRESST experiment. Using FEM simulations, one has a mean of systematically investigating further improvements.

4. Determination of the Performance of the Light Channel

The measurement of the scintillation light is crucial for the discrimination of the different recoil bands. Thus, there is a strong motivation for optimizing the detector production towards high light outputs. In order to evaluate the individual scintillator crystals, it is necessary to know how much scintillation light they produce for a given deposited energy. Since the discrimination depends on the amount of detected light, an improvement is not solely possible by increasing the light production, referred to as the *scintillation efficiency*, but also by improving the light detection capability of the whole module. In this work, this concept is called the light *transport efficiency*.

The model which is the base of this chapter is presented in Section 4.2. The considerations in section 4.3 show the importance of the light channel for the event discrimination capabilities.

The subsequent sections of this chapter present three different methods with which the light channel can be examined. One of these methods is the default currently used for evaluating the crystals in CRESST. This standard method for the light output measurement is described in Section 4.4.

The other two are newly developed methods which can avoid some of the weak points of their predecessor. Both new methods work under cryogenic conditions, and require data of α- and γ-lines from e.g. a CRESST calibration run.

These evaluation methods need relatively high-energetic light signals. The standard event fit which is the base for the Dark Matter analysis is optimized for weaker signals and there are indications that it cannot cope with the high pulse amplitudes used for the light channel evaluation. Thus, modified fits and calibrations are necessary. Section 4.5 contains a description of these modifications.

The first alternative method compares the light signal of the scintillator crystal to a standard candle in the module. This comparison offers the possibility to compare the light productions of different crystals to each other.

The signal of the standard candle itself is a measure of the light transport efficiency inside the module.

With the second alternative, the energy balance method, one can directly obtain percental values for both, the fraction of the deposited energy which the crystal turns into scintillation light and the fraction of this light that reaches the light detector.

The new methods are described in Section 4.6 and 4.7, respectively. A comparison of the results obtained from the different methods can be found in Section 4.8. The impacts of these findings and suggestions for further experiments conclude the chapter.

4.1. Scintillation Light in the Detector Module

In the further parts of this work, the life cycle of the scintillation light in a detector module is considered to consist of three steps:

Production: The impinging particles excite the crystal. Scintillation centers, in case of $CaWO_4$ the $[WO_4]^{2-}$ complexes, convert a fraction of the initially deposited energy to scintillation light [Bir64]. Aside from the energy, the amount of scintillation light depends on the nature of the impinging particle as well as on the transformation capability of the crystal. The quenching factor takes into account the former component, whereas the latter, under the name *scintillation efficiency*, is one of the two main subjects of this chapter.

Transport: While the scintillation light propagates through the detector module, it passes through the crystal and reflects on the scintillating foil which forms the innermost layer of the housing. The so-called *transport efficiency* takes into account the opacity of the crystal and the absorptivity of the housing. Both these properties lead to a diminution of the initially created scintillation light.

Absorption: The final step is the absorption by the light detector. The light detector is assumed to fit ideally to the light which it absorbs. This means that the detector converts all the energy it absorbs into a signal without any loss. However, it is possible that a fraction of the light is not absorbed but reflected, or it simply passes through the wafer of the light detector. As there is the reflecting foil behind the light detector as well, this fraction of light is not lost.

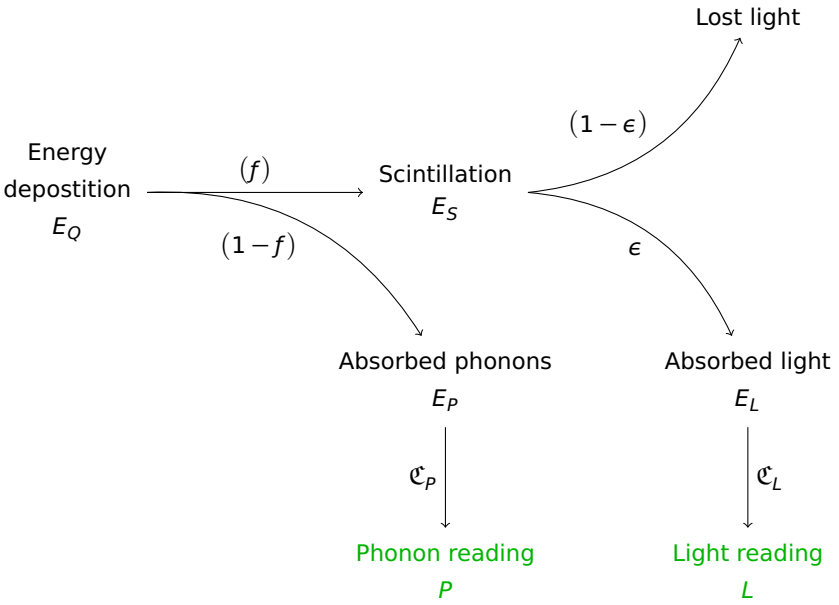

Figure 4.1.: The distribution of energy in the scintillator crystal. An amount E_Q of energy is deposited by a particle. A fraction f of E_Q is converted to scintillation light E_S. The light detector can detect a fraction ϵ of this light.

4.2. Theoretical model of the Energy Distribution in the Detectors

4.2.1. Conversion of Deposited Energy to Phonon and Light Signal

The model, similar to the one described [Arn+10], describes the energy flow in the detector module. It is illustrated in Figure 4.1 and uses the following assumptions:

At the beginning, a particle interaction deposits an energy E_Q in the detector. This energy splits up[1] into one part carried by phonons E_P and another part carried by scintillation light E_S.

[1]This model assumes a complete conversion of the energy into either phonons or light. Possible losses at the particle deposition level are discussed in Section 4.2.2

The amount of scintillation light corresponds to

$$E_S = f E_Q \tag{4.1}$$

and the amount of phononic energy to

$$E_P = (1 - f)\, E_Q \tag{4.2}$$

The fraction f describes the distribution of the deposited energy between phonons and scintillation. It depends on the nature of the impinging particle. This particle dependence is taken into account by the quenching factor QF as it was introduced in equation (2.1). The quenching factor uses the scintillation of γ-particles as a reference so $QF = 1$ for these events, at least for a deposited energy of 122 keV.

The fact that the scintillation does not solely depend on the type of impinging particle, but also on the scintillator material itself makes it necessary to introduce another term. This factor X describes the fraction of energy which turns to scintillation light when a γ-photon excites the detector. For other types of particles, the amount of light decreases according to the respective quenching factors.

$$f = \frac{X}{QF} \tag{4.3}$$

While the phonons propagate in the crystal until being absorbed by the sensor film, the energy in the light channel splits up further: A fraction of the light is lost due to absorptive surfaces in the detector module or due to light trapping in the crystal. The light detector absorbs the remaining fraction ϵ of the scintillation light.

$$E_L = \epsilon E_S \tag{4.4}$$

It is possible that the crystal re-absorbs a part of the light and converts it back into phonons. The probability of this effect increases if the light is reflected multiple times within the module. If this happens, the re-absorbed energy is seen by the phonon detector.

4.2.2. Calibration

The energies E_L and E_P which enter the respective sensors of the phonon and light detectors are absorbed by the electron systems. This increases the resistance of the sensors. Since the detectors are provided with a constant bias current, this causes a variation of the current splitting in the circuit shown in Figure 2.10. The DAQ system registers the temporal development

of these variations in the form of voltages which the SQUID controller produces.

The following analysis treats the pulses formed by the changing voltages; the assignment of pulse heights to energies is done in the calibration. The whole step of conversion of deposited energy to pulse height and reinterpretation as energies P and L can be condensed into a calibration factor $\mathfrak{C}$ for both the phonon and the light detector.

$$P = E_P \mathfrak{C}_P \tag{4.5}$$
$$L = E_L \mathfrak{C}_L \tag{4.6}$$

In general, these calibration factors are determined in the following way:

1. Expose the detector to particles of a known energy $E_{Q,\text{cal}}$
2. Assign the detector signals L, P to the deposited energy $E_{Q,\text{cal}}$

For the calibration factors, this means:

$$P = E_P \mathfrak{C}_P \stackrel{!}{=} E_{Q,\text{cal}} \tag{4.7}$$
$$L = E_L \mathfrak{C}_L \stackrel{!}{=} E_{Q,\text{cal}} \tag{4.8}$$

In case of the assumptions of Section 4.2.1, the quantities E_P and E_L contain the deposited energy, the effects of the quenching factor, and the scintillation and transport efficiencies:

$$P = E_Q \mathfrak{C}_P \left(1 - \frac{X}{QF}\right) \tag{4.9}$$
$$L = E_Q \mathfrak{C}_L \frac{X}{QF} \epsilon \tag{4.10}$$

The conditions (4.7) – (4.10) are fulfilled if the calibration factors compensate for all the processes concerning the scintillation light:

$$\mathfrak{C}_P = \frac{1}{1 - \frac{X}{QF_{\text{cal}}}} \tag{4.11}$$
$$\mathfrak{C}_L = \frac{1}{\frac{X\epsilon}{QF_{\text{cal}}}} \tag{4.12}$$

Note that with the quenching factor included, the calibration factors are sensitive to the type of particle used for the calibration.

Phonon Loss

In the model above, one neglects the energy which does turn neither into phonons nor into scintillation light. A fraction of the deposited energy could, for example, evade the read-out channels via excitations with long time constants or via phonons which escape through the clamps. In a simple assumption, the fraction of lost energy is constant for all types of particles. This means that the quenching factor is the only particle-dependent term and that, once the phonons exist, their origin is not important any more. Under that assumption, neglecting these loss channels is justified, as the calibration of the phonon detector will, by definition, include the effects:

Assuming e.g. a fraction D disappearing from the overall energy means that only the remaining part $(1-D)$ can split up between phonons and light. The lost part will never have an influence on the readings of the channels. Correspondingly, replacing E_Q by $(1-D)\cdot E_Q$ in all the equations will not provide additional information. It affects the phonon and the light signal in the same way and at the end, both calibration factors contain a $(1-D)$ term. When one then calibrates the detector with a certain particle, one has to respect the energy loss in the energy deposition. Like this, the $(1-D)$ term cancels out:

$$P = E_Q(1-D)\mathfrak{C}_P\left(1-\frac{X}{QF}\right) \stackrel{!}{=} (1-D)E_{Q,\mathrm{cal}} \tag{4.13}$$

$$L = E_Q(1-D)\mathfrak{C}_L\frac{X}{QF}\epsilon \stackrel{!}{=} (1-D)E_{Q,\mathrm{cal}} \tag{4.14}$$

Light Detector Calibration and Light Transport Efficiency

Usually, the phonon detector is calibrated using the 122 keV γ-line of a ^{57}Co source. The light detector is calibrated with the scintillation light of these events. The calibration factors are chosen such that the energy readings of both detectors correspond to the injected energy for $Q_\gamma = 122\,\mathrm{keV}$:

$$P = E_Q\mathfrak{C}_P\left(1-\frac{X}{QF}\right) \stackrel{!}{=} 122\,\mathrm{keV} \tag{4.15}$$

$$L = E_Q\mathfrak{C}_L\frac{X}{QF}\epsilon \stackrel{!}{=} 122\,\mathrm{keV} \tag{4.16}$$

This means that the calibration factors have to compensate for the scintillation effects of γ-particles. Since the quenching factor of γ-particles is $QF_\gamma = 1$

by definition, this implies:

$$\mathfrak{C}_P = \frac{1}{(1-X)} \tag{4.17}$$

$$\mathfrak{C}_L = \frac{1}{X\epsilon}. \tag{4.18}$$

Such calibrations are useful in order to produce a light yield plot for the Dark Matter analysis, as it is described in Section 2.1.3. Yet, they do not contain information about the energy distribution between phonons and light any more. The values for X and ϵ are hidden in the calibration factors $\mathfrak{C}_P$ and $\mathfrak{C}_L$ so that only the quenching factor QF plays a role in the measurement.

Thus, for an evaluation of the light channel, the choice of a meaningful light detector calibration is especially important. As the transport efficiency plays a role solely in the light channel, a light detector calibration which compensates for the transport efficiency will effectively remove its information from the calibrated data.

In theory, it is possible to extract the influence of the transport efficiency from the resolution of the light channel. However, this would require a precise knowledge not only about how the transport efficiency contributes to the resolution, but also about all the other contributions. This makes a definite reconstruction of the contribution of the transport efficiency hardly possible. In addition, with the method presented, one directly obtains the relation between transport and scintillation efficiency.

It is therefore essential to choose a light detector calibration which does not depend on the transport efficiency.

With a so-called absolute calibration, one can keep the information about the transport efficiency in the data. Then, the effects of e.g. crystals of different opacities and non-reflecting surfaces are observable. In the context of this work, absolute calibration means that a light detector reading of $L = 1\,\mathrm{keV}$ is the result of the deposition of $E_{L,\mathrm{cal}} = 1\,\mathrm{keV}$ directly into the light absorber:

$$L = E_{L,\mathrm{cal}} \tag{4.19}$$

Then, according to equation (4.6), the calibration factor of the light detector is

$$\mathfrak{C}_L = 1. \tag{4.20}$$

Not containing an ϵ, this calibration will not compensate for losses during light transport.

Such an absolute calibration can be done with a low-energetic X-ray emitter. It is valid under the assumption that the detector reacts the same when

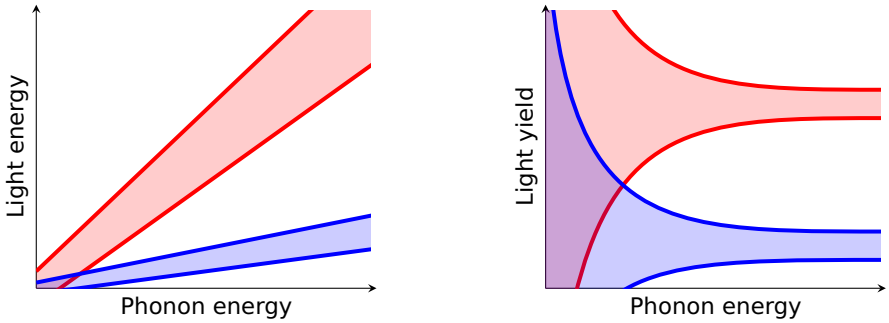

(a) Bands in light energy display

(b) Bands in light yield display

Figure 4.2.: The combination of light and phonon signal provides a mean to discriminate different particle bands. Instead of the display energy vs. light signal in Figure (a), the usual form is energy vs. light yield (Figure (b)). The slope of the bands in the energy vs. light plot corresponds to the ordinate position of the bands in the energy vs. light yield plot.

it absorbs thousands of scintillation photons with energies in the eV range and individual X-rays in the keV range.

4.3. Influence of the Scintillation Efficiency on the Width of the Bands

As it was explained in Section 2.1.3, the scintillation light provides a criterion of discrimination for different particles. For a Dark Matter analysis, this discrimination is not done directly via the energy reading of the light channel. Instead, a value LY called the light yield is calculated and used for the discrimination. The light yield is defined as the ratio between the energies measured in the light and the phonon channel.

$$LY = \frac{L}{P} \tag{4.21}$$

As mentioned in Section 4.2.2, the light detector is usually calibrated such, that the energy reading of a γ-scintillation event is equivalent in both the phonon and the light channel. Therefore, the light yield is $LY = 1$ for 122 keV γ-events of the ^{57}Co-source.

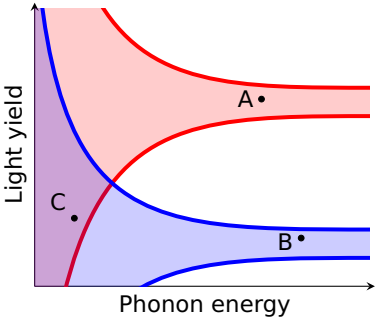

(a) Assignment of point C ambiguous

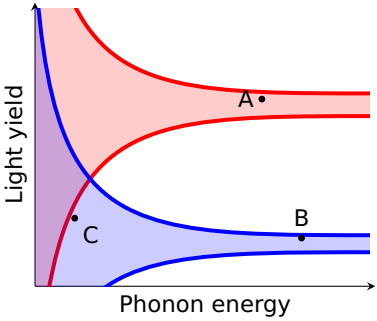

(b) Assignment more clear due to more narrow bands

Figure 4.3.: Influence of the band width on the discrimination efficiency. In plot (a) the assignment to a certain band is clear for point A and B but not for point C. The smaller bands in plot (b) increase the confidence of assigning point C to the blue band.

Figure 4.2(a) shows a plot of the light signal versus the phonon signal. Commonly, the phonon detector reading is interpreted in good approximation as the energy of the particle interaction. Particles of different nature are aligned in bands of different slope.

Plotting the light yield versus the energy results in Figure 4.2(b). Here, the bands of different slopes have turned into horizontal bands of varying distance from the horizontal axis. The distance and the slope in the respective plots are equal to the reciprocal of the quenching factor of a particle. As the phonon and light detectors have a finite resolution, the bands have a non-zero width.

The resolution of the phonon detectors is better compared to the resolution of the light detectors. Therefore, the width of the bands is mostly determined by the properties of the light detector. In the range of low energies, the width of the bands increases, as the signal to noise ratio of the detectors gets worse.

In order to keep the following discussion more generic, these plots do not refer to specific particles. Instead, the case of two types of hypothetical events, “red” and “blue”, with different quenching factors will be discussed. For reasons of simplicity, the bands in the example have finite boundaries, like in the case of a contour containing a fixed percentage of all the events in a band.

The width of the bands is crucial for the discrimination between different types of particles. Figure 4.3 visualizes the effect:

- In the region of high energies in Figure 4.3(a), the red and the blue band are clearly separate. Without doubt, point A can be assigned to the red band and point B belongs to the blue band. The position of point C is in the region where the red and the blue band overlap. It is impossible to claim that point C was caused by an event of type "red" or by an event of type "blue".
- In Figure 4.3(b), the points are at the same positions, but the width of the bands has changed. With the bands more narrow, the overlap is smaller as well. Now, the confidence for assigning point C to the blue event band is much higher.

Since the WIMP-signal is expected at low energies, narrow bands are favorable since they can drastically increase the possibility to identify a signal. One way to make the bands more narrow is to improve the light output of the crystals. While being intuitively clear, this circumstance can be formally proven in the following way. Assume that the light channel has a resolution of σ_{E_L}. Then, the calibrated reading looks like

$$L = \mathfrak{C}_L E_L. \tag{4.22}$$

It has a resolution of

$$\Delta_L = \mathfrak{C}_L \sigma_{E_L}. \tag{4.23}$$

The detected light signal of equation (4.4), with the equations (4.1) and (4.3), and a calibration according to (4.18) becomes

$$L = \frac{E_Q}{QF} \tag{4.24}$$

and the resolution accordingly

$$\Delta_L = \frac{\sigma_{E_L}}{X\epsilon}. \tag{4.25}$$

The calibration compensates for detector module-specific behavior concerning the light production and transport. Thus, rising the amount of emitted or detected light will *not enhance the energy* reading L itself. Yet, the calibration introduces the scintillation and transport efficiencies as a denominator to the resolution term. This means that enhancing the light output of a detector module can *improve the resolution* level Δ_L and by this way, improve

the signal to noise ratio, at least if the term σ_{E_L} has components which rise less than linear with $X \cdot \epsilon$.

The phenomenological model which describes the resolution of the light channel in CRESST is of the form

$$\sigma_{E_L} = \sqrt{V_{E_L}} = \sqrt{V_0 + V_1 E_L + V_2 {E_L}^2} \tag{4.26}$$

To some extent, physical characteristics of the detector module can be attributed to the different summands. The baseline noise of the sensor for example does not depend on the energy of the signal. Thus it will contribute to the V_0-term. Statistical variations of the phonon counting depend linearly on the number of emitted phonons. Therefore, the $V_1 E_L$-term at least partially consists of these variations. If in a crystal the scintillation and transport efficiencies X and ϵ have a position dependence, such an effect will contribute to the $V_2 {E_L}^2$-term.

However, the resolution does not solely consist of these terms. For example the standard event fit, which is a central part of the data analysis, performs differently when confronted with pulses of different heights, below or above the truncation level. Thus, the fit introduces an energy-dependent contribution to the resolution. Another example is a position dependence in the sensitivity of the light detector.

In [Sch10] it has been shown that this model is a good description of the data, at least in a phenomenological way. Therefore, the model is sufficient in order to estimate the influence of the factors X and ϵ on the resolution. With the γ-calibration, the overall error of the light detector energy reading is:

$$\Delta_L = \frac{\sigma_{E_L}}{X\epsilon} = \sqrt{\frac{V_0}{X^2\epsilon^2} + \frac{V_1}{X\epsilon}\frac{E_Q}{QF} + V_2 \frac{{E_Q}^2}{QF^2}} \tag{4.27}$$

The calibration inserts $X \cdot \epsilon$ into the denominators of the first two terms below the square root. Thus, the overall sum diminishes with increasing $X \cdot \epsilon$. This shows that improvements in both, the scintillation and the collection efficiency enhance the resolution of the light detector and thus result in more narrow bands. Especially for low energies, where the width of the bands is a crucial factor for the discrimination of events, the increase of $X \cdot \epsilon$ has a beneficial effect. In the range of high energies, the dominant part is the V_2-term which is not affected by higher $X \cdot \epsilon$.

The calculations of Section 1.5.2 lead to the result that the expected WIMP recoil spectrum decays exponentially with the energy. Therefore, the experiment can benefit greatly from improvements of the scintillation and transport efficiency.

Name	Delivery	Anneal	Polish	Deposit	Roughen
Hanna	60	146			177
K14	140	151			
Maja	100	110			
Rita	82	126			131
Verena	88				109
VK29	67	109		87	101
VK31	31	127	113		125
VK32	68	126	116	103	122
VK33	70	119	111	92	117
VK34	98	124			143
Wibke	88				100
$ZnWO_4$-4	97	108			

Table 4.1.: Percentage of light output compared to *Boris* after different steps of the detector production. These values were obtained at room temperature using a photomultiplier.

4.4. Method 1: Room Temperature Measurement with Reference Crystal and Photomultiplier

The most straightforward approach to compare the amount of scintillation light that different crystals produce, is to compare the reaction of individual crystals to a reference crystal, when exposed to a standardized radiation source. After having purchased new crystals, one can use a photomultiplier in order to measure them individually and, by comparing them to the reference crystal, put them in relation to the other crystals. It is not necessary to gather all crystals for a comparison every time after a new crystal has been acquired. However, measuring the reference crystal again each time is mandatory, as varying ambient conditions have an influence on the properties of the photomultiplier used in the process.

The reference crystal commonly used in CRESST is the $CaWO_4$ crystal *Boris*. The light outputs of the individual crystals are normalized to the light output that *Boris* had in the same measurement session. If the crystal specimen is made of another material, one has to compensate for eventual differences in the scintillation emission spectra of $CaWO_4$ and the other material. This is the case e.g. for the $ZnWO_4$ crystals [Bav09].

Table 4.1 shows the light output values of several crystals across different steps of detector production. All crystals become more efficient after an annealing process in an oxygen atmosphere. However, this improvement is not necessarily permanent. For the conventional detectors, the light output after the thermometer deposition has decreased again.

The origin of both effects is of chemical nature: amounts of oxygen lower than the stoichiometric optimum result in a decrease of the the light output. Newly delivered crystals can have such an oxygen deficit. The oxygen annealing increases the amount of oxygen in the crystal and thus enhances the light output. Afterwards, the evaporation process also takes place at high temperatures but at low pressures. These conditions reduce the oxygen content of the crystals and the light output becomes worse again.

When the crystals are being polished, the reflectivity of the surface increases. Due to the different refractive indices of the crystal and the medium outside, this means an increased chance of light being reflected inside the crystal infinitely. This phenomenon is called light trapping. A rough surface increases the probability that the light leaves the crystal and thus the light output after the roughening increases.

The photomultiplier tube (PMT) method of determining the light output of a crystal happens at ambient temperature in a table-top experiment. The measurement is therefore easy to perform. The disadvantage of this simple method comes from the fact that at least the scintillation of the crystals is temperature-dependent [KMW05]. There is no guarantee that all crystals behave in the same way when cooling them down to mK temperatures. Hence, the resulting light output values do not necessarily indicate whether or not the crystal is well-suited for the actual Dark Matter experiment.

Concerning the transport efficiency, the method also has a weak point: The PMT measurement applies to individual crystals and not complete detector modules. Thus, one can only determine the crystal-specific contribution to the light transport efficiency of a detector module. The contribution of the module housing which might become interesting for modified detector module designs is not measured with the *Boris*/PMT method.

4.5. Data Treatment for Measurements Under Cryogenic Conditions

4.5.1. Modification of Standard Event Fit Procedure

Apart from the *Boris*/PMT method, it is possible to measure the properties of the light channel in two further ways. They are going to be called *standard*

candle method and *energy balance method*. These methods are described in the sections 4.6 and 4.7. Both require data taken at Gran Sasso which have undergone a special fitting and calibration treatment.

Data for the two alternative measurements come from complete detector modules operated during Run 32. The methods require the measurement of γ-induced scintillation light where the excitation energy is known and, as explained in Section 4.5.3, preferably in the range between 500 and 1000 keV. This exceeds the range in which the detectors are commonly used for Dark Matter search by an order of magnitude.

In addition, both methods rely on an absolute calibration of the light detector. In such a case, the energy of the calibration source is deposited directly in the light detector wafer, without undergoing a conversion to scintillation light. The pulse shapes of these direct depositions in the light detector differ slightly from signals that have been induced by scintillation light. The fits which determine the pulse amplitudes can be influenced by changes in the pulse shape if these are large enough. It is necessary to avoid such a behavior.

The range issue and the different pulse shapes, can be solved by increasing the fit truncation amplitude above the recommended level described in Section 2.4.2. Using the example of the light detector *X*, Fig. 4.4 shows the impact of the increased truncation level on the data from the calibration source: Both plots compare standard event fits to the maximal pulse height attained in a record.

For plot 4.4(a) the truncation level was set to 0.4 V whereas for plot 4.4(b) the truncation level was elevated to 1.0 V. In both plots, scintillation light events form linear bands which extend from the origin of the plot across the entire canvas. In each plot, below these scintillation light bands, there is an additional separate population of events. This separate population is constituted by the signals from the ^{55}Fe-calibration source directly illuminating the light detector.

The amplitude values at which these populations reside vary with the truncation level of the fit. A higher truncation level shifts the population towards the γ-band. The higher truncation makes the fit less sensitive to the difference in pulse shapes. This does not simply affect the "offset" of the ^{55}Fe-sub-band but also its slope. Comparing the two plots, one can see that the band of calibration events adopts the slope of the scintillation events.

The fact that the slopes are equal in plot 4.4(b) is important for the calibration: It indicates that in this case, the amplitude values are correlated to the pulse height in the same way for scintillation events as for direct hits. As the calibration converts pulse amplitudes to energies, this means that the relation between amplitude and energy is the same for the calibration

Detector module	systematical error (%)	
	Phonon detector	Light detector
Verena/Burkhard	0.04	2.9
Verena/Q	0.04	0.085
Verena/combined	0.04	1.4
Maja/Hans	0.12	0.79
$ZnWO_4$/Ulrich	0.16	2.2
Wibke/X	0.08	0.30
Rita/Steven	0.40	3.2

Table 4.2.: Detector modules and relative systematical errors of their calibration. The values are given as percentages.

and the scintillation events. Thus, with this kind of standard event fit, an absolute calibration of the light detectors is possible.

4.5.2. Calibration of the Detector Modules

Only the energy balance method requires a calibration of the phonon detector. In principle, a calibration is not necessary at all for the standard candle method. It works, as long as it is possible to ensure that one always uses the same γ-line when comparing the different crystals. This is already possible with the uncalibrated fit amplitudes, although analysis with the anyway calibrated data is much more convenient. Both alternative methods require an absolute calibration of the light detector.

Phonon Detectors

In order to calibrate the phonon detectors, one needs a line which can be clearly assigned to a known deposition of energy. For a Dark Matter analysis, this is usually the absorption of 122 keV γ-photons from a ^{57}Co source. The energy balance method works by comparing the phonon and light detector readings for selected lines of γ-photons and α-decays. The α-lines with the lowest energies that can be observed with all detectors are those of ^{147}Sm and ^{180}W. They are at 2310.5 keV [GM70] and 2516 keV [Coz+04] respectively. These energies exceed the one of the 122 keV line by a factor of ≈ 20. In addition, they are beyond the range covered by the test pulses as well. These usually reach up to ≈ 2 MeV.

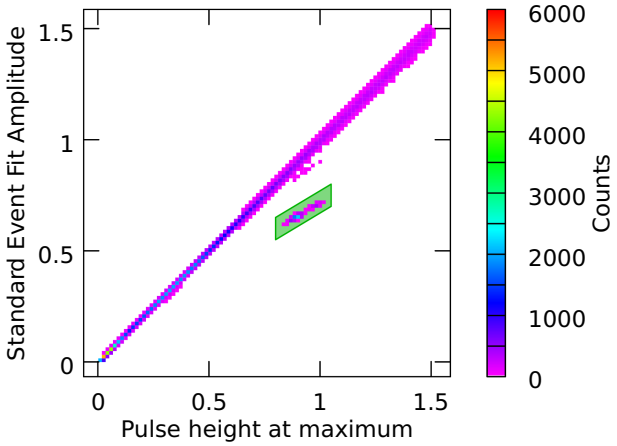

(a) Standard event fit, truncated at 0.4.

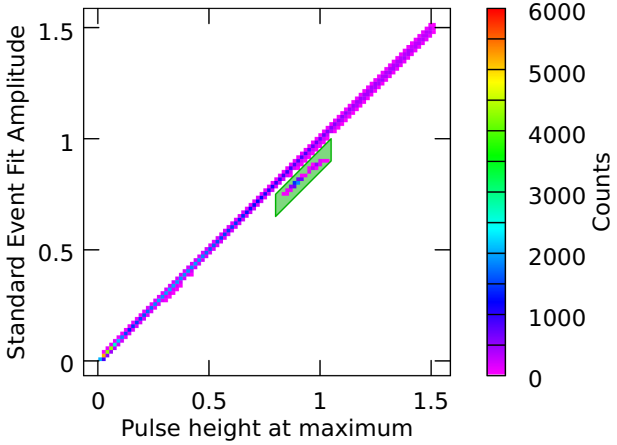

(b) Modified standard event fit, truncated at 1.0.

Figure 4.4.: The impact of a modified fit truncation level on the fit result of the ^{55}Fe calibration peak in the detector *X*. Note the population of ^{55}Fe-events marked in green, as it adopts the slope of the gamma band when raising the truncation level.

In order to avoid introducing errors by extrapolating the 122 keV γ-calibration too far, this work relies on a modified phonon detector calibration: The reference is not the 122 keV γ-line but one of the α-lines. As the ^{147}Sm-line has the higher count rate in all detectors, it is the more convenient choice, compared to ^{180}W.

Similar to the Dark Matter analysis, the response of the detector to the test pulses establishes the scale for applying the calibration over the whole energy range. But in contrast to the Dark Matter analysis, the calibration peak is beyond the test pulse scale. This means that the polynomial which interpolates the behavior of the detector for amplitude values in between the test pulses has no support nodes in the range of the calibration line.

Raising the order of the polynomial above 1 increases the risk of the polynomial diverging from the actual detector behavior in the range of interest. This can be observed directly when comparing the calibrated energy reading of the ^{180}W-peak to its literature value. The percental value of this deviation is the systematical contribution of the phonon detector error to the estimation of the errors in the calculation of the scintillation and transport efficiency values.

With regard to this calibration error, the interpolation polynomial for all phonon detectors was limited to an order of 1, excepting *Rita*, where a second-order polynomial yielded the smallest deviation. The percental errors assumed for the individual phonon detectors can be found in Table 4.2.

In theory, one can calculate the energy balance using a γ-calibration as well. The choice of the calibration source is arbitrary. Nonetheless, one has to take it into account when setting up the equations for comparing the α- and γ-lines.

Light Detectors

As indicated above, the reference for the light detector calibration comes from an ^{55}Fe source. These nuclei perform an electron capture, causing the emission of the K_α- and K_β-lines of the daughter nucleus ^{55}Mn. The energies of those X-ray lines are 5.895 keV[2] and 6.490 keV [CEF99].

Similar to the phonon detector, the lower of the two lines serves as the reference. A comparison between the reading of the upper line compared to its literature value yields an estimate of the relative systematical error. As in the case of the phonon detectors, the percental errors of the individual calibrations can be found in Table 4.2.[3]

[2] The CRESST detectors are unable to resolve the difference between the $K_{\alpha 1}$- and $K_{\alpha 2}$-lines of 5.888 keV and 5.899 keV[CEF99]; the value above is the weighted mean of these energies.

[3] These percental errors are assumed to be the same for all calibrated values. As the data lack

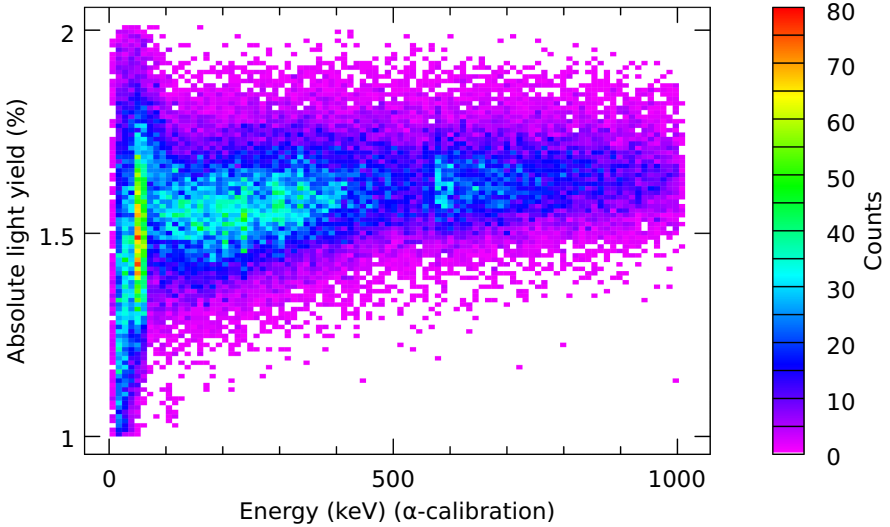

Figure 4.5.: Absolute light yield vs. energy for the detector pair *Verena/Q*. Note the strong non-linearity of the γ-band.

In the case of the light detectors, the reference line lies within the range of the test pulses. Therefore, one can select an interpolation polynomial of higher order, increasing the modeling accuracy of the detector behavior.

4.5.3. Selection of Data Points for γ-Induced Scintillation

For the analysis, one needs to identify at least one γ-line within the measured spectrum. In the environment of this emission line, the detector should preferably behave in a linear way.

The plot in Figure 4.5 shows the light yield (see equation (4.21)) against the phonon energy. The data come from the detector pair *Verena/Q*. In contrast to the simple assumption made in Section 2.1.3, the γ-band does not have a constant slope. The rise in the low energy range, known as scintillator non-proportionality, is known for various materials (see e.g. [Tau+97; Mos03]). The overview in Figure 4.6 shows that all the detector modules have regions of non-linear light yield.

Except for the $ZnWO_4$-module, the γ-band becomes flat for energies above 600 keV. There are features in this energy domain of the background run

a second line with an energy known independently from the calibration, it is not possible to refine this estimation by e.g. a linear approximation.

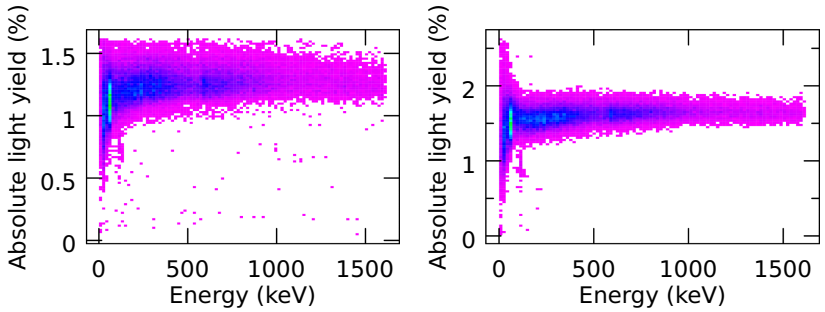

(a) *Verena/Burkhard* (b) *Verena/Q*

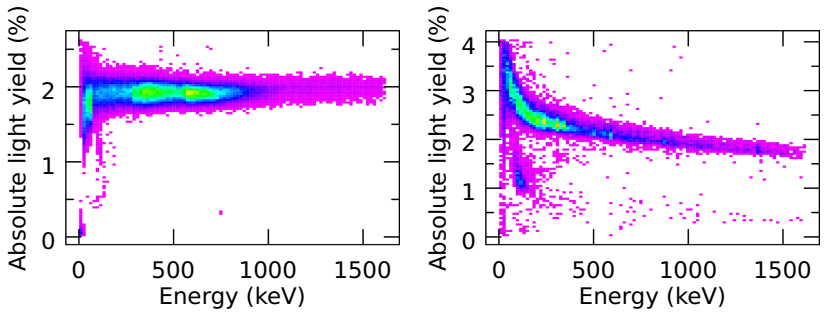

(c) *Maja/Hans* (d) *$ZnWO_4$-4/Ulrich*

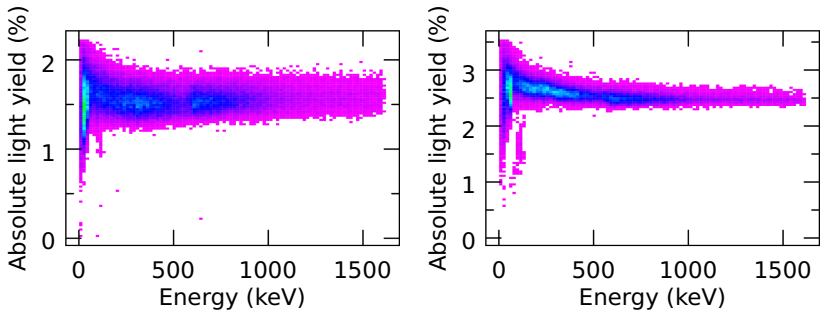

(e) *Wibke/X* (f) *Rita/Steven*

Figure 4.6.: Absolute light yield versus energy for all detector modules. Except for the $ZnWO_4$, all detector modules have a linear region above 600 keV.

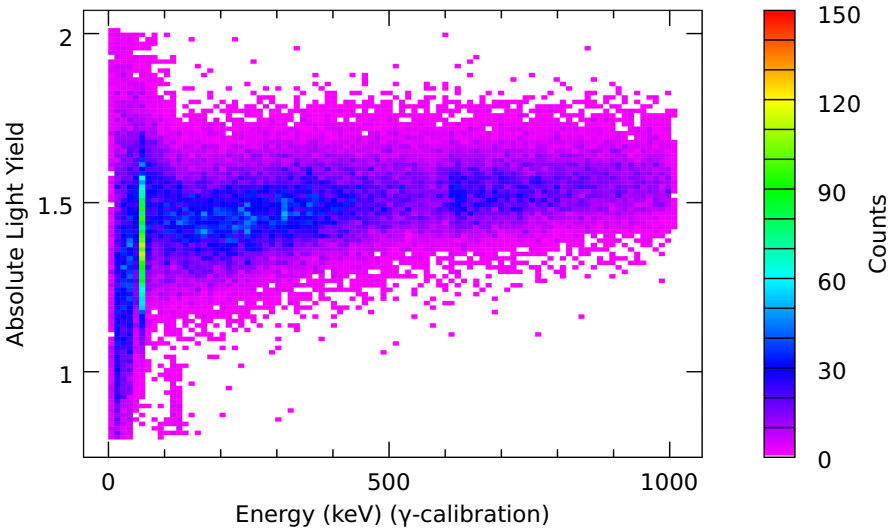

Figure 4.7.: Absolute light yield vs. energy for the detector pair *Verena/Q*. The non-linearity is present with γ-calibrated data as well.

data. However, none of these was an emission line that was suitable for the analysis:

- The γ-line of ^{40}K at 1460.8 keV, would be a good candidate due to its well-defined energy. This natural isotope of potassium is present in the human metabolism, and human sweat is probably the origin of this contamination of the detectors. However, the line is not strong enough in every detector in order to serve as a common reference.
- All detectors feature β-spectra starting at $\approx$ 600 keV. Even with an analysis regarding coincident α-decays it was not possible assign these β-emissions to certain decay chains in a doubtless way. Therefore, as the energy of these β-spectra is not absolutely certain, they cannot serve as a calibration reference.

In order to provide a clear reference peak for γ-induced scintillation, a calibration with a ^{232}Th source was done near the end of Run 32. A good overview of the spectrum of this isotope and its daughter nuclei can be found in [Rad11]. From the various γ-lines of this spectrum, the double peak of ^{228}Ac and ^{212}Bi at 726 and 727 keV lies within the linear region and is clearly identifiable by its distance to neighboring peaks. The γ-energy of 727 keV is therefore the reference line for the following analyses.

For low energies, the non-linearity of the γ-band light yield is already described in [Bir64]. One could assume that the non-linearity for higher energies was an artifact created by the energy calibration. Since the first order polynomial cannot model the characteristics of the detector as accurately as a higher polynomial could, there might be systematical errors for the low energy γ-depositions. As the phonon energy is used to define the light yield, this error could cause the non-linear behavior of the γ-band.

In order to cross-check this, Figure 4.7 shows the light yield of the γ-band for the detector pair *Verena/Q* again. In this plot however, the phonon detector calibration relies on a polynomial of third order and uses the 727 keV peak as the energy reference. The phonon energies of this calibration are systematically higher than these obtained with the α-calibration, since the γ-calibration compensates for the increased scintillation light production of γ-particles (see equation (4.11)).

This difference is the basic concept for the energy balance method. With the phonon energies increased and the light energies remaining the same, all events obtain a lower light yield. This is visible when comparing the position of the γ-bands in the two plots. Nonetheless, although the points forming the γ-band are shifted to lower energies and higher light yields, the non-linearity of the γ-band remains.

4.6. Method 2: The Scintillating Foil as a Standard Candle

4.6.1. Principle of Operation

One can determine the light output of the crystals at mK temperatures in the CRESST experiment itself. Since the housing of the detector modules is closed, a measurement during the operation of the experiment has to make use of the individual light detectors of the modules. In such a measurement, one needs to compensate for the individual characteristics of the detector modules in terms of light transport.

The question of the light transport can be answered with the measurement of a reference signal coming from a *standard candle*. The light transport has to affect the light of this standard candle in the same manner as it affects the scintillation light of the respective crystal. Because there is no common line of sight, it is not possible to use the very same standard candle in the measurements. In contrast, every detector module needs its own.

The scintillating housing of the detector modules itself can serve as such a standard candle. In every module, the housing consists of a reflecting scin-

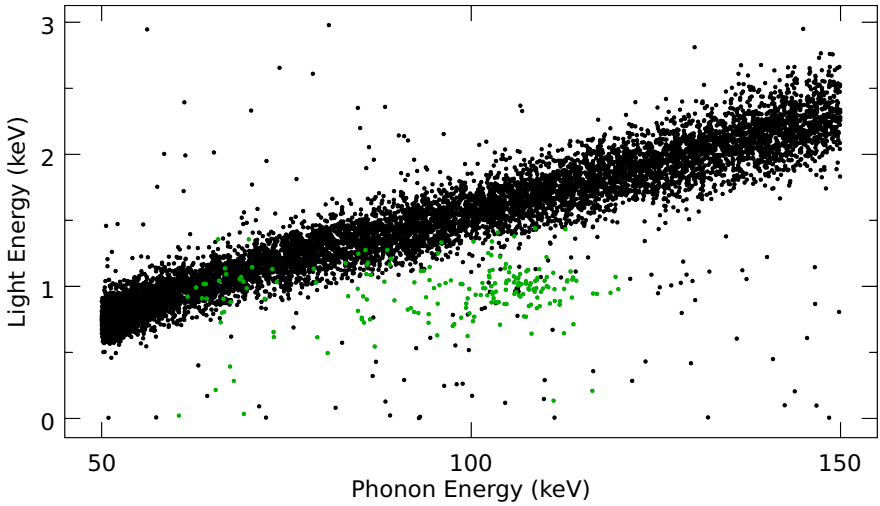

Figure 4.8.: Detail of the Phonon/Light plot of *Verena/Q*. The green dots indicate α-decays where only the recoiling nucleus hits the detector crystal while the α-particle impinges the housing. The events were selected using to the procedure introduced in Section 4.6.3.

tillating foil which helps discriminating certain α-decays (see Section 2.2.1). This foil is the same in every detector module, so the light production characteristics of the individual housings are identical.

If the light from the foil propagated along a completely different path than the light of the crystals, this method would have been be prone to a systematic error. This is improbable for the following reason: once the light from the foil enters the crystal, it is subject to the same transmittance and reflection effects as the crystal scintillation effects. Hence, the requirement for a completely different path would mean that the light from the foil propagated to the light detector along the gap between the crystal and the foil and thus completely avoid entering the crystal. Especially for foil regions which are not directly facing the detector, such a path is hardly possible.

As described in Section 2.2.1, most of the events in which the foil scintillates are absorptions of α-particles from the decay of ^{210}Po on the surfaces of either the crystal or the housing. In these processes, the α-particles leave their point of origin towards the scintillating foil. The recoiling daughter nuclei impinge into the scintillator crystal. Since Pb nuclei are very massive objects, they produce hardly any scintillation light but only trigger a phonon signal.

Figure 4.8 is a phonon/light plot of events recorded with the module *Verena/Q*. The foil scintillation events are marked in green. In contrast to the γ-band, the population of the foil events does not seem to have a slope. On the phonon axis, their energies reach up to $\approx 110\,\mathrm{keV}$ while on the light axis, their energy remains constant. This behavior comes from the fact that all these pulses have approximately the same α-energy, producing the same amount of scintillation light in the foil.

The phonon signal on the other hand can vary, if the recoiling nucleus does not originate from the very surface of the housing. In such a case, it loses energy while exiting the foil or wins energy if the decay happens on the surface of the crystal. Consequently, the energy in the phonon channel can differ from the literature value of recoil energy for this type of decay.

4.6.2. Light Channel Parameters

In analogy to equation (4.10), the light signal of these foil events can be written as

$$L_{\mathrm{foil}} = Q_\alpha \mathfrak{C}_L X_{\mathrm{foil}} \epsilon \tag{4.28}$$

As such a measurement is only done with this single α-decay and not with other types of particles, one can include the quenching effect in the factor X. For the comparison of different modules, one can calculate a ratio R

consisting of the scintillation light of γ-absorptions of the 727 keV calibration line normalized with this foil scintillation light:

$$R = \frac{L_{727\,\mathrm{keV}}}{L_{\mathrm{foil}}} = \frac{Q_\gamma X_{\mathrm{crystal}}}{Q_\alpha X_{\mathrm{foil}}} \tag{4.29}$$

Since the light transport is the same for both types of signal, one can reduce the transport efficiency ϵ from the fraction. As both measurements use the same calibration, the calibration factor $\mathfrak{C}_L$ disappears from the fraction as well. The scintillation efficiency of the housing X_{foil}, as well as the deposited energies $Q_{\alpha,\gamma}$, are assumed to be the same for all detector modules, since the situation is always the same. Thus, the ratio only depends on the scintillation efficiency of the crystals:

$$R \propto X_{\mathrm{crystal}} \tag{4.30}$$

This makes the ratio R a measure of the scintillation efficiency of the detector module.

The light signal L_{foil} of the foil on its own carries information on the transport efficiency in the module: In equation (4.28), the values of Q_α and X_{foil} are equal for all modules. Furthermore, if the light detectors are calibrated absolutely, the calibration factor $\mathfrak{C}_L$ is set to unity. With these assumptions, the foil signal in each detector module is directly proportional to the transport efficiency of a detector module:

$$L_{\mathrm{foil}} \propto \epsilon \tag{4.31}$$

In order to determine the scintillation efficiency with the standard candle method, one does not need an absolute calibration of the light detector. The calibration factor is reduced anyway, as it is involved in both the numerator and the denominator of the relation R. For the transport efficiency on the other hand, the absolute light detector calibration is an essential prerequisite.

In this kind of measurement, the fraction of light which is re-absorbed and converted to phonons in the crystal only contributes to the transport efficiency value indicated by L_{foil}. Both, the light from the foil and from the crystal are subject to those re-absorptions in the same way. Therefore, their ratio R is not affected by the re-absorption as its effect cancels out.

4.6.3. Decay Time Cut for the Foil Events

The foil is a much faster scintillator than a $CaWO_4$ crystal. Exploiting this fact, one can discriminate the foil and the crystal events by comparing the shape of their pulses:

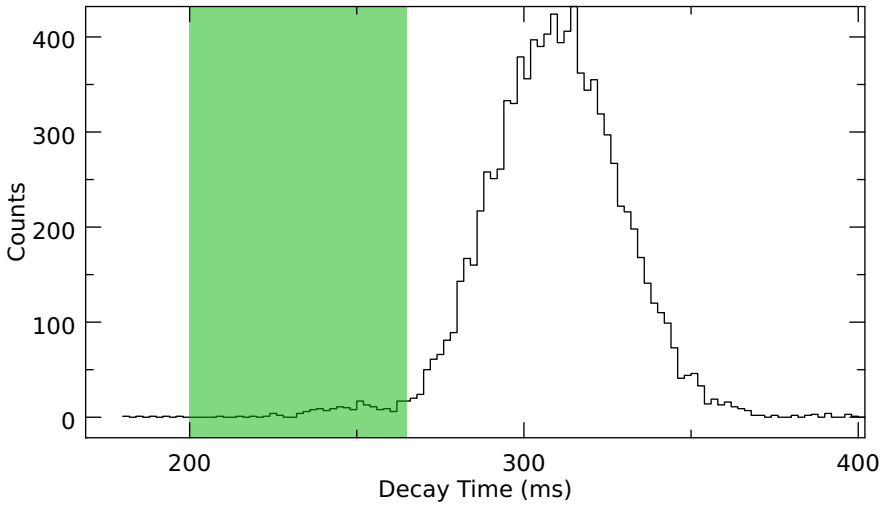

Figure 4.9.: One can discriminate between foil and crystal events by cutting on the decay time of the light detector records. This example shows the distribution of decay time for particle events with phonon energies of 60 keV to 120 keV. The region marked in green indicates the pre-selection for foil event candidates.

General Method

Using the decay time parameter from CMP, it is possible to automatically select the foil events. A phonon energy cut from 60 to 120 keV limits the data to a region that is plausible for foil events. Figure 4.9 shows the distribution of decay times for the light records of these events in the detector Q. The lower tail of this distribution contains the events of the foil, where the scintillation ceases faster. In the plot, the green region indicates the limits of the selection.

Data Cleaning

When treating composite detectors, one can prefix an additional cleaning step before the decay time cut on the light signals. The spike-shaped pulses from the detector carrier (see Section 3.3) form a band in the phonon-light-plot which can pass through the region of the foil events. By cutting on the decay time of the phonon signal after the energy cut, one can remove such events before cutting on the light signal decay times.

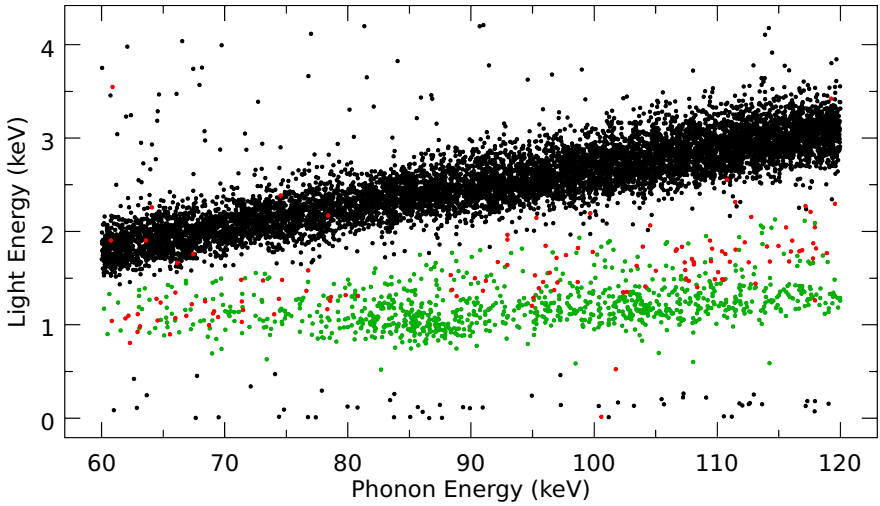

Figure 4.10.: In the $ZnWO_4$-module, it is not possible to distinguish the foil (green) from crystal events (black) by cutting on the light signal decay time. Therefore, one has to cut directly in the phonon energy/light plane. A decay time cut in the phonon signal can remove direct hits of the thermometer carrier (red) before.

For composite detectors made of $CaWO_4$, this way of pre-cleaning of the data is not strictly necessary but an easy way of removing statistical outliers of the γ-band. Yet, when analyzing the $ZnWO_4$-crystal, it is an essential prerequisite. $ZnWO_4$ is a scintillator with an afterglow time much shorter than $CaWO_4$[KMW05]. The scintillation light signals of this material are indistinguishable from the signals generated by energy depositions in the foil. Therefore, the only way of discriminating the foil events is by manually selecting the flat band of events reaching up to 100 keV in the phonon/light plane.

As shown in Figure 4.10, the cut on the phonon signal decay time identifies the carrier hits. These hits, marked in red in the plot, form a band right of the γ-band, with a similar slope. This band intersects with the foil event region. In this intersection, the carrier events would be interpreted as fake foil events.

The horizontal shift of the carrier band results from the different phonon pulse shapes for carrier and absorber crystal hits. As the pulse shape of the carrier events is completely different from the pulse shape of the standard event used in the fit, the resulting fit amplitude is wrong. This error in the fit amplitude causes an error in the energy calibration. Therefore, the carrier hits are shifted along the phonon energy axis.

After having removed these events using the phonon detector decay time, it is easier to perform the manual cut of the foil events of a $ZnWO_4$-module.

4.7. Method 3: Energy Balance

Figure 4.11 features a region of the Th-spectrum measured with the detector *Verena* using two different calibrations. As already mentioned, the calibration process compensates for eventual losses of energy in the measurement channel concerned. In the case of the phonon channel, the emission of scintillation light is an example for such an energy loss. Since the amount of scintillation light depends on the nature of the impinging particle, this special kind of energy loss is particle-dependent. When one selects a certain calibration particle, e.g. α or γ, the compensation for the emitted scintillation light is set to a fixed value which fits to the particles used for the calibration.

Since the compensation is fixed, it does not match to other particle types. Only if the measured particle is of the same type as the particles on which the calibration relies, the energy reading is correct. Otherwise, the energy reading can deviate from the deposited energy. If the quenching factor of the measured particle is higher than that of the calibration particle, the energy reading is higher as well, because there is less scintillation light and the

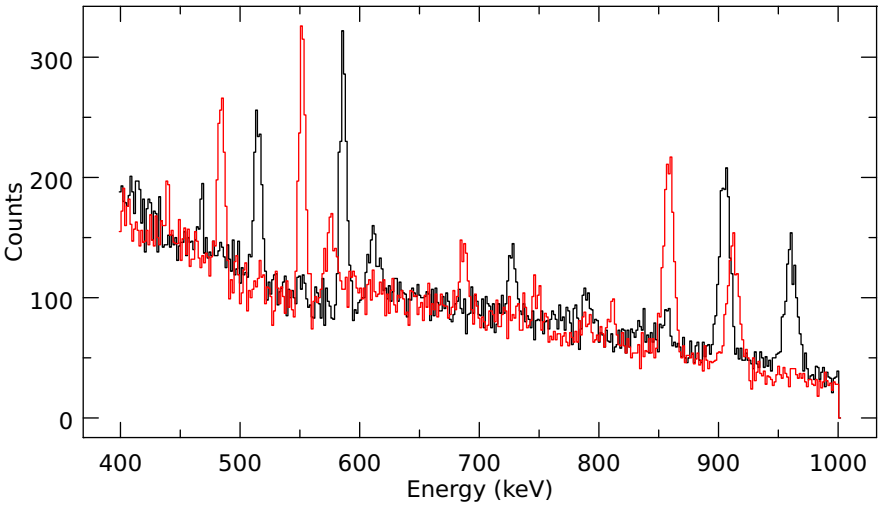

Figure 4.11.: The same γ-spectrum with different calibrations in *Verena*. With the γ-calibration (black), the lines are forced to their literature values while the α-calibration (red) stays closer to the actual phonon energy.

calibration over-compensates the loss of energy. On the other hand, if the impinging particle has a lower quenching factor than the calibration particle, the calibration cannot completely compensate for the energy loss. The difference in energy readings seen in the plot is a direct effect of the different amounts of scintillation light being emitted.

In an ideal world, one could calibrate the phonon channel using particles which do not induce any scintillation. Then, the calibration would not compensate for any scintillation effect. Consequently, such a detector would always simply yield the amount of phonons created in any particle interaction. In analogy to the absolute calibration of the light detector, such a mode of calibration could be called absolute phonon calibration.

With such an absolute phonon calibration, the difference between the literature value of the energy of a γ-line and the reading of the phonon detector would directly yield the amount of scintillation light. A light detector under absolute calibration could determine the transport efficiency in an easy way:

Given a γ-particle ($QF = 1$) of 100 keV is detected. If the phonon channel reads 80 keV, this means that the 20 keV have left the crystal in the form of light. Therefore, the scintillation efficiency X for this crystal is 20 %. If the module transported the light with an efficiency of $\epsilon = 100\,\%$ to the light detector, its reading would be the full 20 keV. A reading lower than this would indicate a transport efficiency $\epsilon < 100\,\%$.

Since there is no known source of particles with an infinitely high quenching factor, it is impossible to determine the scintillation and transport efficiencies in such an easy way. Nevertheless, by comparing phonon and light data from each one α- and one γ-line, one can reconstruct the ratio of the quenching factor and the calibration factor and, subsequently, extract the scintillation and transport efficiencies X and ϵ from the energy readings.

4.7.1. Quenching Factor

The quenching factor for α-particles can be extracted from the relation of the light detector readings of a γ- and an α-particle. The particle energies Q_α and Q_β can be obtained from literature, e.g. from [CEF99]. With the convention that γ-particles have a quenching factor of $QF_\gamma = 1$ one obtains:

$$\frac{L_\gamma}{L_\alpha} = \frac{\mathfrak{C}_L Q_\gamma \frac{X}{1} \epsilon}{\mathfrak{C}_L Q_\alpha \frac{X}{QF_\alpha} \epsilon} \tag{4.32}$$

$$\Rightarrow QF_\alpha = \frac{Q_\alpha}{Q_\gamma} \frac{L_\gamma}{L_\alpha} \tag{4.33}$$

Note, that for this step of the calculation, the choice of light detector calibration is not yet important, as the factor $\mathfrak{C}_L$ disappears from the result in any case. In contrast to the efficiencies, the determination of the quenching factor is possible with any light detector calibration.

4.7.2. Calibration Factors

The calibration factors $\mathfrak{C}$ themselves are not important for the performance of a detector module. However, one has to know them in order to extract the relevant information, the scintillation and transport efficiencies X and ϵ. As it was discussed in Section 4.2.2, the absolute calibration of the light detector sets the light detector calibration factor to unity:

$$\mathfrak{C}_L = 1 \tag{4.34}$$

which avoids any compensation of scintillation and transport efficiencies during the calibration. As already discussed in the context of the standard candle method, a calibration using scintillation light would make the transport efficiency contribute to the calibration factor. Then, the calibration would compensate for the losses of light due to a less-than-ideal light transport. Thus, in order to avoid a tautological equation determining the transport efficiency, the light detector has to be calibrated in an absolute manner.

For the phonon detector, the calibration can be done using both particle types. However, one has to be aware of the effect of a calibration on the energy reading. Since some part of the energy escapes the crystal as scintillation light, the remaining phonon energy reading changes with the nature of the detected particles. A calibration with α-particles means that for equation (4.7) there is the condition

$$P_\alpha \stackrel{!}{=} Q_\alpha \tag{4.35}$$

as the detector reading corresponds to the energy deposition caused by the deposition of an α-particle. The calibration factor as in equation (4.11) must compensate for the fact that some of the energy leaves the phonon detector in the form of scintillation light. For α-particles it is

$$\mathfrak{C}_{P_\alpha} = \frac{1}{1 - \frac{X}{QF_\alpha}}. \tag{4.36}$$

4.7.3. Light Channel Parameters

With the phonon calibration factor $\mathfrak{C}_{P_\alpha}$ known from above, the fraction X of energy which leaves the detector as scintillation light can be extracted from the basic equation (4.9) which describes the phonon detector reading of a γ-particle. Using the definition of $QF_\gamma = 1$, one obtains:

$$P_\gamma = \mathfrak{C}_{P_\alpha} Q_\gamma (1 - X). \tag{4.37}$$

With the calibration factor from (4.36), this means

$$P_\gamma = Q_\gamma \frac{(1 - X)}{\left(1 - \frac{X}{QF_\alpha}\right)} \tag{4.38}$$

$$\Rightarrow X = \frac{\frac{Q_\gamma}{P_\gamma} - 1}{\frac{Q_\gamma}{P_\gamma} - \frac{1}{QF_\alpha}}. \tag{4.39}$$

This operation exploits the mismatch between the particle measured (γ) and the particle used for the calibration (α). The calibration does not compensate for the scintillation in a correct way and thus the scintillation efficiency X remains in the equation. In principle, the procedure also works with a γ-calibration, under the condition that an α-particle is measured.

One can then extract the last parameter, the transport efficiency ϵ of the detector module from any light detector reading where the quenching factor of the impinging particle is known. The simplest case is a γ-particle:

$$L_\gamma = Q_\gamma X \epsilon \tag{4.40}$$

$$\Rightarrow \epsilon = \frac{L_\gamma}{Q_\gamma X} \tag{4.41}$$

In principle, the calculation of X is as well possible with the phonon detector readings of two different types of nuclear recoils with the quenching factors and the deposited energies known.

In the case of this analysis method, the re-conversion of light into phonons in the crystal contributes to the scintillation efficiency, as the re-absorbed light is seen by the phonon detector.

4.7.4. Selection of Data Points

Calculating the three basic quantities, QF, X and ϵ requires the measurement of two known lines from different types of radioactive decays. One needs

Detector	*Boris*/PMT (%)	R	σ_R	X (%)	σ_X
Verena (combined)	108.6	11.68	0.33	6.662	0.058
Verena/Burkhard	108.6	10.59	0.60	6.725	0.084
Verena/Q	108.6	11.46	0.16	6.612	0.050
Rita/Steven	131.1	11.45	0.60	6.76	0.20
Wibke/X	100.0	9.49	0.22	5.02	0.69
ZnWO4/Ulrich	108.3	11.36	0.42	6.36	0.22
Maja/Hans	110.2	10.38	0.19	6.06	0.12

Table 4.3.: The scintillation efficiency, determined with the three different methods. First, the room temperature PM tube measurement compared to the reference crystal *Boris*, then the ratio R of scintillation in the crystal for a 727 keV γ-peak and the scintillation of the foil, and last the scintillation efficiency X from the energy balance calculation. The latter two, both measured under cryogenic conditions, are given with their errors according to Gaussian error propagation.

to determine the light energy of both these lines and the phonon energy of one of them.

Since the calculation makes use of the definition that γ-particles have a quenching factor of 1, one of the lines needs to be a γ-line. The second line can be any other line with a quenching factor $QF \neq 1$.

The results discussed in this thesis rely on measurements of the following data: The γ-line is ^{212}Bi ($Q = 727\,\text{keV}$) the same that was used for standard candle method already. Both, the phonon and the light detector reading of this line contribute to the calculation.

The second light detector reading is the α-line of ^{180}W ($Q = 2516\,\text{keV}$). In principle, it would have been possible to use ^{147}Sm ($Q = 2311\,\text{keV}$), the same line that was already the reference for the α-calibration. Nevertheless, ^{147}Sm was not suitable as a common reference for all the crystals because the amount of scintillation light induced by it was subject to severe variations due to a surface effect in the $ZnWO_4$-crystal [Pet11].

4.8. Comparison of Results

The tables 4.3 and 4.4 contain the values for the scintillation and the transport efficiency determined with the different methods. The systematical errors for the values R, X, L_{Foil} and ϵ are based on the errors of the phonon

Detector	L_{Foil} (keV)	$\sigma_{L_{\text{Foil}}}$	ϵ (%)	σ_ϵ
Verena (combined)	1.872	0.047	41.29	0.86
Verena/Burkhard	0.827	0.037	17.91	0.71
Verena/Q	0.977	0.013	23.28	0.20
Rita/Steven	1.550	0.060	36.1	1.8
Wibke/X	1.136	0.025	29.6	4.0
ZnWO4/Ulrich	1.217	0.034	29.9	1.3
Maja/Hans	1.192	0.017	28.05	0.64

Table 4.4.: The transport efficiency, first in terms of the scintillation light L_{Foil} coming from the foil and then as the value ϵ extracted from the energy balance calculation. Both values given with their errors according to Gaussian error propagation.

and light detector calibration described in Section 4.5.2. In case of the foil signal L_{Foil}, the percental error is directly applied. For the other values, the calibration errors contribute to the final error according to the Gaussian error propagation. The statistical errors come from the fit of Gaussians to the phonon and light detector peaks, where the error of the fitted peak position is taken as the error. Again, the error for L_{Foil} is the direct result of the fit, whereas in case of the other values, the errors are estimated using Gauss' law of quadratically adding the errors.

The detector module *Verena* requires a special treatment. It is equipped with two light detectors, *Burkhard* and *Q*, one at each face of the cylindrical crystal. The detector *Q* is located at the usual position, next to the roughened surface of the scintillator crystal. *Burkhard* on the other hand, faces the crystal at the opposite side, next to the phonon detector.

This double-light-detector module was built in order to answer the questions of how the light spreads inside the module and of how well the reflective housing performs. If both light detectors gather light without influencing each other, the collection efficiencies of the individual detectors should be comparable to those of light detectors of conventional modules. Consequently, the sum of their signals should reach twice the amount of light gathered in a conventional module.

On the other hand, the amount of collectible light in a module is clearly finite. If a single light detector could already collect all this light on its own, an additional detector would "steal" a part of the energy away from the primary light detector. The two light detectors in sum could maximally gather as much light as a single light detector on its own.

In addition to the values obtained with the individual light detectors, there are values for the scintillation and transport efficiency regarding the combination of the two light detectors. Since energy readings are the base of all calculations, it is reasonable to sum up the energy gathered by the two light detectors. Consequently, the scintillation efficiency X of *Verena* is the average of the values of its components. The transport efficiency ϵ on the other hand is the sum of its components. An estimation of the errors relies on the Gaussian law of error propagation, similar to the case of the single-light-detector modules.

The three methods, the *Boris*/PMT, the standard candle and the energy balance method measure the same properties of the detector modules. However, the fraction of light that the crystal re-converts to phonons is treated differently in each of the methods. Therefore, it makes no sense to compare the results by fitting one to the other, as it is not possible to take into account the re-converted phonons. Instead, the discussion will focus on a visual comparison of how the values are distributed with the different methods.

4.8.1. Scintillation Efficiency

The values of Table 4.3 are visualized in the Figures 4.12 through 4.14. All figures start with a value of 0, in order to compare the variation of the values over the entire possible scale.

One can see that in all three figures, the variation of the values is similar. The only extraordinary crystals are *Rita* which gives a high value with the *Boris*/PMT method and *Wibke* which has a low scintillation efficiency value. However, the *Boris*/PMT method is measured at a different temperature, and the error of the *Wibke* value is large. Thus, one can assume that in terms of light production, all modules behave in a similar way.

4.8.2. Transport Efficiency

Concrete numbers for the transport efficiencies of the modules can only be obtained with the standard candle and the energy balance method since only these process data from assembled modules.

Looking at Figure 4.15 and Figure 4.16, one can observe that for the light transport, the variation between different modules is much larger than for the light production. In addition, the individual crystals show the same systematic behavior in both measurements. This is visible even better in Figure 4.17, where the values of the two methods are plotted against each other. The straight line fitted to the points emphasizes this.

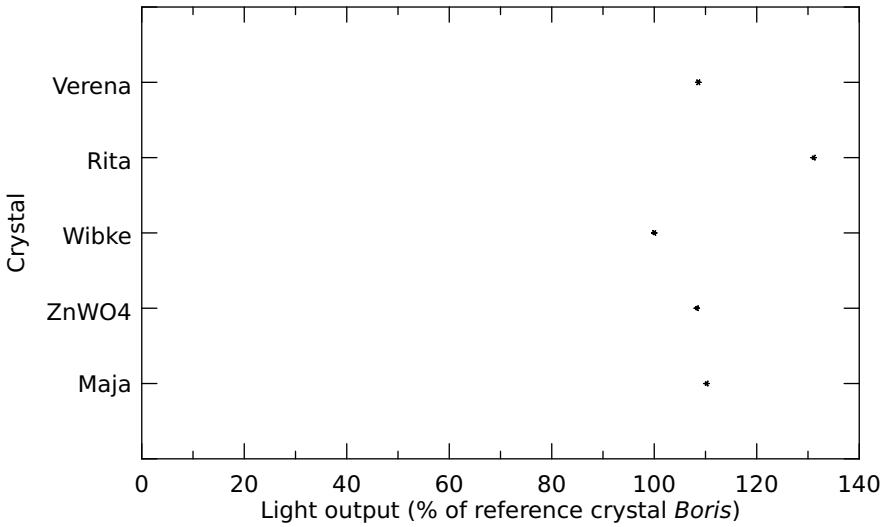

Figure 4.12.: Scintillation efficiencies obtained with the *Boris*/PMT method.

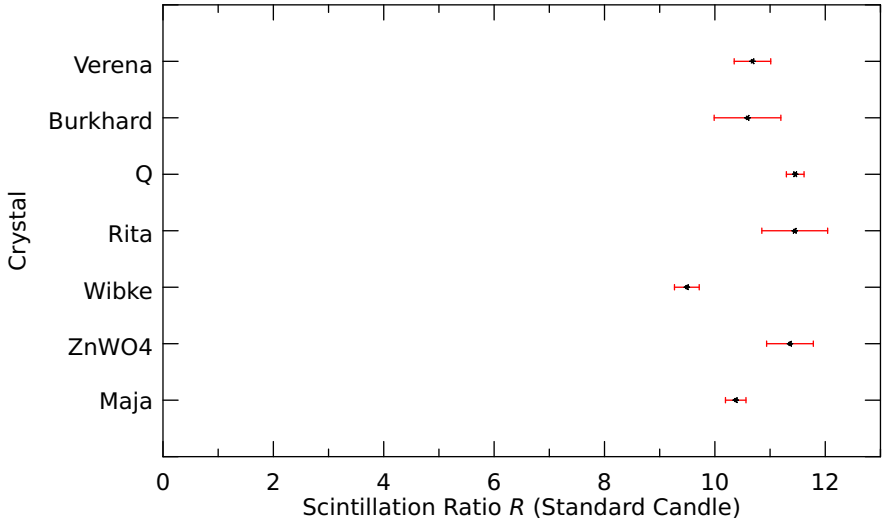

Figure 4.13.: Scintillation efficiencies determined by using the standard candle method.

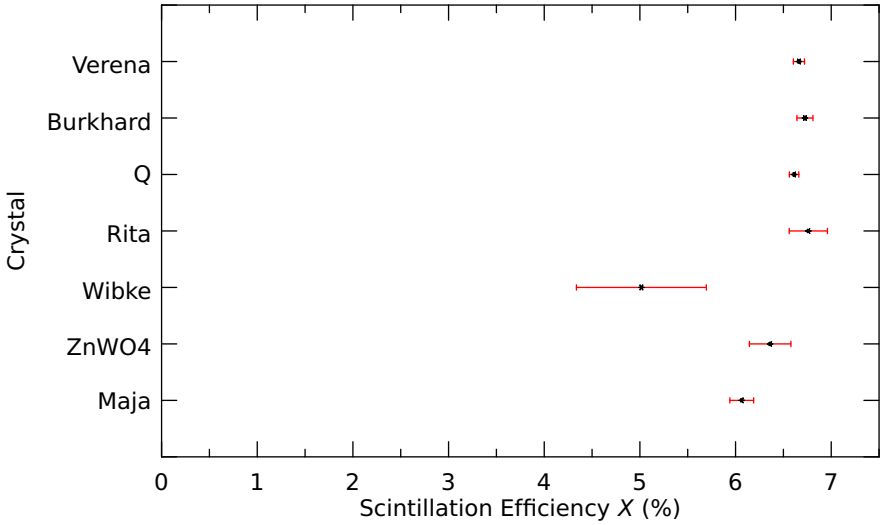

Figure 4.14.: Scintillation efficiencies determined by using the energy balance method.

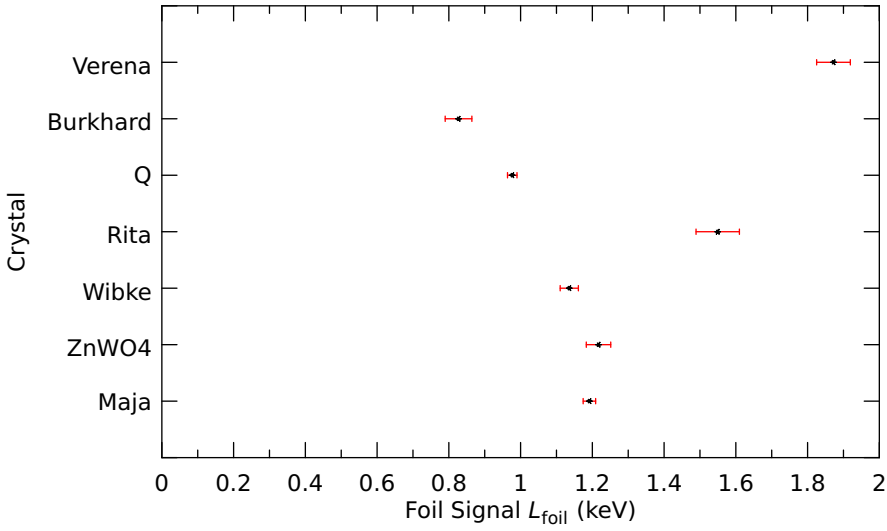

Figure 4.15.: Transport efficiencies indicated by the light signals of the foil events.

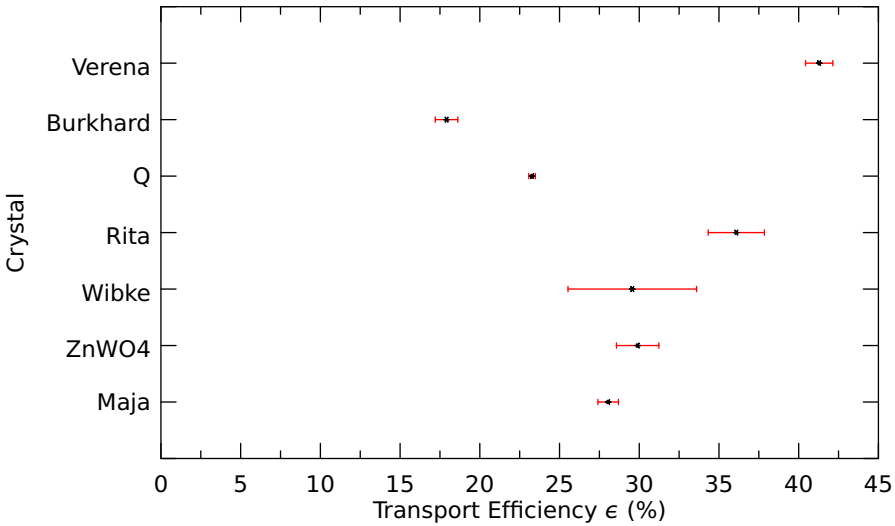

Figure 4.16.: Transport efficiencies obtained with the energy balance method.

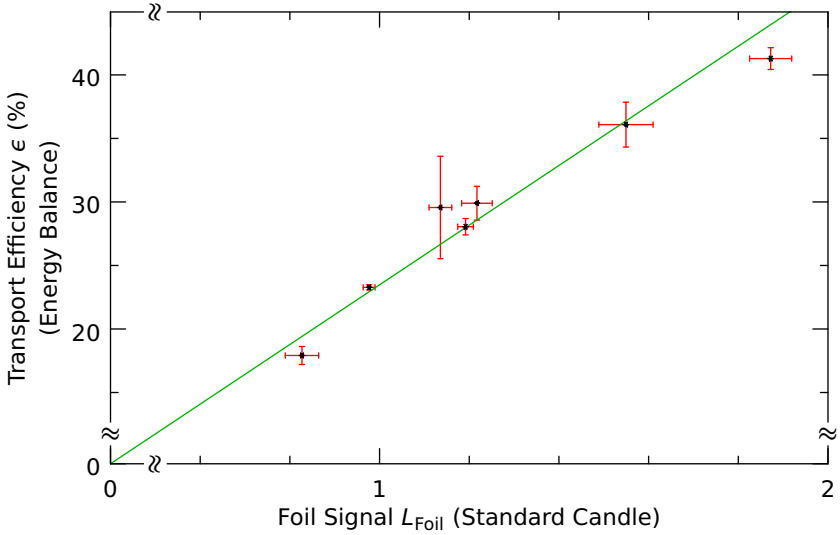

Figure 4.17.: Comparison of the transport efficiencies obtained with the energy balance and the standard candle method.

Detector Module	$X \cdot \epsilon$ (%)	$\sigma_{X \cdot \epsilon}$
Verena/combined	2.751	0.062
Verena/Burkhard	1.539	0.018
Verena/Q	1.205	0.050
Rita/Steven	2.440	0.013
Wibke/X	1.483	0.028
$ZnWO_4$/Ulrich	1.902	0.010
Maja/Hans	1.701	0.052

Table 4.5.: The fraction of energy of a γ-absorption that is seen as scintillation light in different detector modules

4.8.3. Discussion

The variation of the light production is not as big as the variation of the light transport among the different modules. In addition, the transport efficiency values of the standard candle method and the energy balance method are in good accordance with each other. In total, the light transport seems to bear a big possibility for optimization. The step from the lowest to the highest value is nearly 50 %.

This variation in the transport efficiency could have several reasons:

- The variation could be in the opacity of the crystals. As the light reflects several times in the module before being absorbed, already small variations of the opacity could have a big effect.
- The alignment of the reflective foil is slightly different in each module, since the foil bends easily. Again, the many reflections could add up to relatively high differences between the transport efficiencies of the different modules.

When Run 32 is finished and the detector modules have been dismounted, it might be possible to measure the opacity of the crystals, e.g. using a well-defined light source and the photomultiplier. The characteristics of the foil assembly on the other hand are difficult to determine. Such an investigation would need a controlled way of deploying the foil inside the module housing and measuring the influence of the positioning on the light transport efficiency.

The determination of scintillation and transport efficiency makes it possible to check whether the two alternative designs provide better modules:

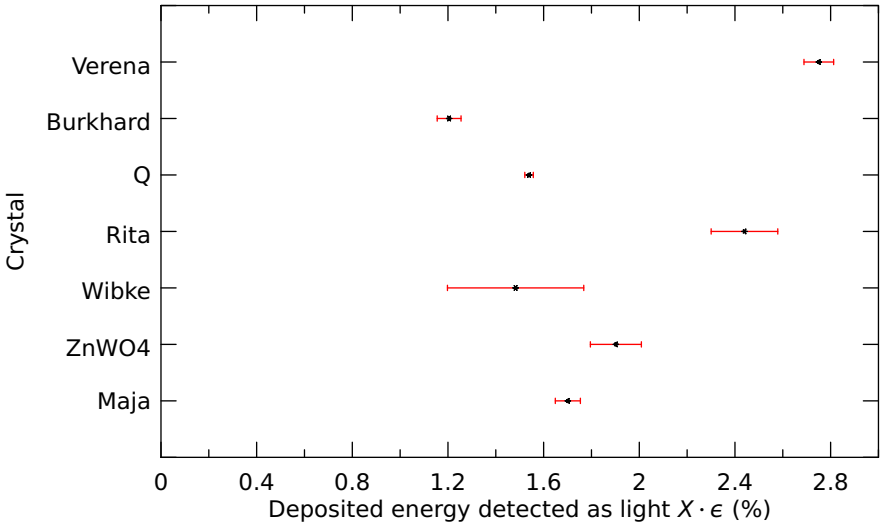

Figure 4.18.: The fraction of deposited energy seen by the light detectors, obtained with the Energy balance method.

In terms of the scintillation efficiency, there seems to be no significant effect. However, in terms of the transport efficiency, the composite detectors are equal to or better than conventional modules.

The product of the two efficiencies (see Table 4.5 and Figure 4.18) is the fraction of the deposited energy that arrives in the light detector in the form of scintillation light. This is the relevant information for the calibration factor and at the end for the Dark Matter analysis. In terms of this amount of detected light, even the worst composite module is still a factor of 1.1 better than the best conventional module. The best composite module excels the best conventional module even by a factor of 1.6.

The light transport efficiency can also help to solve a question related to the double-light-detector module. It could be possible that the two detectors "steal" light from each other or that light which leaves the crystal towards one light detector could not be seen by the other detector in any case.

The actual result is in between the two extremes: When looking at them individually, *Burkhard* and *Q* are the two detectors with the lowest transport efficiencies. This hints towards the idea of the concurrent light detectors. Yet, when adding up the signals of the light detectors, the combined values of the module *Q/Verena/Burkhard* shows the best performance of all the de-

tector modules investigated. It achieves a transport efficiency of over 40 %. The best single- light-detector module achieves only 36 % while the average for single-light-detector modules is 31 %.

This implies that in a standard module, the single light detector does not absorb the entire amount of collectible light. It appears as if the remaining light does not have the possibility to reach the position of the light detector at all, so that it can never be seen in a single-light-detector module. Therefore, it might be possible to increase the amplitude of the light signal by modifying the design of the detector modules.

4.9. Summary

The CRESST-II experiment relies on active background discrimination on an event-by-event-basis. The discrimination criterion is the scintillation light: Different types of particles produce different amounts of light, a characteristic which is described by the quenching factor.

In the analysis, particles of different quenching factor show up in bands of different light yield. These bands are separable down to a certain threshold of deposited energy. Below this threshold, the bands overlap more and more, and event discrimination becomes more and more difficult. The width of these bands is partially determined by the amount of detected light. An increased amount of detected light reduces the width of the bands. Thus, it is crucial to increase the amount of detected light in order to improve the discrimination at low energies.

The amount of produced light depends on the material of the scintillator crystal. Composite detectors allow for a better control of the stoichiometry of the crystals. In addition, alternative materials as for example $ZnWO_4$ are easier to obtain and have scintillation capabilities at least equal to $CaWO_4$. This is beneficial for the scintillation efficiency. Handling of $ZnWO_4$ in CRESST is only possible with a composite detector design. Composite detectors of both $CaWO_4$ as well as $ZnWO_4$ are part of the CRESST Run 32.

The importance of the light channel has lead to the desire of characterizing the detector modules with respect to their light detection capabilities. Up to now, the only aspect which has been investigated was the behavior of the crystals at ambient temperature. This basic method compares the γ-induced scintillation of the tested crystals to the scintillation of a reference crystal. The reliability of this method is doubtful as the scintillation properties of $CaWO_4$ are temperature dependent [KMW05]. In addition to this ex situ characteristic, the method does not yield information on whether light *production* or light *transport* are the dominant effect. Thus, one does neither

know how big an improvement could possibly be nor what would be the most promising way to improve the modules at first hand.

The present work introduces two alternative methods for evaluating the light production. Both these new methods use data obtained under cryogenic conditions, during the actual running time of the experiment. The standard candle method compares the γ-induced scintillation of the sample crystals to α-induced scintillation in the detector module housing. The energy balance method calculates the scintillation efficiency from the phonon and light signals of an α-line and a γ-line of known energies.

For the *Boris*/PMT measurement, spectral corrections were necessary respecting the differences between the $CaWO_4$ and $ZnWO_4$ crystals in terms of the scintillation characteristics. Since the two new methods use the data from the experiment itself, there is no need for a special treatment for alternative scintillator materials.

The result of the three methods are not directly comparable since the reabsorption of light inside the crystal affects all methods in a different way. However, the variation of the values shows that for all three methods, the light production does not vary over a large scale for the different crystals in any case.

In addition to this so-called scintillation efficiency, the two new methods can determine the efficiency at which the detector module transports light from the point in the crystal where the energy deposition takes place to the light detector. The results of the two new methods are consistent in terms of the light transport efficiencies.

However, the individual efficiencies are not of big relevance for a Dark Matter analysis, since both effects could compensate each other. The product of the two efficiencies yields the relation between the energy deposited in the crystal and the light seen by the light detector. This overall efficiency is vital for the discrimination capability of the detector modules. In terms of this overall efficiency, composite detector modules of both materials are better than the conventional modules.

Run 32 featured a special module with two light detectors. The *Boris*/PMT method is not capable of evaluating an assembled module. The results obtained with the new methods indicate that the light signal could be further enhanced by reviewing the design of the module housing and its influence on the light detection in CRESST.

5. Local Variations of Scintillation and Transport Efficiency

The methods discussed in Chapter 4 provide values for the scintillation and transport efficiencies of the *entire* detector modules. These efficiencies do not contain information on whether a crystal has *regions* of high and low efficiency.

Such a local variation could be problematic in two ways: on the one hand, it would deteriorate the resolution of the light channel. On the other hand and more seriously, it could affect the background discrimination:

If there is an external low-energetic γ- or β-source, its radiation gets absorbed in the volume close to the surface of the crystals. If the surface region has different characteristics than the bulk material, methods developed for dealing with internal background will not treat these events in a correct way. Consequently, in order to correctly handle each event, it would be necessary to individually consider it depending on its origin. But then, since the source of a background event is not known a priori, the discrimination of background would hardly be possible.

Therefore, it is important to know whether detector modules have a position dependence in respect to the scintillation light. If they have such a locally changing behavior, one also needs to know the magnitude of its impact on the analysis.

Furthermore, the light detector does not necessarily have the same sensitivity at every possible region on the wafer where light can be absorbed. This variation also enlarges the width of the bands and therefore disturbs the event discrimination.

The method presented in Section 5.1 uses statistical means for obtaining the position dependence of the crystal from in-situ data of the CRESST-II experiment.

Section 5.2 starts with the results of this analysis. Subsequently, the analysis is extended to other sources of variations, as photon statistics and local variations of the light detector sensitivity.

5.1. Extraction of Information from Correlated Data

5.1.1. Statistical Quantities

Standard Deviation and Variance

The variance of the light detector measurement can be written as

$$V_{E_L} = V_R + V_P. \tag{5.1}$$

Here, the term V_R stands for the random contributions and V_P refers to the position dependence of the light signal. The following analysis method can give an impression on how much the position dependence contributes to the total resolution of the measurement.

Linear Combination of Random Variables

Mathematically, one can see the measurement uncertainties as random variables. The term V_R describes the entirely random contributions. When depositing energy at arbitrarily selected locations in the crystal, the term V_P appears also as random. In contrast, if there is information about the position at which the energy was deposited, this term loses its randomness.

Equation (5.1) is only a special case of a linear combination of random variables. According to [ZBS04], in a linear combination D of random variables X_i as

$$D = \sum_i a_i X_i, \tag{5.2}$$

the variance of the linear combination is

$$V_D = \sum_i {a_i}^2 V_i + \sum_i \sum_{j \neq i} a_i a_j C_{ij}. \tag{5.3}$$

Here, the V_i are the variances of the variables X_i, and the term C_{ij} is called the covariance of the variables X_i and X_j. It is defined as

$$C_{ij} = E\left(\left(X_i - \mu_i\right)\left(X_j - \mu_j\right)\right), \tag{5.4}$$

where E stands for the expectation operator and $\mu_{i,j}$ for the expectation values of the random variables $X_{i,j}$. One can see that the variance is just a special case of the covariance where the indices i and j are identical:

$$V_i = C_{ii} = E\left(\left(X_i - \mu_i\right)^2\right). \tag{5.5}$$

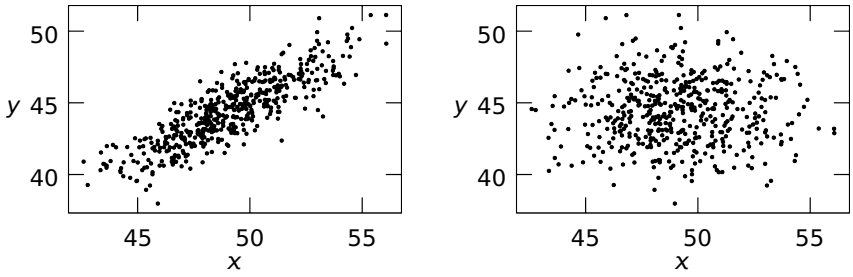

(a) Correlated data: $r = 0.65$, $C = 4.88$ (b) Re-arranged: $r < 0.01$, $C = 0.04$

Figure 5.1.: The correlation coefficient describes how strong a presumed correlation of two sets of data is. Plot (a) shows a set of (x, y) pairs of correlated data. For plot (b), the same set of data was used but the correlation was broken by re-arranging the pairs. In both plots, the variances of the X and Y data sets stay the same but the covariance and the correlation coefficient changes.

The covariance gives an impression on how regularly two random variables deviate *together* from their mean. Consider a case where the variable x_j systematically grows with the variable x_i. Then, the covariance has a positive value since positive and negative deviations tend to occur at the same time in both variables. If both deviations likely have the same sign, their product tends to be positive.

If one variable decreases while the other increases, the individual products of the deviations are negative and with them also their sum, the covariance. If there is no connection between the variables, as in case of the position dependence and the random noise, the covariance becomes zero. Therefore, equation (5.1) is the outcome of adding two uncorrelated random variables.

Putting the covariance of the data sets X and Y in relation to their individual variances leads to the correlation coefficient r:

$$r = \frac{C_{XY}}{\sqrt{V_X V_Y}} \tag{5.6}$$

The plots in Figure 5.1 illustrate how the variances, the covariance and the correlation coefficient of two sets of data behave. Both plots have been generated using the same data sets for creating the point coordinates. In one case, the coordinate pairs consisted of x-data and their matching y-counterparts, in the other case, the pairs were re-arranged so that the x- and y-data do not

match any more. As the individual data were the same, the variances are $V_X = 6.34$ and $V_Y = 5.18$ in both cases. However, when looking at plot (a) one assumes a correlation between the data while in plot (b), the data do not seem to be correlated. The covariance and the correlation coefficient reflect this difference: for the matching pairs $r = 0.85$ and $C = 4.88$ while in the other case $r < 0.01$ and $C = 0.04$. The correlation coefficient is an useful way to objectively describe the illustrated behavior.

According to [Pre+92], the correlation coefficient is no suitable mean for deciding *whether or not* two sets of data are correlated, but only for the *strength of a presumed correlation*. This means, one first has to ensure that the variables are correlated, in order to make the correlation coefficient a meaningful figure.

5.1.2. Extraction of Position Dependent Variations

One can assume that the light production and transport properties of a certain location in a detector module do not vary on a timescale of seconds. This means that if one observes two particle interactions which happen at the same location and one shortly after the other, systematic variations of these efficiencies are much smaller than random variations. Both variations affect the overall variance of the measurements, and it is possible to extract information on how much both parts contribute to the total.

For this, one needs two sets of paired light measurements. The criterion for a pair is that both events took place at the same location in the crystal. Different pairs in contrast, will most probably originate from different positions in the crystal. As the position of the parts of a pair is the same, the light output of these measurements will be correlated according to the position dependence. The correlation coefficient thus gives an impression on how largely the position dependence contributes to the overall variation.

5.1.3. Data of Localized Depositions

Ensuring that the data for the analysis come from the same location in the crystal is vital for the method. The data gathered with the CRESST detectors do not directly contain spatial information. Therefore, one needs a way of using implicit information of the data to conclude on whether or not two events happened at the same position.

Some detectors are contaminated with radionuclides of the ^{232}Th-decay chain. This chain contains the following sub-chain:

$$^{220}\mathrm{Rn} \rightarrow {}^{216}\mathrm{Po} \rightarrow {}^{212}\mathrm{Pb} \tag{5.7}$$

The decays have energies of $Q_{\mathrm{Rn}} = 6404.67\,\mathrm{keV}$ and $Q_{\mathrm{Po}} = 6906.3\,\mathrm{keV}$. Their half-lives are $T_{1/2,\mathrm{Rn}} = 55.6\,\mathrm{s}$ and $T_{1/2,\mathrm{Po}} = 0.145\,\mathrm{s}$ respectively [Son10].

The short half-life of the ^{216}Po-nuclei means that after 2 s, all but $\approx 1/7000$ of the nuclei have decayed. The observation of an independent 6.9 MeV-α-decay in this short time window is very improbable: the detector with the highest count rate of 6.9 MeV-α-events is *Verena* with 610 events during a measuring time of 339 d. This means these events occur at an average rate of $2 \times 10^{-6}\,\mathrm{s}^{-1}$.

Therefore, if one selects 6.9 MeV α-events which follow 6.4 MeV α-events in a time window of 2 s, the chance of seeing a random coincidence is low enough to assume that both events stem from the same decaying nucleus. Since the daughter nucleus does not recoil along notable distances inside the bulk material of the crystal, one can furthermore assume that it has stayed at the same location. Therefore, when undergoing the second decay, the α-event has the same scintillation characteristics, in terms of light production and transport, as its predecessor.

Thus, one can use the measurements of these two nuclides of the ^{232}Th-chain as the data for the statistical analysis. Of the ten modules that have been working in Run 32, only two, namely *Rita* and *Verena*, had enough statistics for this kind of analysis.

In the cases of both these detectors, the data treatment that was described in Section 4.5 was not sufficient to handle the extremely high phonon energies. Therefore modifications of the fit and the calibration procedures were necessary. These modifications only affect the identification of the lines. Since they have no further importance (e.g. for calculations of energy-dependent parameters), their description follows in appendix A.

5.1.4. Calculation

In order to estimate the covariance as defined in equation (5.4), it is possible to calculate the *sample covariance* directly from the ordered data. Given are two sets of data X and Y which have n entries x_1 to x_n and y_1 to y_n. The definition of the sample variance V of the two data sets is

$$V_X = \frac{1}{n-1} \sum_{i=1}^{n} (x_i - \bar{x})^2 \tag{5.8}$$

for the X-data, and for the Y-data:

$$V_Y = \frac{1}{n-1} \sum_{i=1}^{n} (y_i - \bar{y})^2. \tag{5.9}$$

Detector	$C_{Po,Rn}$ (keV^2)	$\sigma C_{Po,Rn}$ (keV^2)	V_{Po} (keV^2)	σV_{Po} (keV^2)	V_{Rn} (keV^2)	σV_{Rn} (keV^2)	r	σr
Burkhard	1.165	0.070	1.388	0.083	1.234	0.071	0.890	0.065
Q	1.77	0.15	2.49	0.18	1.93	0.16	0.806	0.046
Steven	0.551	0.069	1.25	0.16	0.947	0.097	0.506	0.076

Table 5.1.: Correlation coefficients and standard deviations of the measurements of ^{220}Rn and ^{216}Po using the modules *Verena/Burkhard/Q* and *Rita/Steven*.

The terms $\bar{x}$ and $\bar{y}$ are the arithmetic values of X and Y. The denominator of the normalization factor $(n-1)$ in the sample variance considers the fact that the expectation value of the variables was already estimated from the data by using the arithmetic mean.

The sample covariance C_{XY} of the two data sets is defined analogous to the sample variance as

$$C_{XY} = \frac{1}{n-1} \sum_{i=1}^{n} (x_i - \bar{x})\,(y_i - \bar{y}) \tag{5.10}$$

Using the estimates of V_X, V_Y and C_{XY}, one then can calculate the correlation coefficient $r$according to equation (5.6). The results for the detector modules *Rita/Steven* and *Verena/Burkhard/Q* can be found in Table 5.1. The table contains the variances, covariances, and the correlation coefficients of the energy readings of the two decays.

In order to obtain a measure of the errors, the variance of the sample variance, e.g. for the data set X, $\mathrm{Var}(V_X)$ can be calculated according to [Scho7] as

$$\mathrm{Var}(\mathrm{V_X}) = \frac{1}{n}\left(\mu_{4_X} - \frac{n-3}{n-1}V^2\right). \tag{5.11}$$

The therm μ_{4_X} denotes the fourth central momentum of the distribution. It can be calculated as

$$\mu_{4_X} = \frac{1}{n} \sum_{i=1}^{n} (x_i - \bar{x})^4. \tag{5.12}$$

This variance $\mathrm{Var}(\mathrm{V_X})$, and the accordingly determined $\mathrm{Var}(\mathrm{V_Y})$ can then be used in order to calculate the standard errors of the estimates.

There does not seem to exist a straightforward way for calculating the variance of the sample covariance. Therefore, in order to at least have an

impression on the order of magnitude, the error of the sample covariance is estimated as follows: Since the values for the sample variance and covariance are calculated from the same data set, the percental error should be similar. As a conservative estimate the larger of the percental errors of the two sample variances is taken as the percental error of the sample covariance. The values can also be found in Table 5.1.

5.2. Discussion

5.2.1. Possible origin of the position dependence

The data of all three light detectors have variances of similar size and positive correlation coefficients. However, in the case of the double-light-detector module *Verena/Burkhard/Q*, the data are correlated in a much stronger way than those of *Rita/Steven*. This means that for the former, the variation of the light signal depends much stronger on where in the module the deposition takes place.

Since *Verena/Burkhard/Q* is a module with light detectors at both ends, one could assume that this variation is caused by the following mechanism: If a deposition takes place near *Burkhard*, this detector could see more light than its counterpart *Q* and vice versa. Such a behavior could be called an axial position dependence, as the two light detectors are on different ends of the detector axis.

One can check for this axial dependence: if the two light detectors would "steal" light from each other, then the sum of the light seen by both of them would not show variations as large as those of the individual detectors. The light stolen from one detector would be seen by the other one which means the variation would not affect the sum value. Therefore, the correlation coefficient of the sum value would be nearly zero.

However, when doing the calculation, one obtains a value of $r = 0.65$. This means that if *Burkhard* sees a relatively large amount of light, its counterpart *Q* will also see more than the average amount of light. Thus, even if there is an axial position dependence, it is weak compared to the overall position dependence of this module that still dominates the correlation.

As *Verena* is a conventionally produced phonon detector, this non-axial position dependence might be an effect of the sensor evaporation. Near the surface of the crystal, the high temperature treatment might provoke more severe oxygen losses than in the bulk material. Oxygen deficits have already been identified as the cause for badly performing crystals in the past (cf. Chapter 3).

Light Detector	V_Δ (keV^2)	σV_Δ (keV^2)	E_L (keV)	σE_L (keV)	$E_{Q_{\gamma,\mathrm{eq}}}$ (keV)	$\sigma E_{Q_{\gamma,\mathrm{eq}}}$ (keV)
Burkhard	0.292	0.022	20.802	0.051	169	16
Q	0.887	0.076	26.040	0.064	541	68
Steven	1.10	0.14	42.359	0.059	1743	312

Table 5.2.: The variance of the difference of the Po and Rn measurements, the corresponding light energy, and the energy at which the position dependence becomes dominant for e/γ-events.

However, as in this analysis there is only one specimen of conventional and composite detectors each, further data are needed to definitively answer this question.

5.2.2. Effect of the position dependence on a Dark Matter analysis

The data for the position dependence were obtained in the MeV range, while the Dark Matter signal is expected to be relevant below 100 keV. With a few assumptions, one can estimate how large the effect of the position dependence in the low energy range can be. For a given energy, the position dependence will mostly affect data with a high light yield, namely events from the electron/γ-band. Therefore, the calculation aims at determining the energy at which the position dependent contribution will start to be the dominant part of the detector resolution in that band.

According to equation (5.3), the variance of the difference of the two measurements of ^{220}Rn and ^{216}Po looks like

$$V_\Delta = V_{\mathrm{Po}} + V_{\mathrm{Rn}} - 2C_{\mathrm{PoRn}}. \tag{5.13}$$

The correlation term is positive and thus the variance V_Δ is smaller than the sum of the individual variances V_{Po} and V_{Rn}. The graphical method shown in Appendix C uses this directly. As noted in equation (5.1), each of the individual measurements consist of one random and one position dependent term, denoted by the indices P and R. Therefore, one can expand equation (5.13) to

$$V_\Delta = V_{R,\mathrm{Po}} + V_{P,\mathrm{Po}} + V_{R,\mathrm{Rn}} + V_{P,\mathrm{Rn}} - 2C_{P,\mathrm{PoRn}} \tag{5.14}$$

The measurements of the two isotopes are in the same energy range and

therefore their variations should have approximately the same size. With

$$V_{P,\mathrm{Po}} \approx V_{P,\mathrm{Rn}} = V_P \tag{5.15}$$

for the position-dependent and

$$V_{R,\mathrm{Po}} \approx V_{R,\mathrm{Rn}} = V_R \tag{5.16}$$

for the position-independent term, one can further simplify equation (5.14) to

$$V_\Delta = 2V_R + 2V_P - 2C_{P,\mathrm{PoRn}}. \tag{5.17}$$

Since the position dependence for both measurements is the same, the C-term corresponds to the V_P-terms (see equation (5.5)). With

$$V_P = C_{P,\mathrm{PoRn}}, \tag{5.18}$$

the remaining part is

$$V_R = \frac{V_\Delta}{2}. \tag{5.19}$$

Looking back at equation (4.26), the variance of a light detector measurement can be written as

$$V_{E_L} = V_0 + V_1 E_L + V_2 {E_L}^2. \tag{5.20}$$

In this description, the position dependence will contribute to the $V_2 {E_L}^2$-term. In the most extreme case, that term is constituted entirely by the position dependence:

$$V_P = V_2 {E_L}^2. \tag{5.21}$$

Then, the random contribution corresponds to the remaining terms V_0 and V_1. For high energies, as in the case of the α-events, one can neglect the constant term V_0, so that

$$V_{E_L} = V_1 E_L + V_2 {E_L}^2 \tag{5.22}$$

and thus

$$V_R = V_1 E_L. \tag{5.23}$$

The random and the position dependent contributions V_R and V_P become equal at an energy $E_{L,\mathrm{eq}}$ of

$$E_{L,\mathrm{eq}} = \frac{V_1}{V_2} = \frac{V_R}{V_P} E_L = \frac{V_\Delta}{2V_P} E_L. \tag{5.24}$$

This corresponds (see equation (4.10)) to γ-particles of the energy

$$E_{Q_{\gamma,\mathrm{eq}}} = \frac{E_{L,\mathrm{eq}}}{X\epsilon} = \frac{1}{2}\frac{V_\Delta}{C_{P,\mathrm{PoRn}}}\frac{1}{X\epsilon}E_L, \tag{5.25}$$

The average of the energies of the ^{216}Po and ^{220}Rn light detector readings is used for E_L, the values for $X \cdot \epsilon$ are from Table 4.5.

With the results listed in Table 5.2, one can see that for the two detectors of *Verena*, the position dependence will become dominant in the range of $\mathcal{O}(100\,\mathrm{keV})$. For the composite detector *Rita*, the energy is about $\mathcal{O}(1\,\mathrm{MeV})$. Thus, in case of *Rita* the position dependence plays a clearly negligible role in the resolution of the light detector, when searching for Dark Matter events below 100 keV. In the case of *Verena*, $Q_{\gamma,\mathrm{eq}}$ is still above 100 keV for both light detectors, but detectors with even lower values might not be useful for a Dark Matter search.

5.2.3. Contribution of Photon statistics to the Light Detector Resolution

As mentioned in Section 4.3, the variance of the photon counting statistics contributes to the linear term $V_1 E_L$ of the light detector resolution V_{E_L}. The contribution of the statistics term is inevitable, but apart from the inhomogeneity of the crystal properties, there might be other mechanisms also contributing to the resolution which one can possibly control as well. The following considerations present a method of estimating whether the resolution term is solely determined by photon statistics or whether there are other effects that might be the subject of further optimizations.

When expecting a total number of N photons, the standard deviation of the Poissonian counting statistics is

$$\sigma_{N,\mathrm{stat}} = \sqrt{N}. \tag{5.26}$$

If the photons have an average energy of ε_p, the product of this average and the number of photons seen in the light detector corresponds to the energy E_L seen in the detector:

$$L = N\varepsilon_p \tag{5.27}$$

Then, the standard deviation of the energy reading is

$$\sigma_{L,\mathrm{stat}} = \sigma_{N,\mathrm{stat}}\varepsilon_p = \sqrt{N}\varepsilon_p, \tag{5.28}$$

and its variance is

$$V_{L,\mathrm{stat}} = {\sigma_{L,\mathrm{stat}}}^2 = N{\varepsilon_p}^2. \tag{5.29}$$

Detector	$V_{L,\mathrm{stat}}$ (keV^2)	$\sigma V_{L,\mathrm{stat}}$ (keV^2)	$V_{L,\mathrm{stat}}/V_R$ (%)	$\sigma V_{L,\mathrm{stat}}/V_R$ (%)
Burkhard	67.09×10^{-3}	0.78×10^{-3}	46.0	3.5
Q	5.25×10^{-2}	0.22×10^{-2}	11.8	1.1
Steven	106.37×10^{-3}	0.57×10^{-3}	19.3	2.5

Table 5.3.: The variance contributed by the photon statistics, both absolute and in relation to the random variance.

With an absolute calibration, ($\mathfrak{C}_L = 1$, see Section 4.2.2), the light detector signal from equation (4.10) becomes

$$L = E_Q \frac{X\epsilon}{QF} \tag{5.30}$$

or in terms of photon numbers:

$$N = \frac{1}{\varepsilon_p} E_Q \frac{X\epsilon}{QF}. \tag{5.31}$$

Therefore, the variance becomes

$$V_{L,\mathrm{stat}} = E_Q \frac{X\epsilon}{QF} \varepsilon_p. \tag{5.32}$$

For $CaWO_4$, assume $\varepsilon_p = 2.95\,\mathrm{eV}$ [Zde+05]. In addition, consider the values for $X\epsilon$ from Table 4.5 and the same value for E_Q as for the calculation of Table 5.2. Using these values, one can estimate the statistical variance of the light signal for the detectors *Burkhard*, *Q* and *Steven* as denoted in Table 5.3.

In Section 5.2.2, the variance was split up into a term V_P that describes the position dependence and a random term V_R. This latter term absorbs all the effects that appear random to an analysis that focuses on the correlation. One of the random contributions is the statistics term. The ratios $V_{L,\mathrm{stat}}/V_R$ listed in Table 5.3 are a measure on how largely the V_R-terms of certain detectors are determined by the photon statistics. Comparing the values of the three detectors, it is noticeable that for *Burkhard*, the counting statistics constitutes nearly half of the variance, while for *Steven* and *Q* it is much less. Thus, the statistics is only one contribution to the random part of the variance among others. Even more, in case of *Steven* and *Q*, the statistics term is only minor compared to the overall variance.

As this clearly indicates that there is another contribution to the V_R term, the question arises, what the nature of this contribution might be. A possible

candidate for another contribution to the variance is a position dependence of the light detector efficiency. This means that the light detector might have a different sensitivity, depending on the location on the wafer at which scintillation light is absorbed. While *Steven* and *Q* look at the roughened side of the crystal, *Burkhard* looks at the polished face which carries the phonon sensor.

The roughening treatment manipulates the transmittance of the crystal surfaces. When exposing a cylindrical crystal with one roughened face, as the right crystal in Figure 2.2, to UV-light, one sees that the roughened face emits light in a rather homogenous way. On the polished side, most of the light leaves the crystal at the bevel (see Figure 3.2(b)[1]). Therefore, the spatial distribution of the light leaving the crystal towards *Burkhard* is different from that of the light which *Steven* and *Q* see. Most probably, it is confined to a smaller region, as the light leaves the crystal from a smaller area. Together with the aforementioned position dependence of the light detectors, this could make the overall variance of the light signals in *Burkhard* smaller. This turn would increase the relative contribution of the counting statistics, which is not affected.

This argument relies only on one specimen. Therefore, it is necessary to further investigate in detector modules with the light detector and the phonon detector on the same crystal face. Such a modification of the detector design is relatively simple, since the light detector can be screwed to the threads on the other side of the detector holder. If a module of this geometry behaves similar to *Burkhard*, then this could be a promising way of improving the light detector resolution in Run 33 with a rather small effort.

5.3. Summary

It is possible that the light production and transport efficiencies change locally in a module. Since energy depositions can happen at arbitrary locations in the module, such a position dependence results in the broadening of the light channel signal. Even worse, if the position dependence is large enough it will result in the light yield notably depending firstly on whether the origin of an event was inside or outside the crystal and secondly on the energy-dependent penetration length of an external particle impinging the crystal. If possible at all, such an effect would be difficult to compensate for.

Because the CRESST detector modules do not produce data containing the location information, one has to look indirectly for this position dependence.

[1] The left crystal in Figure 2.2 is not roughened and therefore cannot be compared directly.

One possible way is to exploit the short half lives of two isotopes in the ^{232}Th decay chain, ^{220}Rn and ^{216}Po. The recoiling daughter nuclei of their α-decays propagate only along a negligible distance inside a solid. Thus, one can assume that both decays happen at the same location in the crystal and therefore, both are exposed to the same position-dependent light channel properties of the module.

Having identified pairs of events which belong to the aforementioned α-chain, one can obtain information on the contribution of the position dependence to the total resolution of the light detector measurement by determining the correlation coefficient directly from the data. The variance of the data contains information on the total uncertainty of the measurement, while the correlation coefficient indicates how much of these uncertainties is caused by the position dependence.

In Run 32, only the modules *Verena/Burkhard/Q* and *Rita/Steven* provided sufficient numbers of such α-signals for the analysis. The result indicates that *Verena* has a higher position dependence than *Rita*, and that in *Verena*, the position dependence is relevant for lower energies than in *Rita*. The increased position dependence is not an effect of the total amount of light splitting up between the two light detectors in *Verena*. Instead, it is plausible that the different production techniques have caused this effect. Since *Rita* is a composite detector, its crystal surface has not been affected by the oxygen loss caused by the sensor film deposition.

Furthermore, the analysis of these correlated data suggests that there is a position dependence of the light detector sensitivity. Data of the light detector *Burkhard* showed a smaller variance than that of *Q* and *Steven*. Due to the construction of the detector modules, the spatial distribution of the light leaving the crystal towards *Q* and *Steven* is visibly different than that towards *Burkhard*. A position dependence of the light detector sensitivity would relay this in the form of a wider variation of the signals and thus explain the effect. This suggests that one could easily improve the resolution by switching the position of the light detectors.

Due to the limited number of detectors that produce data for this type of analysis, there is only one specimen for each of the hypotheses. However, all these effects can potentially help to improve the resolution of the light channel without major modifications of the CRESST design. Therefore, further experiments which investigate in these effects could be of great value for CRESST.

6. Conclusions and Outlook

Various observations on different scales of size indicate the existence of Dark Matter in the form of weakly interacting massive particles called WIMPs. Extensions to the current standard model of particle physics predict particles which have properties that make them WIMP candidates. Due to the extremely low scattering cross-section of WIMPs and baryonic matter, an experiment which aims at the direct detection of WIMPs has to face low signal rates and low energies.

One of the experiments searching for Dark Matter is CRESST, the Cryogenic Rare Event Search with Superconducting Thermometers. The key techniques of this experiment are cryogenic detectors and an active background discrimination, which permit the detection and identification of particles down to the 10 keV range.

The active background discrimination relies on detectors that are based on scintillating crystals and thus have two read-out channels. The phonon channel determines the deposited energy, while the light channel determines the nature of the impinging particle. Especially the measurement of the scintillation light is a delicate issue as the energies can be below 1 keV.

Two aspects are important for the performance of the light channel: firstly, the amount of produced scintillation light, and secondly, how much of the produced light actually arrives in the detector.

Up to now, the only method for determining the properties of the scintillator crystal could be done at room temperature. With this method, it is not possible to separate the light production from the light transport. This thesis presents two approaches which both can separately determine the production and the transport properties of the detectors. These methods, in contrast to the room temperature measurement, use data obtained at temperatures in the mK-range. Hence, they are not subject to systematical errors caused by temperature-dependent crystal properties.

The so-called standard candle method uses unique events of the scintillating detector housing in order to separate the scintillation efficiency of a crystal from transport effects. The energy balance method determines the distribution of energy by comparing the signals obtained from different particles of known energy. The two new methods give consistent results both for the scintillation and the transport efficiency.

With these new methods, it was possible to determine the performance of different detector designs. In the conventional design, the phonon detector is directly evaporated onto the scintillator crystal. The composite detectors follow a modified design scheme, where the phonon detector resides on a small carrier crystal which is glued to the scintillator crystal.

The finite element simulations that have been performed within the scope of this work indicate that the two crystals of a composite detector should have their crystal axes aligned and that the layer of glue between them should be as thin as possible in order to keep the thermo-mechanical stress during the cool-down low.

The composite detector design bears several advantages: On one hand, it permits the use of scintillator materials which are too delicate to suffer an evaporation process, such as e.g. $ZnWO_4$. On the other hand, in the past, even $CaWO_4$ crystals which are the default scintillators in CRESST have shown effects of decrease of the light channel performance after the thermometer deposition. A composite detector avoids this effect.

With the new measurement methods for the scintillation and transport efficiency, it was shown that composite detectors, both with $CaWO_4$ and $ZnWO_4$ scintillators, have better performing light channels than the conventional ones.

The possibility to separately determine the light transport efficiency provided information about the light collection capabilities of the modules in general: the data of a special module with a conventional phonon detector and two light detectors indicate that such a module sees more energy in the form of scintillation light than a single-light-detector module. Therefore, in a single-detector module, a significant amount of scintillation light never arrives at the light detector at all.

Up to now, only half of the modules are equipped with calibration sources. The plans for the upcoming Run 33 include a light detector calibration source for each detector module, so that the light channel parameters of each detector module can be determined in situ.

Composite detectors show clear advantages compared to standard type detectors. Their light channels are more efficient than these of conventional detectors and they allow for the application of materials which are available more easily or have better properties than $CaWO_4$. Future runs of CRESST will benefit of these advantages.

Information concerning the distribution of the light inside a detector module can be obtained by observing the decay of each a certain radionuclide and its short-lived daughter product. These data contain information about the variation of the light channel parameters with respect to where in the crystal the energy deposition took place. The radionuclide was present in

one composite crystal and the conventional crystal that is part of the double-light-detector module. The conventional crystal showed higher variations of the light channel parameters than the composite crystal. It has been excluded that this effect is due to the distribution of light between the light detectors. Therefore, it has to be an intrinsic effect of the crystal. Whether it is characteristic for all conventional crystals needs to be clarified with additional data.

Furthermore, the data of the double-light-detector module indicate that the sensitivity of the individual detectors depends on the spatial distribution of the light that leaves the scintillator crystals. This suggests that one could easily improve the resolution of the singe-light-detector modules, simply by putting the light detectors on the polished side of the crystals.

In summary, within this work, several modifications for the CRESST-II experiment were shown. Without requiring major changes in the setup, these modifications could help to improve the discrimination capabilities in order to achieve a higher sensitivity for Dark Matter.

A. High-Energy Calibration of the Phonon Detector

For energies far beyond the scale of the test pulses, the phonon detector calibration using the test pulses as a gauge and the ^{147}Sm signal as the calibration fix point does not work reliably. For example, some crystals as *Rita* and *Verena*, have a relatively rich contamination of isotopes from the ^{235}U, the ^{238}U, and the ^{232}Th natural decay chains. The Q-values of these decays are in the range of 4000 keV to 7000 keV.

If the pulses are extremely large, the digitizer reading does not drop below the truncate level of the fit within the record length any more (see Figure A.1(a)). In such a case, the fit becomes unreliable, because the only data points which are fitted belong to the rising edge of the pulse. The resulting amplitude spectrum in Figure A.1(b) therefore has rather broad lines.

Similar to the modification described in Section 4.5 for the light detector, one can fit the data of the phonon detector with an increased truncation level as well. For *Rita*, for example, with a truncation level of 2.5 V instead of 0.8 V, the fit works better. This can be seen by the fact that the individual lines are sharper (see Figure A.2(a)). The increase of resolution for the high-energy α-lines comes at the cost of systematic errors for the lower energies. The value of 2.5 V is below the saturation level, but above the range where the detector responds strictly linear. The standard event fit can now be confronted with events slightly above the linear range and thus the fit does not produce reliable results for those relatively low energies any more.

After fitting, one has to gauge and calibrate the data in order to obtain an energy spectrum. Since the α-lines are already relatively sharp, one can try to identify one or more of them. The spectrum of Figure A.2(b) in this work was created by assuming that the most prominent line was the 5407 keV line of ^{210}Po. Compared to the uncalibrated spectrum, this one becomes sharper. The uncalibrated signal suffers from the fact that the detector response changes with time. Figure A.3 illustrates this behavior of the ^{210}Po-line. The calibration procedure takes these variations into account and compensates for them when converting fit amplitudes to energies. Therefore, the calibrated spectrum is sharper.

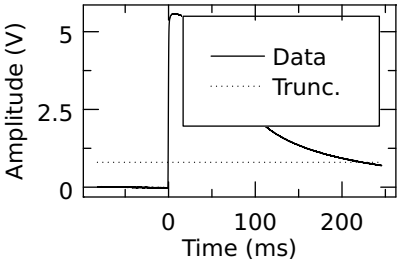

(a) Example of a high-energy pulse with the phonon detector exceeding the truncation level

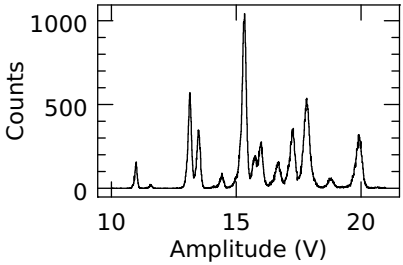

(b) High-energy spectrum of *Rita*, truncated in the linear range.

Figure A.1.: For high energy pulses as in plot (a), the fit becomes less reliable when truncating in the linear range. This happens because the pulses hardly relax below the truncation level. Consequently, the spectrum in plot (b) has a relatively bad resolution.

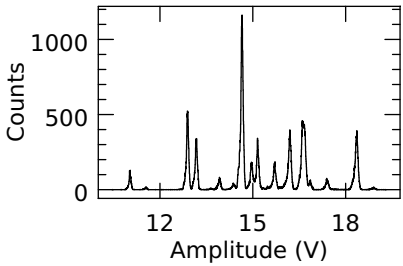

(a) Spectrum with higher truncation level.

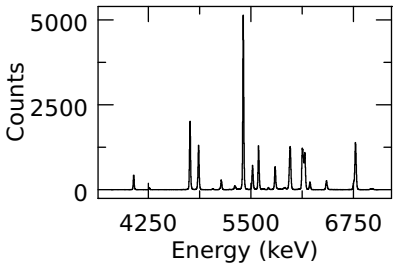

(b) Calibrated and stabilized spectrum.

Figure A.2.: The fit leading to spectrum A.1(b) can be improved by increasing the truncation level to 2.5 V. As it is shown in plot (a), the resolution of the α-lines increases. Besides assigning an energy value, the calibration compensates for temporal variations in the detector response, resulting in the sharper spectrum shown in plot (b).

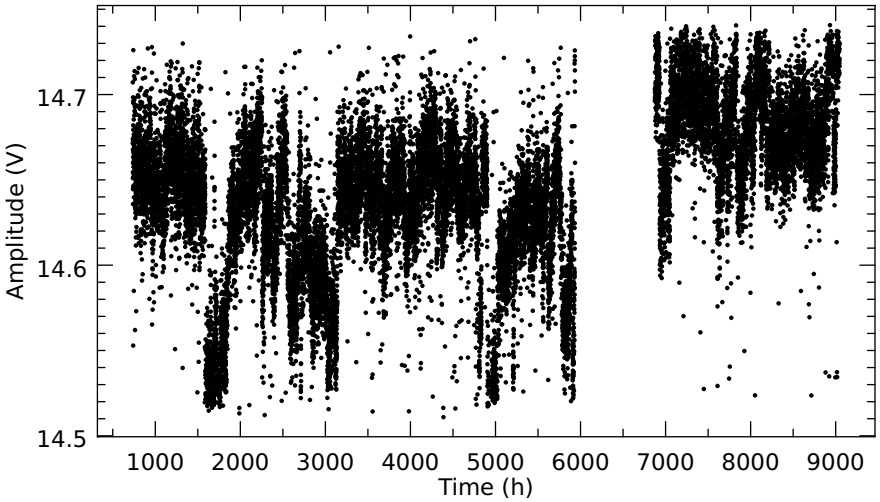

Figure A.3.: Stability of the calibration/gauging line of ^{5407}keV during the data taking of Run 32.

If a single line is not sufficient, one can extend this procedure by iteratively using more and more identified lines as gauges. Additional lines make it possible to increase the grade of the interpolation polynomial that is part of the calibration procedure.

In principle, the results of this fitting technique allow to extend the data analysis even to ranges above 10 MeV. An example can be seen in Appendix B.

B. Observation of α-Cascade Reactions

The fact that for distorted pulses, the standard event fit yields amplitudes which do not match the actual energy is not necessarily a disadvantage:

In the detector pair *Verena/Burkhard*, when looking at the α-band at an energy of about 15 000 keV there is a population of events forming a band-like substructure (see Figure B.1). In other detector pairs, e.g. Verena/Q there is no such substructure (see Figure B.2).

The Figures B.3 and B.4 show records of these events from the upper left and the lower right end of the band substructure respectively. The cause of these events are two α-absorptions which occur in a short time window. The interval between the two varies between nearly 0 up to a few 10 ms. With growing intervals, the pulse shapes from *Burkhard* and *Verena* become more and more distorted. This distortion affects the results of the standard event fit and thereupon the energy calibration, so that the energy seen by *Verena* is estimated too high.

Consequently, the data points of these events leak into the region of the next α-line at $\approx$ 16 000 keV. In the case of the pair *Verena/Burkhard*, this leakage does not happen as the double-peak structure affects the fit of the light signal in a different way than usually: The pulse temporarily drops below the truncation level. Then the fit estimates the pulse amplitude too low. This causes the population to extend downwards in terms of the light/energy plot. When the local minimum of the light detector signal is sufficiently far below the truncation threshold of the fit (see Figure B.5), this under-estimation does not exceed any further and the population spreads only to the right, following the over-estimation of the phonon signal.

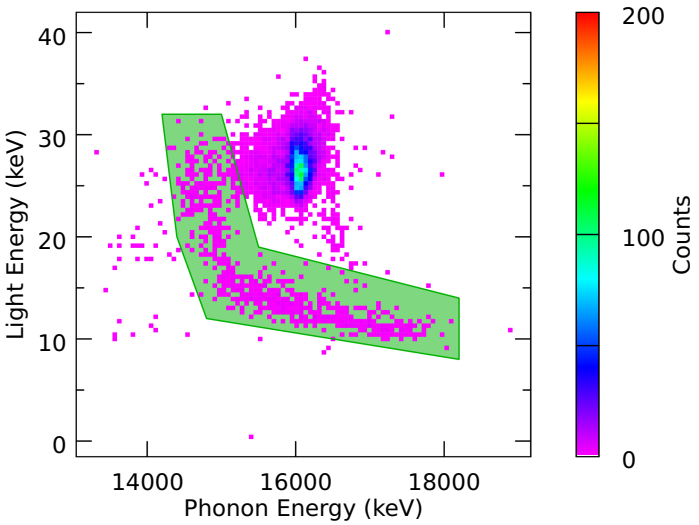

Figure B.1.: The region of α-cascades in the light/energy spectrum of the detector pair *Verena*/*Burkhard*.

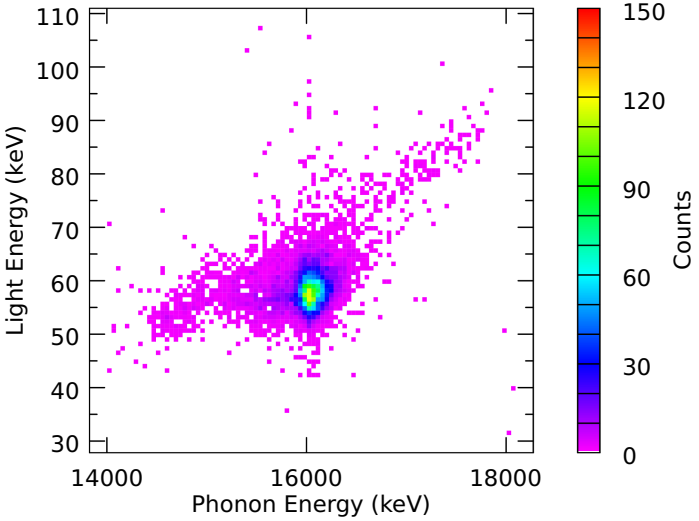

Figure B.2.: The region of α-cascades in the light/energy spectrum of *Verena*/*Q*.

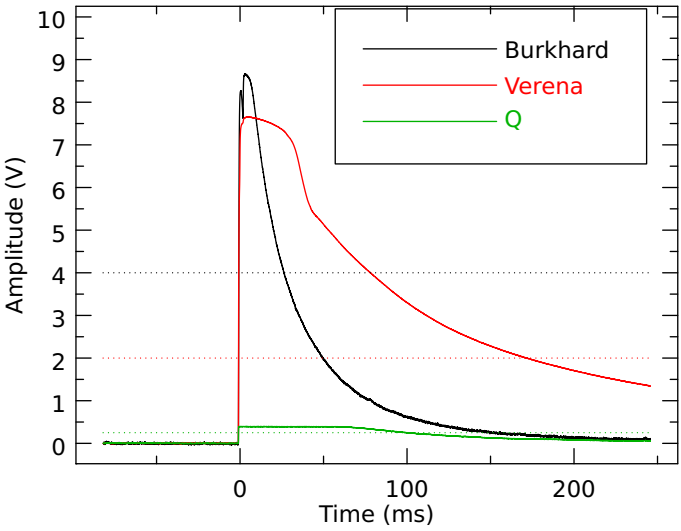

Figure B.3.: Fast α-cascade.

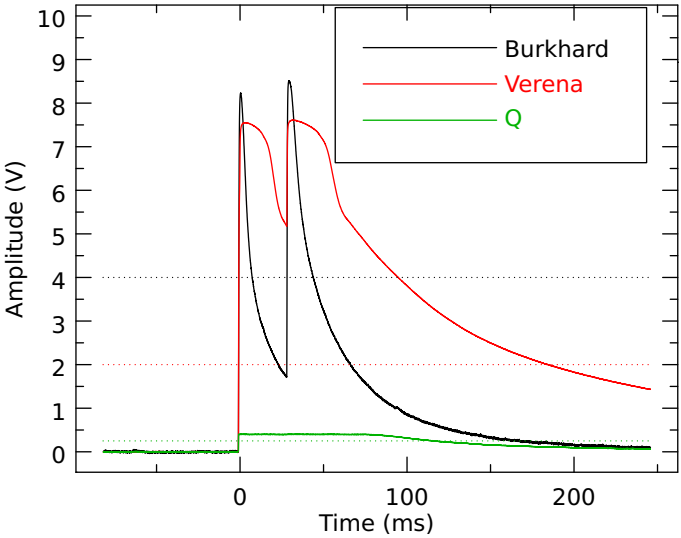

Figure B.4.: Slow α-cascade.

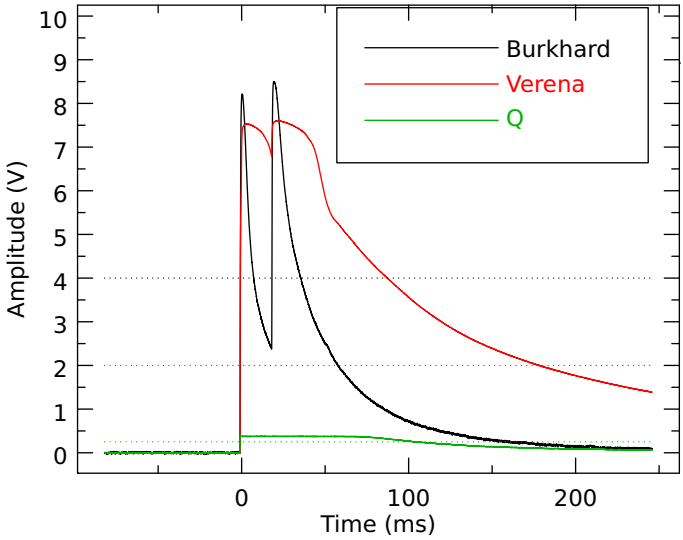

Figure B.5.: Between the peaks, the signal drops below the truncation level in *Burkhard*.

C. Visual method for analyzing the position dependent scintillation characteristics

According to equation (5.14), the variance of the difference of two correlated variables is

$$V_{\Delta,\text{correlated}} = V_{R,\text{Po}} + V_{P,\text{Po}} + V_{R,\text{Rn}} + V_{P,\text{Rn}} - 2C_{P,\text{PoRn}}. \tag{C.1}$$

The index "correlated" helps to distinguish between this case which concerns the subtraction of matching measurements and the subsequent case where the measurements were taken in random order.

As said in Section 5.1.1, the covariance bears information on how strongly two variables of data are correlated. Since the noise terms are not correlated to the other terms, all covariances concerning noises are zero.

If one assumes a position dependence, the covariance term has to be positive. Therefore, the difference of correlated measurements has a smaller variance than the sum of the variances:

$$V_{\Delta,\text{correlated}} < V_{\text{Po}} + V_{\text{Rn}}. \tag{C.2}$$

If there is no correlation between the measurements of ^{220}Rn and ^{216}Po, the covariance is zero. One way to artificially create a set of non-correlated data is to take a set of α-measurements which have been selected according to the method described in 5.1.3 and to randomly shuffle the data of one of the two sub-sets, e.g. the Po-decay. With a perfect non-correlation, the covariance becomes zero and the variance of the difference of the shuffled subsets is then

$$V_{\Delta,\text{shuffled}} = V_{R,\text{Po}} + V_{P,\text{Po}} + V_{R,\text{Rn}} + V_{P,\text{Rn}}, \tag{C.3}$$

which is the same as the sum of the variances. In practice, the variance of the shuffled difference might not reproduce the sum of the individual variances, since the shuffling is not necessarily perfect in building pairs of events from completely different crystal regions.

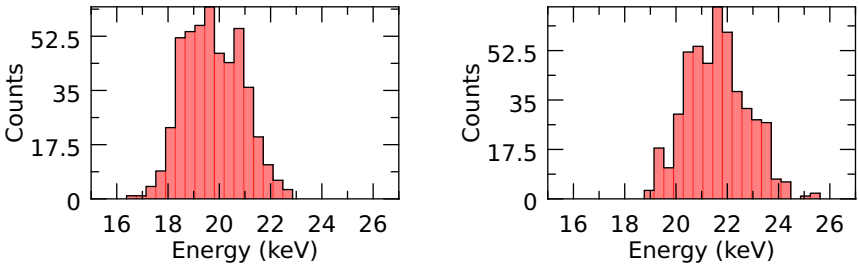

(a) ^{220}Rn-peak (b) ^{216}Po-peak

Figure C.1.: The light signals of ^{216}Po and ^{220}Rn with the detector *Burkhard*, calibrated in terms of absolute energy.

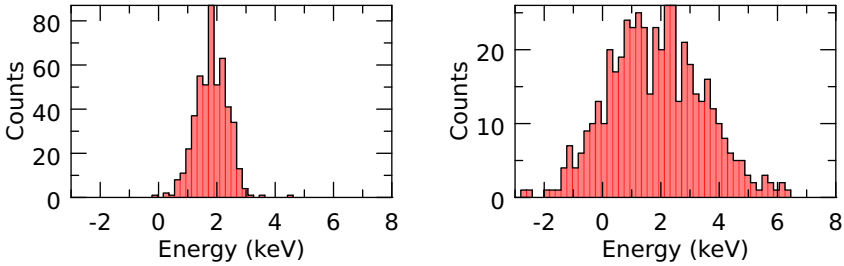

(a) Ordered (b) Shuffled

Figure C.2.: When subtracting the corresponding data of Figure C.1 from each other, the variance of the result depends on whether the data are ordered or shuffled.

Using the case of *Burkhard*, the data of the Figures C.1 and C.2 show how the visualization works. The Figures C.1(b) and C.1(a) are measured energy spectra of ^{220}Rn-α-decays and of matching ^{216}Po-α-decays. In order to obtain the plots in Figure C.2, one has to subtract, in a pair-wise fashion, the energy reading of a ^{216}Po-decay from that of a ^{220}Rn-decay and build a histogram of the differences. For plot C.2(a), the event pairs came from the same location while in case of plot C.2(b) these data were randomly shuffled.

With this simple mean of visualizing the subtracted data either ordered or shuffled, one can see that the position dependence has a significant contribution to the variance of the readings of *Burkhard*.

However, in order to obtain more than an optical impression, one would have to build histograms of the data, assume a model distribution, in this case a Gaussian, and fit the model to the data in order to obtain values for the variances the difference of which finally yields the covariance. All these assumptions and fits are sources of possible errors which one does not have to put up with when calculating the covariance directly from the data.

Index

List of Figures

List of Tables

Bibliography

[Abb11] M. Abbas. *La méthode des éléments finis isoparamétriques*. Référence Code_ASTER R3.01.00. 2011. URL: http://www.code-aster.org/V2/doc/default/fr/man_r/r3/r3.01.00.pdf.

[Ang+11] G. Angloher et al. "Results from 730 kg days of the CRESST-II Dark Matter Search." In: *European Physical Journal C* (2011). to be published. arXiv:1109.0702.

[Apr+11] E. Aprile et al. "Dark Matter Results from 100 Live Days of XENON100 Data." In: *Phys. Rev. Lett.* 107 (2011), p. 131302. DOI: 10.1103/PhysRevLett.107.131302. arXiv:1104.2549v3.

[Arn+10] C. Arnaboldi et al. "CdWO4 scintillating bolometer for Double Beta Decay: Light and heat anticorrelation, light yield and quenching factors." In: *Astroparticle Physics* 34.3 (2010), pp. 143 –150. ISSN: 0927-6505. DOI: 10.1016/j.astropartphys.2010.06.009. arXiv:1005.1239.

[Arp92] C. Arpesella. "Background measurements at Gran Sasso Laboratory." In: *Nucl. Phys. B, Proc. Suppl.* 28.1 (1992), pp. 420 –424. ISSN: 0920-5632. DOI: 10.1016/0920-5632(92)90207-9.

[Bav09] I. Bavykina. "Investigation of ZnWO4 and CaMoO4 as target materials for the CRESST-II Dark Matter search." PhD thesis. LMU München, 2009.

[Ber+10] Gianfranco Bertone et al. *Particle Dark Matter*. Ed. by Gianfranco Bertone. Cambridge University Press, 2010.

[BG06] L. Bergström and A. Goobar. *Cosmology and particle astrophysics*. 2nd ed. Springer, 2006.

[Bir64] J. B. Birks. *The Theory and Practice of Scintillation Counting*. Ed. by D. W. Fry and W. Higinbotham. Pergamon Press, 1964.

[Bot+97] A. Bottino et al. "Exploring the supersymmetric parameter space by direct search for WIMPs." In: *Physics Letters B* 402.1-2 (1997), pp. 113 –121. ISSN: 0370-2693. DOI: 10.1016/S0370-2693(97)00390-0.

[Cea+06] H. Cease et al. *Measurement of mechanical properties of three epoxy radhesives at cryogenic temperatures for CCD construction*. Fermi Nat'l Accelerator Laboratory. Nov. 2006. URL: http://lartpc-docdb.fnal.gov/0002/000249/001/fermilab-tm-2366-a.pdf.

[CEF99] S.Y.F. Chu, L.P. Ekström, and R.B. Firestone. *WWW Table of Radioactive Isotopes*. Feb. 1999. URL: http://nucleardata.nuclear.lu.se/nucleardata/toi/.

[Clo+06] D. Clowe et al. "A Direct Empirical Proof of the Existence of Dark Matter." In: *The Astrophysical Journal Letters* 648.2 (2006), p. L109. arXiv:astro-ph/0608407. URL: http://stacks.iop.org/1538-4357/648/i=2/a=L109.

[Coz+04] C. Cozzini et al. "Detection of the natural α-decay of tungsten." In: *Phys. Rev. C* 70.6 (Dec. 2004), p. 064606. DOI: 10.1103/PhysRevC.70.064606. arXiv:nucl-ex/0408006.

[CS99] E. Corbelli and P. Salucci. *The Extended Rotation Curve and the Dark Matter Halo of M33*. 1999. arXiv:astro-ph/9909252.

[DFS98] F. Donato, N. Fornengo, and S. Scopel. "Effects of galactic dark halo rotation on WIMP direct detection." In: *Astroparticle Physics* 9.3 (1998), pp. 247 –260. ISSN: 0927-6505. DOI: 10.1016/S0927-6505(98)00025-5.

[Eng91] J. Engel. "Nuclear form factors for the scattering of weakly interacting massive particles." In: *Physics Letters B* 264.1-2 (1991), pp. 114 –119. ISSN: 0370-2693. DOI: 10.1016/0370-2693(91)90712-Y.

[FPL11] A. Fraser-McKelvie, K. A. Pimbblet, and J. S. Lazendic. "An estimate of the electron density in filaments of galaxies at $z \sim 0.1$." In: *Monthly Notices of the Royal Astronomical Society* 415 (Aug. 2011), pp. 1961–1966. DOI: 10.1111/j.1365-2966.2011.18847.x. arXiv:1104.0711.

[GHJ73] M. Gluyas, F. D. Hughes, and B. W. James. "The elastic constants of calcium tungstate, 4.2 – 300 K." In: *Journal of Physics D: Applied Physics* 6.17 (1973), pp. 2025–2037. DOI: 10.1088/0022-3727/6/17/309.

[GM70] M. C. Gupta and R. D. MacFarlane. "The natural alpha radioactivity of samarium." In: *Journal of Inorganic and Nuclear Chemistry* 32.11 (1970), pp. 3425 –3432. ISSN: 0022-1902. DOI: 10.1016/0022-1902(70)80149-X.

[Hel56] R. H. Helm. "Inelastic and Elastic Scattering of 187-MeV Electrons from Selected Even-Even Nuclei." In: *Phys. Rev.* 104.5 (Dec. 1956), pp. 1466–1475. DOI: 10.1103/PhysRev.104.1466.

[Huf10] P. Huff. "The Detector Parameters Determining the Sensitivity of the CRESST-II Experiment." PhD thesis. TU München, 2010.

[Kie07] M. Kiefer. "Optimierung szintillierender Tieftemperaturkalorimeter für den direkten Nachweis von Teilchen der Dunklen Materie." Diploma thesis. Universität Würzburg, July 2007.

[KMW05] H. Kraus, V. B. Mikhailik, and D. Wahl. "Multiple photon counting coincidence (MPCC) technique for scintillator characterisation and its application to studies of $CaWO_4$ and $ZnWO_4$ scintillators." In: *Nuclear Instruments and Methods in Physics Research Section A: Accelerators, Spectrometers, Detectors and Associated Equipment* 553.3 (2005), pp. 522 –534. ISSN: 0168-9002. DOI: 10.1016/j.nima.2005.07.011.

[Kom+11] E. Komatsu et al. "Seven-Year Wilkinson Microwave Anisotropy Probe (WMAP) Observations: Cosmological Interpretation." In: *Astrophys.J.Suppl.* 192 (2011). DOI: 10.1088/0067-0049/192/2/18.

[Lan08] R. Lang. "Search for Dark Matter with the CRESST experiment." PhD thesis. TU München, 2008.

[Mar80] R. S. Markiewicz. "Kinetics of electron-hole droplet clouds: The role of thermalization phonons." In: *Phys. Rev. B* 21.10 (May 1980), pp. 4674–4691. DOI: 10.1103/PhysRevB.21.4674.

[Mos03] M. Moszynski. "Inorganic scintillation detectors in γ-ray spectrometry." In: *Nuclear Instruments and Methods in Physics Research Section A* 505.1-2 (2003). Proceedings of the tenth Symposium on Radiation Measurements and Applications, pp. 101 –110. ISSN: 0168-9002. DOI: 10.1016/S0168-9002(03)01030-1.

[Nar93] J. V. Narlikar. *Introduction to Cosmology*. 2nd ed. Cambridge University Press, 1993.

[NG10] K Nakamura and Particle Data Group. "Review of Particle Physics." In: *Journal of Physics G: Nuclear and Particle Physics* 37.7A (2010), p. 075021. DOI: 10.1088/0954-3899/37/7A/075021.

[Nin05] J. Ninkovic. "Investigation of $CaWO_4$ Crystals for Simultaneous Phonon-Light Detection in the CRESST Dark Matter Search." PhD thesis. TU München, 2005.

[OTF80] T. Oi, K. Takagi, and T. Fukazawa. "Scintillation study of ZnWO4 single crystals." In: *Applied Physics Letters* 36.4 (1980), pp. 278–279. DOI: 10.1063/1.91452.

[Pet06] F. Petricca. *Private communication*. Entry in the CRESST database. 2006.

[Pet11] F. Petricca. *Private communication*. 2011.

[Pre+92] W. H. Press et al. *Numerical Recipes in FORTRAN*. Cambridge University Press, 1992.

[Prö+95] F. Pröbst et al. "Model for cryogenic particle detectors with superconducting phase transition thermometers." In: *Journal of Low Temperature Physics* 100 (1 1995), pp. 69–104. DOI: 10.1007/BF00753837.

[PW07] T. Paszkiewicz and S. Wolski. "Young's and shear moduli and Poisson's ratio for elastic media of high and middle symmetry." In: *physica status solidi (b)* 244.3 (2007), pp. 978–987. DOI: 10.1002/pssb.200572716. arXiv:cond-mat/0607152.

[RHB08] J. Rösler, H. Harders, and M. Bäker. *Mechanisches Verhalten der Werkstoffe*. 3rd ed. Vieweg + Teubner, 2008.

[Sal] *Salome Platform Documentation*. Version 5.1.5. 2011. URL: http://www.salome-platform.org/user-section/online-documentation.

[Sch07] V. Schmidt. *Statistik I*. 2007. URL: http://www.mathematik.uni-ulm.de/stochastik/lehre/ss07/statistik1/skript.pdf.

[Sch10] J. Schmaler. "CRESST - New Analysis Methods and Results." PhD thesis. TU München, 2010.

[Seg97] E. Segre. *Die großen Physiker und ihre Entdeckungen*. München: Piper, 1997.

[Smi+07] M. C. Smith et al. "The RAVE Survey: Constraining the Local Galactic Escape Speed." In: *Mon.Not.Roy.Astron.Soc.* 379 (2007), pp. 755–772. DOI: 10.1111/j.1365-2966.2007.11964.x. arXiv:astro-ph/0611671 [astro-ph].

[Son10] A. Sonzogni. *Nudat 2 Database*. National Nuclear Data Center, Aug. 2010. URL: http://www.nndc.bnl.gov/nudat2/.

[Tau+97] T.D. Taulbee et al. "The measured electron response nonproportionalities of CaF2 , BGO, and LSO." In: *Nuclear Science, IEEE Transactions on* 44.3 (June 1997), pp. 489 –493. ISSN: 0018-9499. DOI: 10.1109/23.603696.

[Wit10] F. K. Wittel. *FEM for 4 - Eine kurze Einführung in die Finite Elemente Methode*. 2010. URL: http://www.ifb.ethz.ch/comphys/people/wittelf/FEM-Intro.

[YB71] B. Yates and A. C. Bailey. "The low-temperature anisotropic thermal expansion of calcium tungstate." In: *J. Low Temp. Phys.* 4.1 (Jan. 1971), p. 117125. DOI: 10.1007/BF00628442.

[ZBS04] W. Zucchini, F. Böker, and A. Stadie. *Statistik III*. 2004. URL: http://www.statoek.wiso.uni-goettingen.de/veranstaltungen/statistik3alt/daten/sec7.pdf.

[Zde+05] Yu.G. Zdesenko et al. "Scintillation properties and radioactive contamination of CaWO4 crystal scintillators." In: *Nuclear Instruments and Methods in Physics Research Section A: Accelerators, Spectrometers, Detectors and Associated Equipment* 538.1-3 (2005), pp. 657 –667. ISSN: 0168-9002. DOI: 10.1016/j.nima.2004.09.030.

[Zwi33] F. Zwicky. "Die Rotverschiebung von extragalaktischen Nebeln." In: *Helvetica Physica Acta* 6 (1933), pp. 110–127.

[NAS07] NASA/WMAP Science Team. *WMAP Media Resources*. June 2007. URL: http://map.gsfc.nasa.gov/m_or.html.

[Rad11] Radiochemical Society. *Gamma-ray spectrum catalog of isotopes*. 2011. URL: http://www.radiochemistry.org/periodictable/gamma_spectra/.

Acknowledgements

At the end, I would like to express my gratitude to the people who supported me during my time as a PhD student.

Many thanks to Dr. Franz Pröbst, in whose group I participated. He was always helpful when there were issues with the experiments or when I needed additional functionality in the software. Only with his counsel based on his comprehensive knowledge, it was possible to write this thesis.

Thanks to Prof. Dr. Allen Caldwell for supervising my work and for the interesting input. Thanks to Prof. Dr. Lothar Oberauer for being my second referee, especially on such a short notice.

The discussions with Federica were very important for this work. She was the one who taught me how to operate the cryostats at the beginning. During the analysis, she could always spare the time to help me sort my thoughts about the problems I was pondering on.

The same goes to my office mate Jens: Your feed back helped me more than once in times of confusion. Thank you for the many discussions, some serious and some not-so-serious.

Thanks to Dieter Hauff for teaching me how to operate most of the experimental hardware which I needed for measurements and thanks for helping me to produce the sensor films.

Thanks tho Karoline Schäffner for the many conversations, not only about physics but also on many other topics of life. The same goes to Rafael and Christof for the interesting debates on principles, at MPI and during my stays at Gran Sasso. Thanks also to Wolfgang, whose view of the world I first mistook as cynical before having to realize that most of the time he was just being realistic.

Kudos to my proof-readers Karo, Federica, Jens, Gena, and Patrick, and to Antonio for finding one of the last and most disturbing errors.

Gode Angloher was the person who had the initial idea that was the basis of my Diploma thesis – thank you for being such an example of enthusiasm.

Thanks to my current and former colleagues Anja, Clemens, Emilija, Florian, Irina, Katrin, and Patrick for contributing to this thesis in many ways.

I would like to thank Bernhard Kaster, Katarzyna Danielewicz, Uwe Leupold and Trung-Si Tran as representatives for the numerous people from the workshops and support groups of the Max-Planck-Institut für Physik

and the TU München that had their share in making this work possible. Thank you very much, especially to Holger Wetteskind for the fundamental information about FEM. Thanks as well to the people who gave me helpful advice in the SALOME and Code_ASTER Forums.

Zum Schluss vielen Dank an meine Eltern, meinen Bruder und auch an Tim, für die Unterstützung, die ich erfahren habe.